

Washington University in St. Louis

Washington University Open Scholarship

All Theses and Dissertations (ETDs)

January 2010

An Airloads Theory for Morphing Airfoils in Dynamic Stall with Experimental Correlation

Loren Ahaus

Washington University in St. Louis

Follow this and additional works at: <https://openscholarship.wustl.edu/etd>

Recommended Citation

Ahaus, Loren, "An Airloads Theory for Morphing Airfoils in Dynamic Stall with Experimental Correlation" (2010). *All Theses and Dissertations (ETDs)*. 11.

<https://openscholarship.wustl.edu/etd/11>

This Dissertation is brought to you for free and open access by Washington University Open Scholarship. It has been accepted for inclusion in All Theses and Dissertations (ETDs) by an authorized administrator of Washington University Open Scholarship. For more information, please contact digital@wumail.wustl.edu.

WASHINGTON UNIVERSITY IN ST. LOUIS

School of Engineering and Applied Science

Department of Mechanical, Aerospace, and Structural Engineering

Dissertation Examination Committee:

David Peters, Chair

Ramesh Agarwal

Mark Jakiela

Kenneth Jerina

Hiro Mukai

Swaminathan Karunamoorthy

AN AIRLOADS THEORY FOR MORPHING AIRFOILS IN
DYNAMIC STALL WITH EXPERIMENTAL CORRELATION

by

Loren A. Ahaus, M.S.

A dissertation presented to the School of Engineering
of Washington University in partial fulfillment of the
requirements for the degree of

DOCTOR OF PHILOSOPHY

May 2010

Saint Louis, Missouri

ABSTRACT OF THE DISSERTATION

An Airloads Theory for Morphing Airfoils in
Dynamic Stall with Experimental Correlation

by

Loren A. Ahaus

Doctor of Philosophy in Mechanical Engineering

Washington University in St. Louis, 2010

Research Advisor: Professor David A. Peters

Helicopter rotor blades frequently encounter dynamic stall during normal flight conditions, limiting the applicability of classical thin-airfoil theory at large angles of attack. Also, it is evident that because of the largely different conditions on the advancing and retreating sides of the rotor, future rotorcraft may incorporate dynamically morphing airfoils (trailing-edge flaps, dynamic camber, dynamic droop, etc.). Reduced-order aerodynamic models are needed for preliminary design and flight simulation. A unified model for predicting the airloads on a morphing airfoil in dynamic stall is presented, consisting of three components. First, a linear airloads theory allows for arbitrary airfoil deformations consistent with a morphing airfoil. Second, to capture the effects of the wake, the airloads theory is coupled to an induced flow model. Third, the overshoot and time delay associated with dynamic stall are modeled by a second-order dynamic filter, along the lines of the ONERA dynamic stall model. This paper presents a unified airloads model that allows arbitrary airfoil morphing with dynamic stall. Correlations with experimental data validate the theory.

Acknowledgments

This work was funded by the U.S. Army through the Georgia Tech Center of Excellence for Rotorcraft Technology, Michael Rutkowski technical monitor; and by NASA Ames Research Center, Grant NN A05CV28G, William Warmbrodt technical monitor. Many thanks to Tom Maier of the U.S. Army, to M.S. Chandrasekhara of NASA Ames for supplying data on the VR-12 airfoil, to Andrzej Krzysiak of the Institute of Aviation in Warsaw, Poland, and Janusz Narkiewicz of Warsaw University of Technology for supplying the data on the NACA 0012 trailing-edge flap airfoil, and to Rohit Jain of HyPerComp for supplying the data on the SC-1095 airfoil.

Loren A. Ahaus

Washington University in Saint Louis
May 2010

Contents

Abstract	ii
Acknowledgments	iii
List of Tables	vi
List of Figures	vii
Nomenclature	ix
1 Introduction	1
1.1 Motivation	1
1.2 Problem Statement and Approach	2
1.3 Literature Review	4
1.3.1 Early Work in Thin-Airfoil Theory	5
1.3.2 Finite-State Models	6
1.3.3 Dynamic Stall	7
1.3.4 Morphing Airfoils	8
1.3.5 Optimization	10
1.4 Overview	10
2 Development of the Unified Model	12
2.1 Johnson/Peters Flexible Airloads Theory	12
2.2 Two-dimensional Dynamic Inflow Model	17
2.3 Dynamic Stall Model	20
2.4 The Unified Model	23
2.4.1 Theory	23
2.4.2 Application	25
2.5 Static Correction Factors	26
3 Static Airfoil Section Characteristics	31
3.1 Theoretical Background	34
3.1.1 Linear Airloads	34
3.1.2 Static Stall Residuals	36
3.2 NACA 0012 Airfoil	37
3.2.1 Definitions	38
3.2.2 Pitching Moment	40

3.3	SC1095 Airfoil	41
3.4	Boeing VR-12 Airfoil	44
3.5	Conclusions on Static Data	45
4	Determination of Stall Parameters	65
4.1	Characteristics of Dynamic Stall Response	66
4.2	Mathematical Model	66
4.3	Stall Parameter Exercise for Variable-Droop VR-12	68
4.4	NACA 0012 Stall	71
4.5	SC-1095 Stall	72
4.6	Boeing VR-12 Stall	72
5	Dynamic Airload Correlations	80
5.1	Harmonic Pitch and Flap Simulations	80
5.2	Combined Pitch-Flap Oscillation	83
5.3	VR-12 Variable Droop	86
5.4	SC-1095 with LE Droop	90
6	Conclusions and Future Work	117
6.1	Conclusions	117
6.2	Required Constants	119
6.3	Future Work	121
Appendix A	Definition of Matrices and Vectors	124
Appendix B	Derivation of Spatial Gradient Components	127
Appendix C	Mean Line Expansion for LE and TE Droop	130
Appendix D	Chain Rule Application to Stall Residual Derivatives	134
References	137
Vita	142

List of Tables

3.1	Angle of zero lift for NACA $\overline{m\bar{p}}$ 12 airfoils.	62
3.2	Tabulated values for ΔC_L and ΔC_M for morphed NACA 0012 airfoil.	63
3.3	Tabulated values for ΔC_L and ΔC_M for SC-1095 airfoil.	64
5.1	Summary of airload correlations. (*Mean and Amp. are measured in degrees)	116
B.1	Spatial gradient components for NACA four-digit airfoils	129

List of Figures

1.1	Schematic of the unified airloads model.	11
2.1	General airfoil coordinate system	28
2.2	Physical significance of first three shape functions.	29
2.3	Comparison of exact and approximate Theodorsen function $C(k)$. . .	29
2.4	Illustration of static stall	29
2.5	Coordinate system for large angles.	30
2.6	Air loads on a typical airfoil section.	30
3.1	Schematic for the parameterization of static characteristics.	46
3.2	Comparison of steady and quasi-steady airloads for VR-12 airfoil. . .	47
3.3	Section lift curves for NACA $\overline{m\overline{p}}12$ airfoils.	48
3.4	Section moment curves for NACA $\overline{m\overline{p}}12$ airfoils.	49
3.5	Angle of zero lift for NACA $\overline{m\overline{p}}12$ airfoils.	50
3.6	Static stall angle for NACA $\overline{m\overline{p}}12$ airfoils.	50
3.7	Deflected geometry for LED and TED SC1095 airfoils.	50
3.8	Angle of zero lift for SC-1095 airfoil with LED and TED.	51
3.9	Section lift curves for SC-1095 airfoil with leading-edge deflection. . .	52
3.10	Section moment curves for SC-1095 airfoil with leading-edge deflection.	53
3.11	Section lift curves for SC-1095 airfoil with trailing-edge deflection. . .	54
3.12	Section moment curves for SC-1095 airfoil with trailing-edge deflection.	55
3.13	Section lift curves for SC-1095 airfoil with arbitrary morphing.	56
3.14	Section moment curves for SC-1095 airfoil with arbitrary morphing. . .	57
3.15	Static section characteristics for the Boeing VR-12 airfoil, $M = 0.3$. . .	58
3.16	Static lift residuals for the VR-12 baseline and VDLE airfoils at $M =$ 0.2, 0.3, 0.4.	59
3.17	Static moment residuals for the VR-12 baseline and VDLE airfoils at $M = 0.2, 0.3, 0.4$	60
3.18	Static stall angle vs. Mach number for VR-12 airfoil.	61
4.1	Oscillating airfoil in a free stream	74
4.2	Lift coefficient for VR-12 airfoil at $k \leq 0.1$	75
4.3	Experimental correlation with initial parameter estimates	75
4.4	Experimental correlation with final results from genetic algorithm . . .	76
4.5	Fitness value per generation of genetic algorithm	76
4.6	Comparison of NACA 0012 dynamic stall with Ref. [30]	77

4.7	Comparison of SC1095 dynamic stall with Ref. [54]	78
4.8	Comparison of VR-12 dynamic stall with Ref. [32]	79
5.1	Comparison with Theodorsen theory for harmonic pitch oscillations.	91
5.2	Comparison with Theodorsen theory for harmonic flap oscillations.	91
5.3	NACA 0012 airfoil with TE flap, no dynamic stall, $\phi = 59^\circ$.	92
5.4	NACA 0012 airfoil with TE flap, no dynamic stall, $\phi = 122^\circ$.	93
5.5	NACA 0012 airfoil with TE flap, no dynamic stall, $\phi = 239^\circ$.	94
5.6	NACA 0012 airfoil with TE flap, moderate stall, $\phi = 148^\circ$.	95
5.7	NACA 0012 airfoil with TE flap, moderate stall, $\phi = 206^\circ$.	96
5.8	NACA 0012 airfoil with TE flap, moderate stall, $\phi = 298^\circ$.	97
5.9	NACA 0012 airfoil with TE flap, heavy stall, $\phi = 177^\circ$.	98
5.10	NACA 0012 airfoil with TE flap, heavy stall, $\phi = 343^\circ$.	99
5.11	Experimental setup of VR-12 drooped leading-edge airfoil.	100
5.12	Dynamic airload correlation, VR-12 baseline airfoil, $k=0.05$, $M=0.2$	101
5.13	Dynamic airload correlation, VR-12 baseline airfoil, $k=0.05$, $M=0.3$	102
5.14	Dynamic airload correlation, VR-12 baseline airfoil, $k=0.05$, $M=0.4$	103
5.15	Dynamic airload correlation, VR-12 20° variable droop, $k=0.05$, $M=0.2$	104
5.16	Dynamic airload correlation, VR-12 20° variable droop, $k=0.05$, $M=0.3$	105
5.17	Dynamic airload correlation, VR-12 20° variable droop, $k=0.05$, $M=0.4$	106
5.18	Dynamic airload correlation, VR-12 baseline airfoil, $k=0.10$, $M=0.2$	107
5.19	Dynamic airload correlation, VR-12 baseline airfoil, $k=0.10$, $M=0.3$	108
5.20	Dynamic airload correlation, VR-12 baseline airfoil, $k=0.10$, $M=0.4$	109
5.21	Dynamic airload correlation, VR-12 20° variable droop, $k=0.10$, $M=0.2$	110
5.22	Dynamic airload correlation, VR-12 20° variable droop, $k=0.10$, $M=0.3$	111
5.23	Dynamic airload correlation, VR-12 20° variable droop, $k=0.10$, $M=0.4$	112
5.24	Figure 25 of Ref. [50], reprinted for comparison.	113
5.25	Change in airfoil L/D for various leading-edge deflections.	113
5.26	Lift coefficient for dynamic leading-edge deflection.	114
5.27	Quasi-steady drag coefficient for dynamic leading-edge deflection.	114
5.28	L/D ratio for dynamic leading-edge deflection.	115
6.1	Comparison of unified model with CFD for NACA 0012 with TE flap.	123
B.1	Coordinates of NACA 2512 airfoil	128
C.1	Geometry of drooped leading-edge airfoil	133
C.2	Geometry of drooped trailing-edge airfoil	133

Nomenclature

a	location of center of rotation aft of mid-chord, semi-chords
\hat{a}	ONERA lift-curve slope
$a_{\text{corr.}}$	static correction to center of rotation
b	blade semi-chord
b_n	induced flow expansion coefficients
$C(k)$	Theodorsen lift deficiency function
C_L	lift coefficient
ΔC_L	static lift residual (static stall)
C_M	moment coefficient about the center of rotation
ΔC_M	static pitching moment residual
C_n	generalized load coefficient
ΔC_n	static residual of the n th generalized load
d	location of TE flap or droop hinge aft of mid-chord, semi-chords
e	location of LE flap or droop hinge forward of mid-chord, semi-chords
\hat{e}	lead term on stall filter
f	reversed-flow parameter
f_L	static correction factor to lift coefficient
f_M	static correction factor to pitching moment coefficient
f_α	static correction factor to angle of attack input
f_β	static correction factor to TE flap input
f_δ	static correction factor to LE droop input
$h(x, t)$	generalized airfoil motion, positive down, m
h_n	components of generalized airfoil deformation, m
h'_n	components of spatial gradient of airfoil meanline
k	reduced frequency of oscillation, $\omega b/u_0$
L	lift per unit span, N/m
L_n	generalized loads per unit span, N/m
M	number of expansions in airloads theory

N	number of inflow states
ΔP	pressure drop across airfoil, N/m^2
r	radial position along blade, m
R	rotor radius, m
\hat{s}	ONERA apparent mass term
t	time, sec
T	characteristic non-dimensional time constant
T_n	Chebychev polynomials of the first kind
U	ONERA non-dimensional free-stream velocity
$u(z)$	unit step function
u_0	velocity component in the x direction, m/sec
\bar{u}_0	time-averaged u_0 , m/sec
u_T	time-averaged free stream, m/sec
v	total induced velocity, m/sec
v_0	uniform velocity component in the y direction, m/sec
v_1	velocity gradient, m/sec
\bar{v}	induced flow due to bound circulation, m/sec
\bar{v}_L	time-averaged vertical velocity, m/sec
w_n	components of total velocity field, m/sec
x	Cartesian coordinate, m
\bar{x}	NACA chord variable, $\bar{x} = (1 + x/b)/2$
y	Cartesian coordinate, m
z	shift variable $z = \alpha - \alpha_{ss}$, rad
z_0	value of z below which ΔC_n is negligible
α	airfoil angle of attack, rad
α_{0L}	angle of zero lift, rad
α_{shift}	shift in stall initiation angle, rad
α_{ss}	static stall angle, rad
β	TE flap deflection, rad
γ	circulation per unit length, m/s
γ_b	bound circulation, m/s
γ_n	components of velocity due to bound circulation, m/s
γ_w	wake circulation, m/s
Γ	total bound circulation, m^2/s

Γ_n	change in circulation due to dynamic stall of n th generalized load, m^2/s
$\bar{\Gamma}$	ONERA nondimensional circulation
δ	leading-edge droop angle, $rad.$
$\hat{\delta}$	ONERA rate term
$\hat{\eta}$	damping of stall filter
λ	part of v due to γ_w , m/s
λ_n	components of velocity due to shed wake, γ_w , m/s
$\hat{\lambda}$	ONERA pole location
ξ	dummy variable of integration
ρ	density of air, kg/m^3
τ	non-dimensional time u_0t/b
τ_n	expansion coefficients for $\Delta P/(2\rho)$, m^2/s^2
φ	Glauert variable, rad
φ_m	Glauert variable at the flap hinge location d , rad
ϕ	phase angle between pitch and flap input
ω	frequency, rad/sec
$\hat{\omega}$	frequency of stall filter
$(\dot{})$	$\partial()/\partial t$
(\ast)	$\partial()/\partial \tau$

Subscripts:

LE	leading-edge
LED	leading-edge droop
TE	trailing-edge
TED	trailing-edge droop
(b)	baseline
(m)	morphed

Chapter 1

Introduction

1.1 Motivation

The analysis of helicopter rotors remains one of the most challenging problems in aerodynamics. Much of this difficulty is related to the substantially different aerodynamic environments on the advancing and retreating sides of the rotor in forward flight. The advancing side of the rotor is characterized by large Mach numbers and relatively low angles of attack. By contrast, the retreating side of the rotor experiences lower Mach numbers and larger angles of attack, causing the airfoil to stall. This cyclic variation in pitch and time-varying freestream, cycling in and out of the stall regime of the airfoil, leads to the phenomenon of dynamic stall. No complete physical model of dynamic stall based on first principles has yet been developed. However, various empirical models have been employed to simulate dynamic stall behavior. One such model, first developed by ONERA [1] [2] and later extended by Peters and Rudy [3], is investigated in this thesis and integrated with a state-space airloads theory.

As though the presence of dynamic stall were not enough of a complication, many future helicopter designs may include morphing airfoils to improve efficiency, reduce noise and vibration, and alleviate dynamic stall. NASA is interested in addressing these problems to increase U.S. competitiveness in world aerospace markets. The U.S. Army and NASA are interested in morphing airfoils for next generation high efficiency rotorcraft, including heavy-lift concepts. With advances in smart materials and actuator technology, there are many possible morphologies beyond the simple trailing-edge flap. These may include dynamic droop, dynamic camber, leading-edge slats, gurney flaps, and many others. Thus, a useful aerodynamic analysis tool is

needed that would be able to transform morphing airfoil motions into lift, pitching moment, and drag for a two-dimensional airfoil section.

The goal of this work is to offer a unified airloads theory for morphing airfoils, which is integrated with a dynamic stall model. This theory is not intended to supplant wind-tunnel testing or CFD analysis, but rather is intended as a reduced-order model for preliminary design calculations and flight simulation. The model is constructed so as to take a limited data base of airfoil response (from either wind tunnel tests or CFD) and to use those data to construct a reduced-order model that can be taken beyond the individual test cases.

This work was funded by the U.S. Army through the Georgia Tech Center of Excellence for Rotorcraft Technology, Michael Rutkowski technical monitor; and by NASA Ames Research Center, Grant NN A05CV28G, William Warmbrodt technical monitor. This project supports other funded work at the Georgia Institute of Technology and the University of Michigan.

1.2 Problem Statement and Approach

The problem to be addressed in this thesis is how to integrate the finite-state airloads theory of Ref. [4] with a hierarchical model of dynamic stall. The following issues related to the integration of these models into a consistent, unified theory are addressed:

1. How are the airload and dynamic stall equations to be coupled?
2. How should static, unstalled corrections be made to the theory?
3. Should all generalized loads have the same stall dynamics, or should each load have a unique set of poles and zeros?
4. What is the minimum amount of static and dynamic stall data necessary to model the airfoil behavior adequately?
5. How can the theory be made hierarchical so that the level of modeling fidelity can be varied?

The unified model presented herein consists of three basic components that are coupled together in a consistent manner. A schematic of the model is given in Fig. 1.1. The idea related in the figure is that airfoil motions (angle of attack plus morphing dynamics) would be transformed into a generalized set of coordinates (h_n and h'_n). The use of generalized coordinates makes the theory independent of the specific morphing geometry used. These generalized coordinates, when combined both with the flowfield geometry (u_0, v_0, v_1) and with the induced flow distribution at the airfoil from the shed wake (λ_n) provide the boundary conditions that can be fed into the first component to be synthesized—a **linear airloads theory**. This theory should compute the desired bound circulation to match the nonpenetration boundary condition. That process then provides the generalized loads (L_n) corresponding to the virtual work of the generalized displacements h_n . Those linear loads, along with any modifications due to stall, are then fed into the second component of the present approach—an **induced flow model**. In principle, this model could come from any physical description of the wake, depending upon the geometry of the flow (e.g., wind tunnel tests, fixed wing, rotating wing, etc.). The induced-flow model would give the induced flow due to the shed wake (λ_n). The third component of the present approach is the **dynamic stall model**. The concept proposed here is that the airfoil boundary conditions in terms of generalized coordinates would be utilized in some representation of nonlinear static stall data in order to determine what the static stall correction to the airloads might be (ΔC_n). This set of static corrections then drives a dynamic filter (the dynamic stall model proper) that produces the dynamic modifications to the airloads (Γ_n). The idea is that the dynamic filter can provide the time delay and overshoot known to be typical of dynamic stall. Finally, the linear loads (L_n) and the stall corrections (Γ_n) are combined for the total airloads ($L_{n \text{ (total)}}$) that will drive both any structural dynamics and any induced flow model. This is the general approach we wish to formulate, as developed to follow.

Our choice for the Airloads component of this model is the Johnson/Peters thin-airfoil theory that allows for airfoil deformations consistent with a morphing airfoil [4]. These airfoil deformations may arise from a trailing-edge flap, nose droop, dynamic camber, or any of a variety of other possible deformation morphologies. The Johnson/Peters theory is general enough to capture any of these, and it is written in terms of generalized coordinates associated with Chebychev polynomials. The theory takes as an input arbitrary induced flow from any induced-flow model and provides a

time history of both blade loads and total bound circulation as an output. It may be coupled to any induced-flow model—two-dimensional or three-dimensional. Thus, it is ideal. In this work, since we are correlating two-dimensional test data, we will be using the 2-D finite-state theory of Karunamoorthy [5] for the induced-flow model. However, the present approach is easily applied in conjunction with any other induced-flow theory. Third, we develop a dynamic stall model that utilizes a dynamic filter after the manner of the ONERA model in order to generate the corrections to airloads and bound circulation that are due to dynamic stall. In particular, we generalize the ONERA approach to be applicable to arbitrary generalized loads, and we synthesize static data in terms of the generalized coordinates.

The validation of the overall model is accomplished by first validating the individual components of the theory. These include comparing the model to Theodorsen theory for harmonic motions, correlating NACA 0012 dynamic stall data, and developing a database of static airfoil data parameterized by generalized airfoil coordinates. Then the unified model is used to correlate wind-tunnel test data on three different morphing airfoils:

1. NACA 0012 airfoil with trailing-edge flaps
2. Boeing VR-12 airfoil with variable droop leading edge
3. Sikorsky SC-1095 airfoil with leading-edge warping

Correlations are done at various Mach numbers, reduced frequencies, and morphing combinations.

1.3 Literature Review

A review of previous work from the literature has been separated into the following sections:

1. Early work in thin-airfoil theory
2. Finite-state models

3. Dynamic stall
4. Morphing airfoils
5. Optimization

1.3.1 Early Work in Thin-Airfoil Theory

Thin-airfoil theory was developed in the early 1920's, a time of rapid expansion in understanding aerodynamics. Max Munk developed a general theory for thin wing sections [6]. The theory was intended as a simple tool to calculate the aerodynamic loads on thin airfoil sections. It assumes inviscid, incompressible fluid flow, with the airfoil being replaced by a line of vorticity distributed along the mean camber line. Munk derives general integral relationships for the zero lift angle, static pitching moment, and center of pressure, and shows that these are properties of only the mean camber line geometry for sufficiently thin airfoils. Solutions are presented for several common configurations. Munk also investigates the effectiveness of tail plane elevators in the context of the theory.

Thin-airfoil theory was further refined by Theodorsen and Garrick [7] [8], in which conformal mapping is used to map a circle into various airfoil shapes for potential flow analysis. Theodorsen also authored various NACA reports concerned with the mechanism of flutter on wing-aileron configurations [9]. It was observed that—at a certain free-stream velocity, called the flutter speed—aerodynamic forces could lead to exponentially increasing flap oscillations. Theodorsen considered the borderline case of neutrally stable (simple harmonic) motion. The analysis is based on potential flow and application of the Kutta condition (i.e., zero pressure drop across the trailing edge). The result is a frequency-response function for airfoils undergoing simple harmonic motion. Thus, Theodorsen's work is not restricted to fixed wing-aileron configurations, but also lays the foundation for analyzing rotary wings.

Extensions of Theodorsen's work were made during the next two decades. Theodore von Kármán analyzed the leading edge suction peaks on a thin airfoil [10]. Garrick used von Kármán's equations to analyze the drag or propulsive force generated by flapping or oscillating airfoils [11]. He showed that it is possible to derive a

propulsive force from a flapping wing. In the 1940's, Issacs extended Theodorsen theory to the case of an airfoil undergoing simple-harmonic oscillations in a free-stream that is also undergoing simple-harmonic variation [12] [13]. This was an important extension for rotorcraft, due to the periodic free-stream velocity of a helicopter in forward flight. Greenberg simplified the result of Issacs by neglecting the periodic vortex spacing [14]. Reference [15] shows that the Greenberg approximation can lead to significant error in lift coefficient. Nonetheless, the actual lift predicted by the theory is in fairly good agreement with Issacs. This is because the greatest errors in lift coefficient occur when the free-stream velocity is relatively small. Many simulation codes use the Greenberg approximation. Loewy generalized Theodorsen theory to a helicopter in hover or climb by assuming a layered wake approximation [16].

While much work was being done in the frequency domain, others attempted to analyze unsteady aerodynamics in the time domain. Wagner derived an indicial function for the unsteady aerodynamics on a thin airfoil [17]. W. P. Jones showed that the Wagner function (in the time domain) is related to the Theodorsen function (in the frequency domain) through a Fourier Transform pair [18]. R. T. Jones derived a two-state approximation to both the Wagner and Theodorsen functions [19] [20]. Later work by Edwards, *et. al.* [21] [22], developed an exact expression for the Theodorsen function in the Laplace domain in terms of Bessel functions.

1.3.2 Finite-State Models

Up until the 1970's, most time-domain aerodynamic analysis focused on indicial methods, in which arbitrary motion is analyzed by application of the convolution integral. These methods provide a link between the step response and time-domain response. However, they can be cumbersome. Various other methods of transforming frequency domain aerodynamics into the time domain were developed during the 1980's and 1990's. Work by Vepa [23] and Dowell [24] [25] introduced a simple method for developing a finite-state model in the time domain by use of Padé approximants. This method gives a best approximation for a transfer function by a rational function of a given order. Friedmann used this method to convert Loewy theory into state-space [26] [27]. Dowell also showed how singular-value decomposition could be used to transform CFD grids into reduced-order finite-state models [24].

Recent work by Ref. [28] uses a reduced-order model to analyze pitching/plunging airfoils. The model uses Kriging interpolation to map CFD results into a reduced-order surrogate model to capture non-linearities of the flow. However, both the surrogate models and the CFD data from which they were generated are for a two-dimensional flow. Thus they inherently include Theodorsen/Wagner two-dimensional induced flow. These induced flow assumptions cannot be separated from the model, so the surrogate models cannot be applied directly to three-dimensional flows.

Peters, *et al.*, developed an alternative finite-state aerodynamic model, via expansions in a Glauert series [5] [15] [29]. This model is used in the current work to compute the linear airloads. The model is based on two-dimensional potential flow, with the non-penetration boundary condition applied on the airfoil and the Kutta condition applied at the trailing edge. The Peters state-space airloads model has several advantages over previous state-space models. First, the theory is couched in terms of Chebychev polynomials, which are a natural coordinate system for airfoil motions. The first three polynomials correspond physically to plunge, pitch, and camber about the mid-chord. The model is hierarchical, and only a limited number of terms are required to capture the essential physics. For instance, a symmetric airfoil undergoing simple pitch motions can be modeled exactly using only the first two terms. A more complicated airfoil geometry necessitates using additional terms. The theory can be coupled with any induced-flow model, two- or three-dimensional, allowing it to be easily incorporated into rotorcraft aerodynamic analysis tools. The model is general, allowing large-frame motions, unsteady free stream, and arbitrarily morphing airfoil shape. It is computationally efficient due to the limited number of terms required, making it well suited for preliminary design work or flight simulation. Reference [29] shows that the Karunamoorthy approach (with unsteady free-stream) gives a virtually exact correlation with Issacs' Theory.

1.3.3 Dynamic Stall

Dynamic stall is a complicated aerodynamic phenomenon in which a vortex-like disturbance is shed by an airfoil at large angle of attack. The disturbance often originates near the leading edge and translates along the airfoil, resulting in a highly non-linear pressure disturbance. This nonlinearity causes the airloads to diverge significantly

from those predicted by linear, thin-airfoil theory. There have been many semi-empirical models designed to quantify the effect of dynamic stall on airloads [30]. Most of these models share certain characteristics. Namely, the difference between static and dynamic stall increases as the pitch rate increases, and the stall takes a finite time to develop. The models are typically applied as empirical corrections to steady data, and are based on wind tunnel testing. They apply over a fairly restrictive range of airfoil types, angle of attack, Mach number, etc.—based on the test conditions from which they were derived.

ONERA developed a third-order model of dynamic stall [1] [2]. A first-order equation is used to simulate the Theodorsen function (for low angles of attack). This, coupled with apparent mass terms gives a reasonable approximation for rigid, unstalled airfoils. Then, the static changes in stall (as observed in static test data) are sent through a second-order dynamic filter (one zero and two poles) to simulate the delay of stall onset and the stall overshoot observed in test data. The locations of the complex-conjugate poles (and real zero) are made functions of angle of attack. This is effected by the conduct of small-oscillation experiments about various static angles and identification of the coefficients as functions of angle of attack (or, equivalently) as functions of the lift deficiency due to stall.

Reference [31] presents the results of a fairly extensive wind-tunnel test program at the NASA Ames research facility to validate the ONERA model. While the model is unable to reproduce some of the severe overshoot associated with certain dynamic stall scenarios, it does capture the character of the stall. Its ease of incorporation into the state-space airloads theory makes it an attractive model for handling dynamic stall in preliminary design and real-time flight simulation.

1.3.4 Morphing Airfoils

Most helicopters have historically used a swashplate mechanism for 1/rev cyclic control of rotor blades. Due to the need for improved rotor performance for heavy-lift applications, as well as noise and vibration reduction, there has been increasing interest in dynamically morphing airfoils. The idea of Individual Blade Control (IBC)

for higher harmonic control of individual blades is becoming more feasible with improvements in smart structure technology, materials, and adaptive control. Morphing airfoils may take various forms: trailing-edge flaps, dynamically varying droop, camber, or twist, to name a few. References [32] and [33] describe the use of variable leading-edge droop to mitigate the effects of dynamic stall including test data. These data provide one of the test cases for validating the current airfoil theory.

Reduction in vibration associated with dynamic stall flutter has also been demonstrated using actively controlled trailing-edge flaps [34]. The U.S. Army published a comparison of various active control concepts on the VR-12 airfoil [35]. The concepts studied were: leading edge slat, variable droop leading edge, oscillatory jet, Gurney flap, individual blade control, active twist, and trailing-edge flap. The computational results were based on the CAMRAD II comprehensive code. Of the concepts studied, individual blade control, trailing-edge flap, and active twist showed the most promise of improved performance. The authors note that the results depend strongly on the static airfoil tables used. This underscores the importance of accurate static airfoil section characteristics for application of the theory. This is one of the major goals of the current research.

Various approaches for the solution of aerodynamic loads on morphing airfoils have been presented. Hariharan and Leishman use an indicial approach to develop a state-space model of unsteady airloads for a flapped airfoil [36]. They present experimental correlations for small-amplitude, harmonic flap deflections using the indicial approach, with corrections for Mach number and flap effectiveness. These same data were later used in Ref. [29] to compare the Peters state-space airloads theory to the indicial approach. Good correlation was found between the Peters approach and the data for lift, pitching moment, and moment about the trailing-edge flap hinge. In general, the Peters model performed better than did the indicial approach. Wickheiser and Garcia present a solution approach that employs lifting-line analysis to determine the airloads for wings of morphing cross-section and planform [37].

1.3.5 Optimization

Engineering analysis typically approximates physical behavior with a mathematical model. The parameters for the model are selected to minimize the error between theoretical and experimental data. Thus, identification of these parameters is often couched as an optimization problem. Optimization methods are generally divided into two types: deterministic and heuristic. Deterministic approaches, such as Newton’s and steepest descent methods, start from a single point and use gradient calculations with respect to the design variables to locate local optima. Heuristic approaches, such as genetic algorithms and simulated annealing, search the entire design population and use probabilistic transition rules to move toward an optimum. These methods are often faster, because they do not require gradient and hessian computations. They are also better suited to multi-modal design spaces.

In Ref. [38], Pulliam *et al* compare the heuristic genetic algorithm method to the deterministic adjoint-gradient method for optimization of a transonic airfoil design. The fitness function is a weighted combination of multiple objectives: to minimize drag and maximize lift. The authors found that both optimization techniques found similar optimal airfoil shapes, with nearly identical Pareto fronts. In Ref. [39], a non-linear indicial approach is used to determine the unsteady lift and pitching moment for an aircraft at high angles of attack. The fitness is determined by the least-squares error between wind-tunnel test data and the mathematical model. The resulting parameter fit is validated by correlation of experimental data at various reduced frequencies. Thus, genetic algorithms have been shown effective in optimization problems for unsteady aerodynamics.

1.4 Overview

We have established that there is a need for an airloads model that can treat both unstalled and stalled conditions for morphing airfoils. The model should be capable of handling unsteady freestream, large frame motions, and generalized wakes—and should be able to do so efficiently. We have also outlined the building blocks in the

literature that will be synthesized into such a model. In the sections to follow, such a model will be developed and validated.

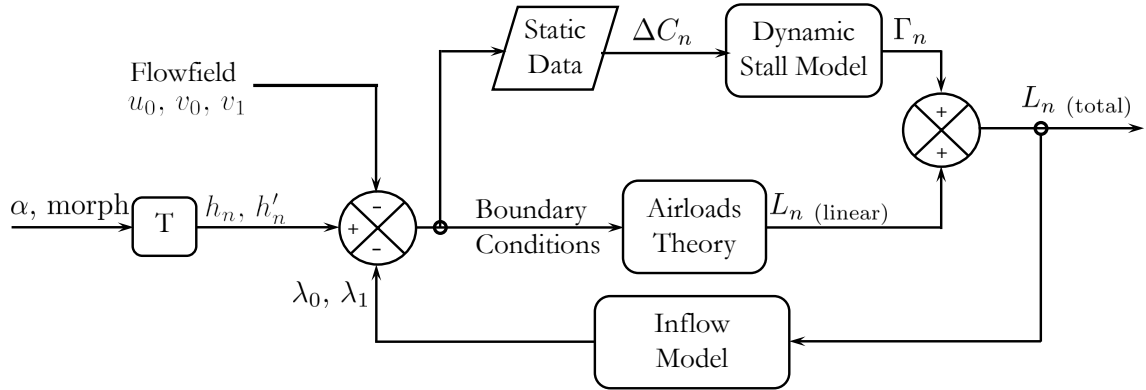


Figure 1.1: Schematic of the unified airloads model.

Chapter 2

Development of the Unified Model

A unified airloads model must allow for arbitrary airfoil motion, unsteady free stream, morphing airfoil shape, and dynamic stall. There are three key elements of the unified model: the Peters flexible airloads theory, the 2D dynamic inflow model, and the modified ONERA dynamic stall model. This chapter summarizes the derivation and development of each of these components of the theory.

2.1 Johnson/Peters Flexible Airloads Theory

The derivation of the Johnson/Peters flexible airloads theory from first principles is presented here, following the procedure of Ref. [15]. Consider a thin airfoil of arbitrary shape moving through a mass of still air, as shown in Fig. 2.1. The coordinate system is centered at the mid-chord, so that $-b \leq x \leq +b$, where b is the semi-chord. The coordinate system is moving with some arbitrary motion, described by horizontal velocity u_0 , vertical velocity v_0 , and rotation v_1 . The deformations of the airfoil within the reference frame are considered small, such that $h \ll b$, $\partial h / \partial x \ll 1$, and $\partial h / \partial t \ll u_0$. Furthermore, circulation is assumed to be shed along the x -axis. These small-angle assumptions are less restrictive than many airfoil theories. While the airfoil motions within the frame are assumed to be small, the reference frame itself is allowed to have arbitrarily large motion. This makes the theory particularly suited to analysis of rotary wings.

As is the case for classical thin-airfoil theory, the system is constrained by the non-penetration boundary condition at the airfoil surface. The non-penetration

boundary condition can be expressed as:

$$w = \bar{v} + \lambda = u_0 \frac{\partial h}{\partial x} + \frac{\partial h}{\partial t} + v_0 + v_1 \frac{x}{b} \quad (2.1)$$

where w is the total induced flow, λ is the induced flow from shed circulation, and \bar{v} is the induced flow from bound circulation. The first two terms on the right-hand side of Eq. 2.1 are the result of the shape of the airfoil mean-line, and the second two terms are from frame motion. It is apparent that the theory captures both static and dynamic shape changes, making the theory applicable to dynamically morphing airfoils. From the Biot-Savart law, \bar{v} may be expressed in terms of the bound circulation per unit length γ_b over the interval $-b \leq x \leq +b$, corresponding to the airfoil surface:

$$\bar{v} = -\frac{1}{2\pi} \int_{-b}^{+b} \frac{\gamma_b(\xi, t)}{x - \xi} d\xi \quad (2.2)$$

Similarly, the induced flow from shed circulation may be expressed in terms of the wake circulation:

$$\lambda = -\frac{1}{2\pi} \int_{+b}^{\infty} \frac{\gamma_w(\xi, t)}{x - \xi} d\xi \quad (2.3)$$

The pressure-vorticity relation gives the loading due to the circulation as:

$$\Delta P = \rho u_0 \gamma_b + \rho \int_{-b}^x \frac{\partial \gamma_b}{\partial t} d\xi \quad (-b \leq x \leq +b) \quad (2.4)$$

The spatial gradient of the induced flow due to the shed wake is related to the temporal gradient of the induced flow by the relation:

$$\frac{\partial \lambda}{\partial t} + u_0 \frac{\partial \lambda}{\partial x} = \frac{1}{2\pi} \frac{d\Gamma/dt}{b - x} \quad (2.5)$$

where Γ is the total bound circulation on the airfoil. Equations (2.1-2.5) define the airloads theory, which must be expressed in terms of the generalized loads, frame motions, and blade deformations. To do this, all of the variables are expressed as expansions with respect to the Glauert variable, φ . The change of variable is given by:

$$x = b \cos \varphi \quad (-b \leq x \leq +b, \quad 0 \leq \varphi \leq \pi) \quad (2.6)$$

The expansions are defined as follows:

$$\gamma_b = 2 \left[\frac{+\gamma_s}{\sin \varphi} - \frac{\gamma_0 \cos \varphi}{\sin \varphi} + \sum_{n=1}^{\infty} \gamma_n \sin(n\varphi) \right] \quad (2.7)$$

$$\Delta P = 2\rho \left[\frac{+\tau_s}{\sin \varphi} - \frac{\tau_0 \cos \varphi}{\sin \varphi} + \sum_{n=1}^{\infty} \tau_n \sin(n\varphi) \right] \quad (2.8)$$

It follows that $\Gamma = 2\pi b(\gamma_s + \gamma_0/2)$. Similarly, the blade deformation, velocity, and induced flow may be expressed as expansions in the Glauert variable.

$$h = \sum_{n=0}^{\infty} h_n \cos(n\varphi) \quad (2.9)$$

$$w = \sum_{n=0}^{\infty} w_n \cos(n\varphi) \quad (2.10)$$

$$\lambda = \sum_{n=0}^{\infty} \lambda_n \cos(n\varphi) \quad (2.11)$$

The $\cos(n\varphi)$ terms in Eqs. (2.9)-(2.11) are equivalent to the Chebychev polynomials, $T_n(x/b)$. These shape functions are quite intuitive, as illustrated in Fig. 2.2. The first three correspond to plunge, pitch and camber respectively.

One can simplify the pressure expression in Eq. 2.8, by means of the Kutta condition:

$$\tau_s = f\tau_0 \quad (2.12)$$

where f is the reversed-flow parameter. This is needed to enforce the condition that $\Delta P = 0$ at the trailing edge. When the flow reverses, the leading and trailing edges are interchanged, so the sign of f must also change. In general, there are various choices of f to account for reversed flow. For instance, if $f \equiv \text{sgn}(u_0)$, the loads will change sign instantaneously (full reversed flow). For a smoother transition to the reversed flow region, one could define $f \equiv \cos \alpha$ (soft reversed flow). Alternatively, one can neglect reversed flow by setting $f = 1$. Some assumption must be made for helicopters in forward flight, where reversed flow exists. However, since the data correlated in this thesis are for two-dimensional wind tunnel tests, there is no reversed flow; and the value of f will be set equal to unity.

The airloads can be expressed in terms of the circulation γ_n (and $\dot{\gamma}_n$) by use of expansion of the vorticity equation, Eq. (2.4) and the expansion in Eq. (2.7). The left-hand side of Eq. (2.1), along with the expression for \bar{v} in Eq. (2.2), then allow the substitution $\gamma_n = w_n - \lambda_n$. That equation can then be simplified by the addition of Eq. (2.5)—with the expansion in Eq. (2.11)—to obtain a loads equation entirely in terms of w_n and λ_0 .

$$\begin{aligned} u_0(w_0 - \lambda_0) &= \tau_0 \\ b(\dot{w}_0 - \frac{1}{2}\dot{w}_2) + u_0w_1 &= \tau_1 \\ \frac{b}{2n}(\dot{w}_{n-1} - \dot{w}_{n+1}) + u_0w_n &= \tau_n \quad n > 2 \end{aligned} \quad (2.13)$$

The generalized loads are determined by substitution into the following relation from virtual work:

$$L_n = \int_{-b}^{+b} \Delta P \cos(n\varphi) dx = - \int_0^\pi b\Delta P \cos(n\varphi) \sin \varphi d\varphi \quad (2.14)$$

The final results for the generalized loads are:

$$\begin{aligned} L_0 &= -2\pi\rho bfu_0(w_0 - \lambda_0) - \pi\rho bu_0w_1 - \pi\rho b^2(\dot{w}_0 - \frac{1}{2}\dot{w}_2) \\ L_1 &= \pi\rho bu_0(w_0 - \lambda_0) - \frac{1}{2}\pi\rho bu_0w_2 - \frac{1}{8}\pi\rho b^2(\dot{w}_1 - \dot{w}_3) \\ L_2 &= \frac{1}{2}\pi\rho bu_0(w_1 - w_3) + \frac{1}{2}\pi\rho b^2(\dot{w}_0 - \frac{1}{2}\dot{w}_2) - \frac{1}{12}\pi\rho b^2(\dot{w}_2 - \dot{w}_4) \\ L_n &= \frac{1}{2}\pi\rho bu_0(w_{n-1} - w_{n+1}) + \frac{1}{4(n-1)}\pi\rho b^2(\dot{w}_{n-2} - \dot{w}_n) \\ &\quad - \frac{1}{4(n+1)}\pi\rho b^2(\dot{w}_n - \dot{w}_{n+2}) \quad n \geq 3 \end{aligned} \quad (2.15)$$

The generalized loads above also correspond to the virtual work of each shape function described earlier. For instance, the load L_0 is a uniform force acting in the negative y -direction; i.e. the negative of the conventional definition of lift. The load L_1 is a linear force distribution, so the quantity $L_1x/2$ is the conventional nose-up pitching moment about the mid-chord. The first two generalized loads are sufficient to determine the lift and pitching moment about any point on the airfoil. However, if other airloads

are desired, for instance flap-hinge moment, other generalized loads would participate in the expansion.

The total bound circulation is found to be:

$$\Gamma = 2\pi b \left[f(w_0 - \lambda_0) + \frac{1}{2}w_1 - \frac{1}{2}\lambda_1 \right] \quad (2.16)$$

Although the local lift is always perpendicular to the local airfoil surface, there is also a leading-edge suction load along the airfoil. These loads combine and can create a component of lift in the direction of the free stream, which can be either induced drag or a propulsive force. [Although classical thin-airfoil theory does not give profile drag, quasi-steady profile drag can be incorporated based on experimental data]. The total induced drag is given by

$$D = \int_0^\pi b (\Delta P) (\partial h / \partial x) \sin \varphi \, d\varphi - 2\pi \rho b f (w_0 - \lambda_0)^2 \quad (2.17)$$

where a negative value implies a propulsive force.

The generalized loads, circulations, and drag may then be written in terms of blade motions and deformations $h_n(t)$ through the right-hand side of Eq. (2.1).

$$\begin{aligned} w_0 &= v_0 + \dot{h}_0 + u_0 \sum_{n=1,3,5}^{\infty} n h_n / b \\ w_1 &= v_1 + \dot{h}_1 + 2u_0 \sum_{n=2,4,6}^{\infty} n h_n / b \\ w_m &= \dot{h}_m + 2u_0 \sum_{n=m+1, m+3}^{\infty} n h_n / b \quad m \geq 2 \end{aligned} \quad (2.18)$$

Equations (2.15-2.17) form the basis of the airloads theory. They can be written more compactly in matrix form as follows:

$$\begin{aligned} \frac{1}{2\pi\rho} \{L_n\} = & -b^2[M] \left\{ \ddot{h}_n + \dot{v}_n \right\} - bu_0[C] \left\{ \dot{h}_n + v_n - \lambda_0 \right\} - u_0^2[K] \{h_n\} \\ & - b[G] \{ \dot{u}_0 h_n - u_0 v_n + u_0 \lambda_0 \} \end{aligned} \quad (2.19)$$

$$\frac{1}{2\pi} \Gamma = b \{1\}^T [C - G] \left\{ \dot{h}_n + v_n - \lambda_1 \right\} + u_0 \{1\}^T [K] \{h_n\} \quad (2.20)$$

$$\begin{aligned} \frac{1}{2\pi\rho} D = & -b \left\{ \dot{h}_n + v_n - \lambda_0 \right\}^T [S] \left\{ \dot{h}_n + v_n - \lambda_0 \right\} + b \left\{ \ddot{h}_n + \dot{v}_n \right\}^T [G] \{h_n\} \\ & - u_0 \left\{ \dot{h}_n + v_n - \lambda_0 \right\}^T [K - H] \{h_n\} + \{ \dot{u}_0 h_n - u_0 v_n + u_0 \lambda_0 \}^T [H] \{h_n\} \end{aligned} \quad (2.21)$$

where $[K]\{h_n\}$ may be alternatively written in terms of the generalized gradients, $[K]\{h_n\} = b[K']\{h'_n\}$. The definitions of the various matrices and vectors are given in Appendix A.

2.2 Two-dimensional Dynamic Inflow Model

As described above, the state-space airloads theory requires knowledge of the λ_0 component of the induced flow. [To obtain the total bound circulation, one also needs λ_1 .] There are various models that could provide the induced flow. For a helicopter in forward flight, the Peters-He 3D Dynamic Inflow model could be used [40] [41]. However, for consideration of airloads in two dimensions, a two-dimensional dynamic inflow model is used. Reference [5] utilizes a potential function expansion of the induced wake velocity, expressed in functional form. Application of the identity in Eq. (2.5) gives the resulting differential equation for the generalized inflow states:

$$\begin{aligned} b \left(\dot{\lambda}_0 - \frac{1}{2} \dot{\lambda}_2 \right) + u_0 \lambda_1 &= \frac{\dot{\Gamma}}{\pi} \\ \frac{b}{2n} (\dot{\lambda}_{n-1} - \dot{\lambda}_{n+1}) + u_0 \lambda_n &= \frac{\dot{\Gamma}}{n\pi} \quad n \geq 2 \end{aligned} \quad (2.22)$$

[It should be noted that the induced flow coefficients are driven by the time derivative of the total circulation. This circulation includes both the lift-generating circulation

from thin-airfoil theory, as well as the changes in circulation due to dynamic stall. Thus, when dynamic stall is included in the analysis, there is a coupling between the inflow and dynamic stall equations, Fig. 1.1. This will be further illustrated in the following section.] Equation (2.22) is a system of N differential equations in $N + 1$ Glauert inflow coefficients $\lambda_0, \dots, \lambda_N$ that is valid for *any* wake model. However, one additional equation is needed based on wake geometry. Reference [5] shows that—for a flat wake— λ_0 may be approximated by the relation

$$\lambda_0 \approx \frac{1}{2} \sum_{n=1}^N b_n \lambda_n \quad (2.23)$$

with the constraint that $\sum b_n = 1$. [The Peters-He model alternatively provides λ_0 for a 3-D wake.] While there are several consistent choices for defining b_n , the augmented least squares approach produces the best approximation to classical aerodynamic theories, as given by Eq. (2.24).

$$\begin{aligned} b_n &= (-1)^{n-1} \frac{(N+n)!}{(N-n)! (n!)^2} \quad n = 1, 2, \dots, N-1 \\ b_N &= (-1)^{(N+1)} \end{aligned} \quad (2.24)$$

Equations (2.16), (2.23), and (2.24) are combined and differentiated to give the right-hand side of Eq. (2.22).

$$\dot{\Gamma} = 2\pi b \left[f \dot{w}_0 - \frac{1}{2} \{b\}^T \{\dot{\lambda}\} + \frac{(\dot{w}_1 - \dot{\lambda}_1)}{2} \right] + \dot{\Gamma}_0 \quad (2.25)$$

where Γ_0 is the change in total bound circulation due to stall. Substitution into Eq. (2.22) yields:

$$\begin{aligned} \left(\frac{1}{2} + f \right) \{b\}^T \{\dot{\lambda}\} + \dot{\lambda}_1 - \frac{1}{2} \dot{\lambda}_2 &= 2 \left(f \dot{w}_0 + \frac{1}{2} \dot{w}_1 \right) + \frac{1}{b\pi} \dot{\Gamma}_0 - \frac{u_0}{b} \lambda_1 \quad n = 1 \\ \frac{f}{2} \{b\}^T \{\dot{\lambda}\} + \frac{3}{4} \dot{\lambda}_1 - \frac{1}{4} \dot{\lambda}_3 &= \left(f \dot{w}_0 + \frac{1}{2} \dot{w}_1 \right) + \frac{1}{2b\pi} \dot{\Gamma}_0 - \frac{u_0}{b} \lambda_2 \quad n = 2 \\ \frac{f}{n} \{b\}^T \{\dot{\lambda}\} + \frac{1}{n} \dot{\lambda}_1 + \frac{1}{2n} \dot{\lambda}_{n-1} - \frac{1}{2n} \dot{\lambda}_{n+1} &= \frac{2}{n} \left(f \dot{w}_0 + \frac{1}{2} \dot{w}_1 \right) + \frac{1}{nb\pi} \dot{\Gamma}_0 - \frac{u_0}{b} \lambda_n \quad n \geq 3 \end{aligned} \quad (2.26)$$

Equation (2.26) can be written in matrix form.

$$[A]\{\dot{\lambda}\} = \{c\}(f\dot{w}_0 + \frac{1}{2}\dot{w}_1) + \frac{1}{2b\pi}\{c\}\dot{\Gamma}_0 - \frac{u_0}{b}\{\lambda\} \quad (2.27)$$

where the matrices and vectors are defined in Appendix A. The velocity vector $\{w\}$ may be expanded in terms of the blade motions and free-stream velocities with the help of Eq. (2.18), resulting in the expression:

$$\{\dot{\lambda}\} = [A]^{-1} \left[\{c\} \left(\{e\}^T \{\dot{v}_n + \ddot{h}_n\} + \frac{u_0}{b} \{f\}^T \{\dot{h}_n\} + \frac{\dot{\Gamma}_0}{2b\pi} \right) - \frac{u_0}{b} \{\lambda\} \right] \quad (2.28)$$

Equation (2.28) is the form of the induced flow equations used in the simulations here. Only the λ_0 component is required for the airloads, but the λ_n are coupled, so that several states are required. For unsteady u_0 , these equations have time-varying coefficients.

The induced-flow model may be validated by comparison to Theodorsen theory. Consider simple harmonic inflow of the form $\lambda_n = \bar{\lambda}_n e^{iku_0 t/b}$ and $w_n = \bar{w}_n e^{iku_0 t/b}$, with no dynamic stall or reversed flow. Substitution of these relations into Eq. (2.27) yields:

$$[Aik + I]\{\bar{\lambda}\} = \{c\}ik(\bar{w}_0 + \frac{1}{2}\bar{w}_1) \quad (2.29)$$

For the case $\bar{w}_0 + \frac{1}{2}\bar{w}_1 = 1$, then

$$\{\bar{\lambda}\} = [Aik + I]^{-1}\{c\}ik \quad (2.30)$$

The Theodorsen lift deficiency function $C(k)$ is given by the ratio of circulatory lift to quasisteady lift for simple harmonic motion.

$$C(k) = \frac{\bar{w}_0 + \frac{1}{2}\bar{w}_1 - \bar{\lambda}_0}{\bar{w}_0 + \frac{1}{2}\bar{w}_1} = 1 - \bar{\lambda}_0 = 1 - \frac{1}{2}\{b\}^T\{\bar{\lambda}\} \quad (2.31)$$

The exact solution, derived by Theodorsen in terms of Bessel functions is:

$$C(k) = \frac{J_1(k) - iY_1(k)}{[J_1(k) + Y_0(k)] + i[J_0(k) - Y_1(k)]} \quad (2.32)$$

A comparison of the exact and approximate Theodorsen functions is shown in Fig. 2.3. The ratio $k/(1+k)$ is plotted on the abscissa to allow comparison of the functions over the entire frequency range from $k = 0$ to $k = \infty$. Eight inflow states are used. Reference [5] shows that the 2-norm of the error for this approximation is less than 1%.

2.3 Dynamic Stall Model

In the early 1980's, the French aerospace research institute ONERA sought to develop a differential equation model of dynamic stall. This was motivated largely by rotorcraft in forward flight, where there is always a portion of the rotor on the retreating side that undergoes dynamic stall. As the blades rotate around the azimuth, some blade sections oscillate in and out of the stall regime, resulting in hysteresis of the lift and moment curves.

Figure 2.4 illustrates the phenomenon of static stall. Up to the static stall angle α_{ss} , the airfoil behaves according to linear, thin-airfoil theory. Beyond that point, the airfoil begins to stall, and there is a deficiency between the projection of the linear lift and the actual lift. That difference is the static loss of lift, denoted ΔC_L . The static loss of lift acts as a forcing function to drive the ONERA differential equation for dynamic stall. Similarly, a static loss ΔC_q may be defined for any of the airloads C_q of interest.

It is not presently possible to analyze dynamic stall fully in a purely theoretical way. However, Ref. [1] notes that physical systems may be modeled as transfer functions, with inputs and outputs. These transfer functions and their associated differential equations may be based upon experimental observation, even if the underlying physics are not completely defined. It is along this line that the ONERA dynamic stall model was developed, and extensive experimental correlations are presented in Refs. [1], [2], [31], and by others. ONERA assumed that in the linear regime (below α_{ss}), the behavior of the airloads can be described by a first-order transfer function. This is a single pole approximation to Theodorsen theory. In the stalled regime, airloads display a time delay and overshoot due to the passing of shed vorticity. In order to allow for this phenomenon, a second-order transfer function is

introduced. Thus, the form of the original ONERA model is given by Eqs. (2.33) - (2.35), where the parameters $\hat{\lambda}$, \hat{a} , \hat{s} , $\hat{\delta}$, $\hat{\eta}$, $\hat{\omega}$, and \hat{e} are determined by parameter identification.

$$C_L = C_{L1} + C_{L2} \quad (2.33)$$

$$C_{L1}^* + \hat{\lambda}C_{L1} = \hat{\lambda}\hat{a}\theta + (\hat{\lambda}\hat{s} + \hat{\delta})\theta^* + \hat{s}\theta^{**} \quad (2.34)$$

$$C_{L2}^{**} + \hat{\eta}C_{L2}^* + \hat{\omega}^2C_{L2} = -\hat{\omega}^2 \left[\Delta C_L + \hat{e} \frac{\partial \Delta C_L}{\partial \theta} \theta^* \right] \quad (2.35)$$

[Implicit in the ONERA derivation is a steady free-stream velocity.] Equation (2.34) in the ONERA model is for calculating the linear lift coefficient, and Eq. (2.35) is for calculating the loss of lift due to dynamic stall. The results are combined in Eq. (2.33) to determine the total lift coefficient. ONERA found that correlation could be improved by introduction of a pure time delay for the onset of stall, following the work of Beddoes [42] [43]. However, this pure time delay introduces an infinite number of states into the system. Therefore, in the work here, we will deal with differential equations without pure time delay.

References [44] and [3] note that the ONERA model may be written alternately in terms of either lift coefficient C_L , nondimensional circulation $\bar{\Gamma} = UC_L$, or nondimensional lift, $\bar{L} = U^2C_L$ (where U is the nondimensional free-stream velocity). For example, the alternate forms of the linear lift coefficient in Eq. (2.34) become:

$$\bar{\Gamma}_1^* + \hat{\lambda}\bar{\Gamma}_1 = \hat{\lambda}\hat{a}U\theta + (\hat{\lambda}\hat{s} + \hat{\delta})U\theta^* + \hat{s}U\theta^{**} \quad (2.36)$$

$$\bar{L}_1^* + \hat{\lambda}\bar{L}_1 = \hat{\lambda}\hat{a}U^2\theta + (\hat{\lambda}\hat{s} + \hat{\delta})U^2\theta^* + \hat{s}U^2\theta^{**} \quad (2.37)$$

(Similar alternate versions also exist for the C_{L2} equation.) For a steady free stream, these three forms are exactly equivalent, so any of the three may be considered the original ONERA model. If an unsteady free stream is considered, the three forms are not the same, due to \dot{U} terms that arise from the transformation of one form to the other. Using the flap response of a simplified rotor, Peters and Rudy showed that the original ONERA formulation, using lift coefficient, has an instability that can occur at large angles of attack. They determined that the formulation of the model that is best behaved and agrees most closely with experimental data is Eq. (2.36), in terms of circulation. This is intuitive, as dynamic stall is the result of lost circulation as

vortices are shed at the leading edge. In addition, they showed that angle of attack due to plunge must be treated independently from that due to pitch. Third, they showed that apparent mass lift should not be treated by the same transfer function that is used for circulatory lift. They then made appropriate modifications to the ONERA model based on these observations, and these modifications extended the model into the rotorcraft regime, allowing an unsteady free stream velocity, large angles of attack, and plunge. ONERA ultimately adopted the changes proposed by Peters and Rudy [2].

The final form of the modified ONERA model in a rotating reference frame, with velocities divided into x and y components, is

$$\bar{k} \overset{+}{\Gamma}_1 + \hat{\lambda} \bar{\Gamma}_1 = \hat{\lambda} \hat{a} U + \delta \bar{b} \hat{e} \quad (2.38)$$

$$\bar{k}^2 \overset{++}{\Gamma}_2 + \bar{k} \hat{\eta} \overset{+}{\Gamma}_2 + \hat{\omega}^2 \bar{\Gamma}_2 = -\hat{\omega}^2 \left[U \Delta C_L + \hat{e} \bar{k} \left(\overset{+}{U} \Delta C_L + \frac{\partial \Delta C_L}{\partial \theta} \overset{+}{U} \right) \right] \quad (2.39)$$

where $(\overset{+}{\cdot})$ implies differentiation with respect to nondimensional time based on the average u_0 , $\bar{k} = b/r$, $\bar{b} = b/R$, and \hat{e} is the rotation rate of the airfoil with respect to the air mass.

In general, these differential equations have time-varying coefficients that will depend upon a dynamically varying angle of attack. ONERA identifies these parameters by dynamic perturbations about a number of mean angles of attack. Thus, an assumption is made that the coefficients change sufficiently slowly to allow the perturbation results to define the coefficients. Experience has shown that good results can be achieved with the model if the stall parameters are identified carefully in this manner [1]. ONERA and NASA ran a series of small-amplitude tests to determine the stall parameters, linearized about various mean angles of attack, Refs. [1], [31]. From these tests the functional form of the stall coefficients was determined to be

$$\begin{aligned} \hat{\omega} &= \omega_0 + \omega_2 (\Delta C_L)^2 \\ \hat{\eta} &= \eta_0 + \eta_2 (\Delta C_L)^2 \\ \hat{e} &= e_2 (\Delta C_L)^2 \end{aligned} \quad (2.40)$$

In the sections to follow, this Peters/ONERA approach for stall will be generalized and then integrated into the dynamic stall approach. However, we will not use the crude first-order approximation for linear circulation expressed by Eq. (2.34). Rather, we will utilize the more accurate 8-state version of the Karunamoorthy model.

2.4 The Unified Model

2.4.1 Theory

The fundamental concept of the unified model is to begin with the flexible airfoil theory of section 2.1, but then to correct each generalized loading L_n with its own ONERA-like stall correction. In order to avoid the confusion that often arises due to the different nondimensional definitions of the classical ONERA approach, we further elect to write both the linear loads and the stall corrections in dimensional form. Thus, the linear airloads are calculated by the Johnson/Peters state-space airloads theory with an appropriate inflow model, Eqs. (2.19) through (2.21). Simultaneously, the total load including dynamic stall for each generalized coordinate is computed as follows:

$$\begin{aligned} \frac{b^2}{u_T^2} \ddot{\Gamma}_n + \eta \frac{b}{u_T} \dot{\Gamma}_n + \omega^2 \Gamma_n \\ = -b u_T \omega^2 \left[\Delta C_n + e \frac{d\Delta C_n}{dt} \frac{b}{u_T} \right] \end{aligned} \quad (2.41)$$

where the total derivative $d(\Delta C_n)/dt$ is accomplished through the chain rule with respect to all appropriate variables, $[\partial(\Delta C_n)/\partial z] \dot{z}$.

$$\begin{aligned} L_n &= L_{n(\text{linear})} + \rho u_T \Gamma_n \\ \Gamma &= \Gamma_{n \text{ linear}} + \Gamma_0 \end{aligned} \quad (2.42)$$

Thus, the stall corrections feed back through the induced flow in Eq. (2.25) and modify the linear airloads. The lift and moment coefficients (along with any other loads of interest) can then be calculated from the generalized loads. The result is a hierarchical unsteady airloads theory for morphing airfoils in dynamic stall.

One of the benefits of the morphing airloads theory presented here is that one does not need to assume that linear lift is oriented in a particular direction. Rigorous application of the definitions of the free-stream velocities and generalized airfoil motions give both the x and y components of lift and thus orient the lift vector correctly, without small angle assumptions. In application of the stall corrections, on the other hand, we must make some assumptions about the direction of lift and drag. Since the stall model is set in a flow-based reference system, it is logically consistent to assume that the stall corrections to lift and drag are perpendicular to and parallel to the local free-stream direction. However, the local free stream can change direction rapidly; and it is not clear a priori whether or not the lift and drag should be allowed such rapid tilt.

Results have shown best correlation with data when the dynamic stall loads are oriented with respect to a time-averaged free-stream velocity. To account for this, the u_T term in Eqs. (2.41) and (2.42) is taken as the total averaged free-stream velocity, which is the resultant of the time-averaged horizontal and vertical velocity components. Figure 2.5 illustrates the directions of the various aerodynamic forces within this reference frame. The time averaging of the free-stream velocity components is accomplished by a first order filter.

$$\left(T \frac{b}{u_T}\right) \dot{\bar{v}}_L + \bar{v}_L = v_0 + \dot{h} - \lambda_0 \quad (2.43)$$

$$\left(T \frac{b}{u_T}\right) \dot{\bar{u}}_0 + \bar{u}_0 = u_0 \quad (2.44)$$

$$u_T = \sqrt{\bar{u}_0^2 + \bar{v}_L^2} \quad (2.45)$$

In Eqs. (2.43) through (2.45) above, T is a non-dimensional characteristic time constant. We propose a value of $T = 15\pi$. This attenuates velocity fluctuations over one rotor revolution by a factor of $1 - 1/\sqrt{1 + (kT)^2}$. For typical helicopters, where once-per-rev reduced frequencies are on the order of $k = 0.1$, this is an attenuation of about 79%. However, lower-frequency variations due to maneuvering flight are attenuated less. If desired, the value of T could be refined from flight-test data. The

total lift and drag forces in the large angle reference frame are then given by

$$L_{T0} = L_0 - \rho \bar{u}_0 \Gamma_0 - \rho b c_d u_T \bar{v}_L \quad (2.46)$$

$$D_T = D - \rho \bar{v}_L \Gamma_0 + \rho b c_d u_T \bar{u}_0 \quad (2.47)$$

[Note that L_0 is in the negative y direction, and D is in the positive x direction.]

2.4.2 Application

To illustrate how the above is integrated into a unified model, consider the case of an airfoil with a trailing-edge flap. A flap deflection results in an effective change in airfoil shape. In theory, to apply the ONERA dynamic stall model, static data should be known for each combination of flap deflection β and angle of attack α . However, the collection of static stall data at all combinations of α and β (followed by dynamic perturbations about each combination to identify the dynamic stall coefficients) is impractical. Here, we choose to represent stall behavior in terms of the Glauert expansion terms rather than discrete airfoil geometry changes. In so doing, existing static wind tunnel data are leveraged to generate a general stall model for a morphing airfoil, which can be used for a wide variety of configurations. In this approach, stall is represented by just enough generalized coordinates to capture the essential physical behavior. Typically, three terms of the expansion are sufficient; however, additional terms could be used if desired.

For example, published data on cambered NACA \overline{mp} 12 airfoils provide a static stall database for morphing of the NACA 0012 airfoil. The static stall model is couched in terms of the generalized spatial gradients h'_0 , h'_1 , and h'_2 . Further, it is assumed that data collected at a low Mach number may be scaled up to higher Mach numbers, as demonstrated by Ref. [29]. It is shown in Chapter 3 that, to first order, one can determine any airload on any type of morphing airfoil by using a single set of static stall data and a single set of stall parameters for a given airfoil family. This will be expanded in greater detail in Chapter 3.

2.5 Static Correction Factors

In order to adequately correlate experimental data, where thickness and compressibility effects exist, correction factors must be added to the theory. For example, NASA has compiled an extensive set of wind tunnel data for the NACA 0012 airfoil [45]. Thin-airfoil theory predicts the slope of the lift curve to be 2π for any thin airfoil, but analysis of the wind tunnel data shows the slope to be a function of both Reynolds number and Mach number. For Reynolds number between 2×10^6 and 2×10^7 , the lift curve slope per radian is approximated by:

$$C_{\ell_\alpha} = \frac{5.8728 + 0.2997 \log(Re/10^6)}{\sqrt{1 - M^2}} \quad (2.48)$$

Such a correction can be incorporated into the present theory by exchange of the factor of 2π in the load equation with C_{ℓ_α} from Eq. (2.48). This is equivalent to multiplying the thin-airfoil loads by a factor of $f_L = C_{\ell_\alpha}/2\pi$.

A complete analysis of the best practices for Mach number corrections can be found in Ref.[29], which validates the flexible airfoil theory and the unsteady free-stream aspects of the Peters/Johnson model. That paper correlates lift, pitching moment, and moments about the trailing-edge flap hinge at reduced frequencies of 0.098 and 0.268 and Mach numbers of 0.5 and 0.748. That reference shows that the Mach number correction factor of $\sqrt{1 - M^2}$ should be applied exactly as the Prandtl stretching variable implies. That is, it should be treated as an equivalent length stretching. Thus, the convective derivative becomes:

$$D[] = \frac{\partial}{\partial t} + \frac{u_0}{\sqrt{1 - M^2}} \frac{\partial}{\partial x} \quad (2.49)$$

Reference [29] shows that there are two alternative ways to incorporate this transform. One is to make the Mach number correction to all of the matrices in the loads equations ($[M]$, $[C]$, $[K]$, and $[G]$) and also to correct reduced time by changing b to $b\sqrt{1 - M^2}$. The second method is to make no change to reduced time but to alter the $[K]$ and $[G]$ matrices (but not $[C]$ and $[G]$) by the Mach number correction $1/\sqrt{1 - M^2}$. In either case, the best results were also found to occur when making the static correction at $M = 0$ only on the $[K]$ matrix. In the present results, we

do not scale $M = 0$ results up to other Mach numbers because we have data at the Mach numbers of interest. Also, since we correct both load and deflections, we have no need to differentiate as to which matrix we are correcting. However, the best-practice procedures of Ref. [29] would be important when using data taken at one Mach number to correlate at other Mach numbers.

The methodology of Ref. [29] is a correction on the output of the theory. However, it is possible to apply correction factors to the inputs as well. Consider the case of an airfoil with a trailing-edge flap. There are two input variables: pitch angle α and flap angle β . Inherent in the thin-airfoil theory is the assumption that a flap deflection is 100% efficient. That is, a flap deflection is assumed to change the shape of the mean camber line of the airfoil; and the lift changes accordingly. However, in reality there is significant loss of effectiveness in the flap's ability to generate lift, due to viscous effects. Reference [36] suggests several contributing factors for this loss of effectiveness: the flap operates in a thick turbulent boundary layer, the flap hinge creates an adverse pressure gradient, and gaps or protusions in the vicinity of the flap hinge alter the boundary layer. To first order, these effects may be accounted for by a simple correction factor applied to the flap deflection angle, β , to obtain an effective β . Similarly, a correction may be applied to the pitch angle α to account for viscous effects, such as those suggested by Eq. (2.48).

In general, it is more difficult to obtain good agreement with experimental pitching moment data because they depend on the lift, the shape of the camber line, and the location of the center of rotation ab , as shown in Fig. 2.6. Experience has shown that the effective center of rotation in the thin-airfoil coordinate system may need to be adjusted slightly in order to correlate experimental moment data.

In results to be presented later in Chapter 5, we will consider airfoils with trailing-edge flaps. Before the dynamic loads (stalled and unstalled) are considered, we will choose the appropriate static correction factors. Five factors are considered: 1.) correction to α , 2.) correction to β (flap angle), 3.) correction to C_L , 4.) correction to C_M , and 5.) correction to a (center of rotation). The convention for applying the

static correction factors is summarized below.

$$\{h_n\} = [T] \begin{bmatrix} f_\alpha & 0 \\ 0 & f_\beta \end{bmatrix} \begin{Bmatrix} \alpha \\ \beta \end{Bmatrix} \quad (2.50)$$

$$C_L = f_L \left(-\frac{L_0}{\rho u_0^2 b} \right), \quad C_M = f_M \left(\frac{L_1 + L_0 a_{\text{corr.}} b}{2\rho u_0^2 b^2} \right)$$

Of these five coefficients, only four are linearly independent. For instance, if the coefficients on α and β are doubled, while those on C_L and C_M are halved, the resulting loads are the same. These static correction factors will be identified from the available static airfoil data before the stall parameters are identified.

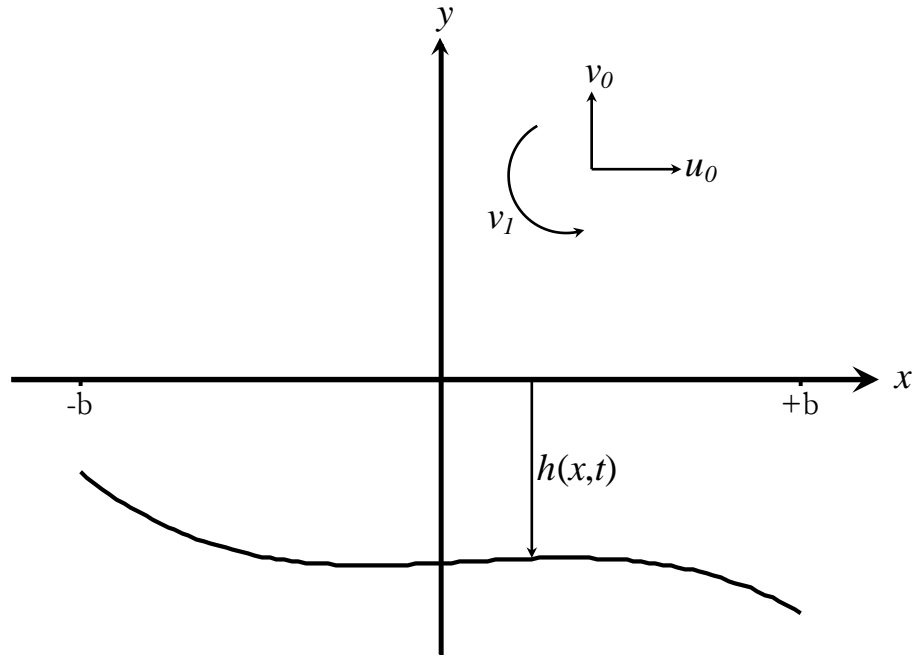


Figure 2.1: General airfoil coordinate system

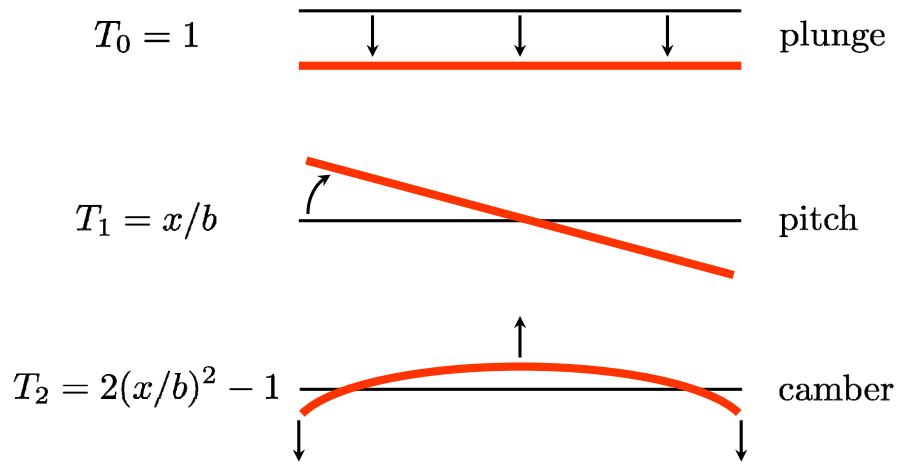


Figure 2.2: Physical significance of first three shape functions.

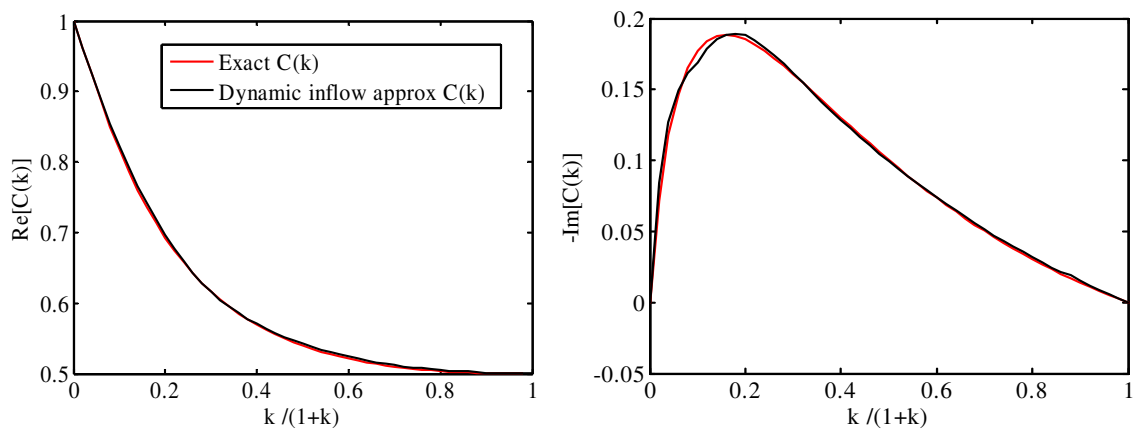


Figure 2.3: Comparison of exact and approximate Theodorsen function $C(k)$

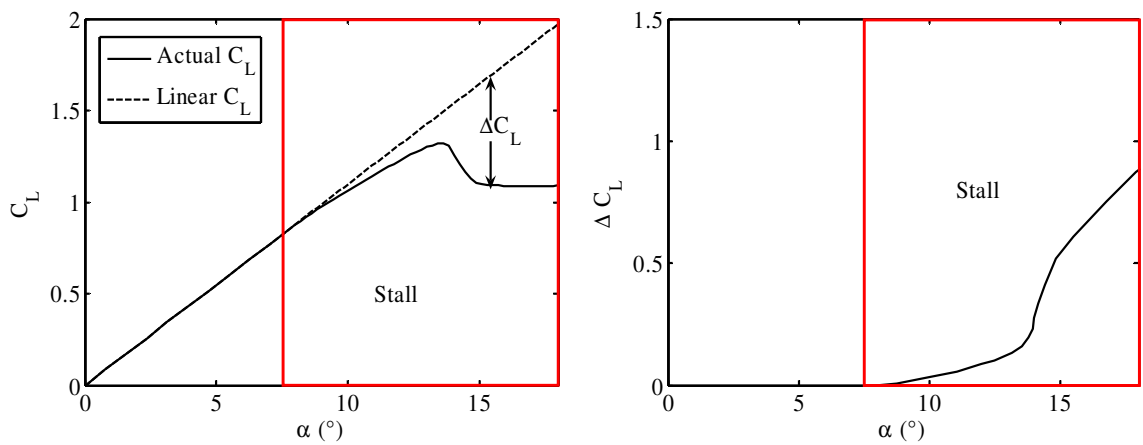


Figure 2.4: Illustration of static stall

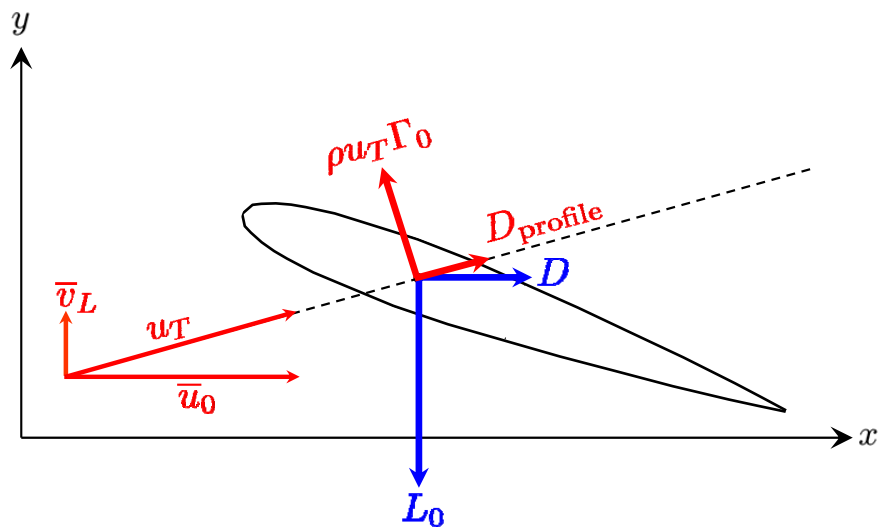


Figure 2.5: Coordinate system for large angles.

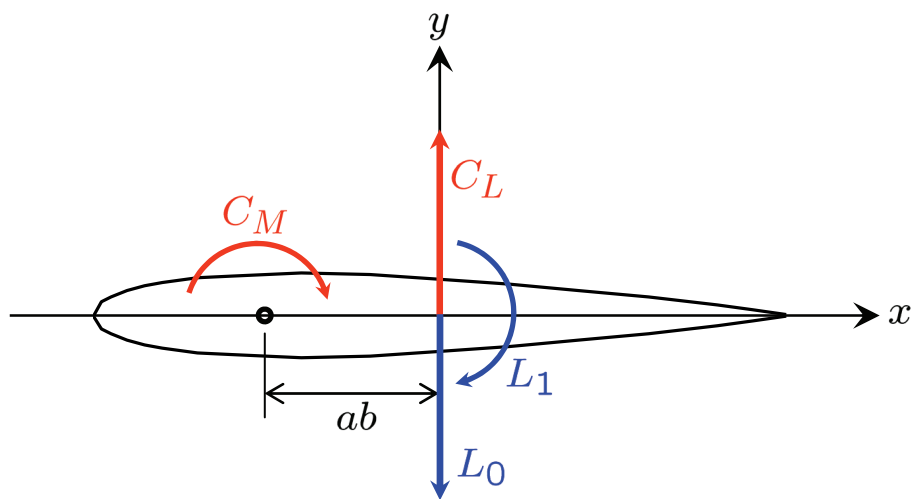


Figure 2.6: Air loads on a typical airfoil section.

Chapter 3

Static Airfoil Section Characteristics

The dynamic stall model used herein is driven by the static stall, which depends on airfoil shape. For fixed geometry airfoils, section characteristics [lift, pitching moment, and drag as a function of angle of attack] can be obtained from published airfoil tables, wind tunnel testing, boundary-layer analysis codes, or other available sources. However, morphing airfoils have static section characteristics that change with the airfoil shape. There are no tables available for morphing airfoils, and only limited wind tunnel testing is available. Reference [46] utilizes a table lookup with data generated by the XFOIL boundary-layer analysis software for a morphing airfoil. The current research uses a different approach to assemble databases of section characteristics for families of morphing airfoils. To accomplish this, one needs static airload data for the baseline airfoil, as well as for a range of values of the morphing variables of interest. The generalized spatial gradient coefficients h'_n are calculated either by a transformation from the morphing variables, or by a summation of the generalized deformations h_n . Finally, the curves are parameterized as a function of h'_n . The result is a static database which may be used for any arbitrary morphology of the baseline airfoil in terms of generalized coordinates.

In the following sections, this process is illustrated and validated for three different baseline airfoil geometries:

1. NACA 0012 12% symmetric airfoil
2. SC-1095 cambered airfoil

3. Boeing VR-12 12% cambered airfoil

All of the airfoils studied share several common characteristics. For small angles of attack, the airfoils behave linearly. From thin airfoil theory, this behavior is given by the relation

$$C_L = C_{L\alpha}(\alpha - \alpha_{0L}) \quad (3.1)$$

where α_{0L} is the angle at which zero lift is produced. Thus, the linear portions of the lift curves collapse onto a single line passing through the origin when plotted as a function of $\alpha - \alpha_{0L}$. In order to adequately correlate experimental data, where thickness and compressibility effects exist, correction factors must be added to the thin-airfoil theory, as discussed in Section 2.5.

The post-stall behaviors of each of the airfoils within a family are characteristically similar to each other. Although some differences occur due to the softening of the stall inception due to the morphing, this behavior can be approximated to first order by a single curve for each of the airfoil families. The accuracy of this approximation is in keeping with the nature of the model. The lift curve for any of these airfoils is thus obtained by a synthesis of the linear portion of the lift curve and the post-stall behavior. The transition from the linear regime to the stall regime is defined to occur at a static stall angle α_{ss} , which is assumed to be a function of the generalized coordinates.

Figure 3.1 illustrates the process of parameterizing the static lift for a morphed airfoil. The black curves indicate the baseline airfoil. The red curves indicate a notional morphed airfoil, where the baseline geometry has been modified through one or more morphing variables. This could be a trailing-edge flap, leading-edge droop, camber or any other morphology. The figure shows a four-stage process for identifying the necessary parameters.

1. Stage 1 shows the raw data plotted as a function of angle of attack, α . From these data, one may calculate the angle of zero lift α_{0L} , at which the lift curve crosses the x -axis. This is typically a negative value for a cambered airfoil. The static stall angle, where maximum lift occurs, is further denoted as α_{ss} . The subscripts _(b) or _(m) refer to baseline or morphed.

2. Stage 2 shows the data plotted as a function of $\alpha - \alpha_{0L}$. As mentioned above, this collapses the linear portion of the lift curve for each of the airfoils onto a single line. The difference between the peak of the morphed airfoil and the peak of the baseline airfoil is indicated by α_{shift} .
3. Stage 3 shows the lift residuals as a function of $\alpha - \alpha_{0L}$. The lift residuals are the *difference* between the expected linear lift given by thin-airfoil theory (including appropriate static corrections) and the experimental lift. Calculation of these residuals is discussed in more detail in following sections.
4. Stage 4 shows the lift residuals as a function of $\alpha - \alpha_{0L} - \alpha_{\text{shift}}$. This aligns the baseline and morphed curves. These curves may be averaged, or fit with a polynomial to provide the approximate static lift for any airfoil as a function of $\alpha - \alpha_{0L} - \alpha_{\text{shift}}$, where $\alpha_{\text{shift}} \equiv 0$ for the baseline airfoil.

A similar process is used for pitching moment, flap hinge moment, or any other airload of interest. As the final step, the values of α_{0L} and α_{shift} are parameterized in terms of generalized morphing variables.

Note that ΔC_L (or, for that matter, any generalized load residual ΔC_n) will be zero until α approaches the static stall angle α_{ss} . This implies that ΔC_n should be expressed (either in tabular or parametric form) in terms of $u(z - z_0)f(z)$, where $u(z - z_0)$ is the unit step function, $z = \alpha - \alpha_{ss}$, and z_0 is the value of z below which the stall residual is negligible. The selection of a suitable z_0 is left to the discretion of the user. It allows for a smooth transition from unstalled to stalled behavior at α_{ss} . To put this into the notation of Fig. 3.1 step 4, we may write z for a morphed airfoil in terms of the shifted parameters:

$$z = \alpha - \alpha_{ss(\text{m})} = [\alpha - \alpha_{0L(\text{m})} - \alpha_{\text{shift}}] - [\alpha_{ss(\text{b})} - \alpha_{0L(\text{b})}] \quad (3.2)$$

For the baseline airfoil, $\alpha_{\text{shift}} = 0$ and $_{(\text{m})}$ becomes $_{(\text{b})}$ so that $z = \alpha - \alpha_{ss(\text{b})}$.

3.1 Theoretical Background

3.1.1 Linear Airloads

From the non-penetration boundary condition at the airfoil, one may write:

$$w = u_0 \partial h / \partial x + \partial h / \partial t + v_0 + v_1 x / b = \sum_{n=0}^{\infty} w_n \cos(n\varphi) \quad (3.3)$$

For an airfoil of arbitrary shape in a steady horizontal free stream at a fixed angle of attack α , this can be simplified to

$$w = u_0(\alpha + \partial h / \partial x) = \sum_{n=0}^{\infty} w_n \cos(n\varphi) \quad (3.4)$$

where we have removed the angle of attack from $h(x)$ so that $h(x)$ contains only morphing. The spatial gradient is then expanded in a Glauert series.

$$\partial h / \partial x = \sum_{n=1}^{\infty} h'_n \cos n\varphi \quad (3.5)$$

Substitution of this expansion into Eq. (3.4) and collection of like terms gives the generalized velocities as

$$\begin{aligned} w_0 &= u_0(\alpha + h'_0) \\ w_n &= u_0 h'_n \quad n \geq 1 \end{aligned} \quad (3.6)$$

From Eq. (3.6), we see that the spatial gradient coefficients h'_n are the components of total velocity due to morphing only, non-dimensionalized on u_0 . From thin-airfoil theory, the lift coefficient is given by

$$C_L = \frac{2\pi}{u_0}(w_0 + 0.5w_1) \quad (3.7)$$

Thus the ideal zero lift condition is given by

$$\alpha_{0L} = -(h'_0 + 0.5h'_1) \quad (3.8)$$

where h'_n is the expansion of the morphing part of dh/dx . If the airfoil is symmetric, i.e. $h'_0 = h'_1 = 0$, then one recovers the flat-plate airfoil result that $\alpha_{0L} = 0$. An alternate form of Eq. (3.8) can be obtained in terms of the generalized deformations h_n , rather than in terms of the gradient.

$$\begin{aligned} \partial h / \partial x &= \sum_{n=1}^{\infty} h_n \frac{n \sin(n\varphi)}{b \sin \varphi} \\ &= \sum_{n=1,3,5,\dots}^{\infty} n \frac{h_n}{b} + \sum_{m=1}^{\infty} \cos(m\varphi) \left[\sum_{n=m+1,m+3,\dots}^{\infty} 2n \frac{h_n}{b} \right] \end{aligned} \quad (3.9)$$

Substitution of this relation into Eq. (3.5) gives the zero-lift angle in terms of the generalized deformations.

$$\alpha_{0L} = \frac{1}{b} \sum_{n=1}^{\infty} n h_n \quad (3.10)$$

Only two terms of the h'_n expansion in Eq. (3.8) are needed to determine the angle of zero lift. However, with Eq. (3.10), many more terms are required to converge to the same result in terms of h_n . This leads to a distinction in application between unstalled and stalled airloads. For the linear thin-airfoil theory, the loads are given in terms only of the airfoil deformations h_n . When analyzing stalled loads, the data are parameterized in terms of the spatial gradient coefficients, h'_n . Of course, Eq. (3.8) is only the ideal approximation to α_{0L} . When experimental data are available, they must be used to correct α_{0L} accordingly.

With the angle of zero lift established, it is convenient to plot all of the section characteristics with $\alpha - \alpha_{0L}$ on the abscissa, as motivated by Eq. (3.1). Plotted in this way, all of the curves coincide in the linear regime, and all of the curves behave similarly following the onset of stall. The distinguishing characteristic for each airfoil is the angle at which stall occurs. There is some ambiguity in the definition of this angle, as static stall occurs slowly at first, followed by a rapid change in lift and pitching moment. For instance, one could define the static stall angle as the angle at which the experimental lift differs from the linear value by some fixed amount. This can be problematic, however, as some airfoils have softer stall characteristics than others. Instead, we define the static stall angle α_{ss} as the angle corresponding to maximum C_L . From Fig. 3.1 we see that α_{shift} may be calculated in terms of α_{ss}

and α_{0L} by the following equation.

$$\alpha_{\text{shift}} = [\alpha_{ss(m)} - \alpha_{0L(m)}] - [\alpha_{ss(b)} - \alpha_{0L(b)}] \quad (3.11)$$

where (m) implies the morphed airfoil and (b) implies the baseline.

3.1.2 Static Stall Residuals

In order to implement the equations for dynamic stall, one must know the static stall residuals, (i.e., the *difference* between the thin-airfoil values for the airloads—with appropriate static corrections—and the experimental observations). In principle, the static stall residuals can be found from stage 4 of the process described in Fig. 3.1. However, for data with very large values of α (such as NACA 0012 data for $0^\circ \leq \alpha < 360^\circ$), the unstalled theory is not truly linear. For such cases, Ref. [47] shows that these residuals may be computed from experimental data by

$$\Delta C_L = C_{L0} \cos \alpha + C_{L\alpha} \sin \alpha - C_L \quad (3.12)$$

$$\Delta C_M = C_{M0} \cos^2 \alpha + C_{M\alpha} \sin \alpha \cos \alpha + \frac{a}{2} C_D \sin \alpha - C_M \quad (3.13)$$

where C_{L0} and $C_{L\alpha}$ are the magnitude and the slope of the lift curve at $\alpha = 0$, respectively; and C_{M0} and $C_{M\alpha}$ are the value and the slope of the moment curve at $\alpha = 0$. Note that calculating the residuals from the factors C_{L0} , $C_{L\alpha}$, C_{M0} , and $C_{M\alpha}$ (identified from static data) gives an empirical static correction consistent with the corrections to the airload theory discussed in Chapter 2. If one chooses not to make these static corrections, the thin-airfoil values could alternately be used [$C_{L\alpha} = 2\pi$, $C_{L0} = 2\pi(h'_0 + 0.5h'_1)$, $C_{M\alpha} = 0$, $C_{M0} = -\pi/4(h'_1 + h'_2)$]. The static residuals given by Eqs. (3.12)-(3.13) act as the forcing function for the dynamic stall equations.

The unified model also employs an unsteady approximation for drag. Thin-airfoil theory gives only the induced drag, which must be combined with the profile drag to determine the total drag. The unstalled profile drag is generally proportional to a constant plus a term proportional to α^2 . Thus, a parabola can be fit to the supplied drag data in the unstalled region, defining the unstalled profile drag. The parabolic profile drag is treated as quasi-steady. The increment in drag due to stall

beyond the parabolic shape is then defined by:

$$\Delta C_D = C_{D(\text{exp.})} - C_{D(\text{profile})} - C_{D(\text{induced})} \quad (3.14)$$

The drag residual can be processed through a dynamic filter, exactly as lift and pitching moment are, or it can be treated as quasi-steady. We will consider both approaches. Even when ΔC_D is applied as a quasi-steady correction to the induced drag, there is still some unsteadiness due to the feedback of circulation loss due to stall in the calculation of induced drag.

It is often necessary to adjust the angle at which stall onset occurs in the model to obtain good correlation to experimental data. The motivation for this correction comes from the difference between steady and quasi-steady airload data, as discussed in Ref. [48]. In the left panel of Fig. 3.2, the steady and quasi-steady experimental lift have been digitized from Ref. [48] for a Boeing VR-12 airfoil. The red curve indicates the steady lift, obtained at fixed angle of attack after the transients have decayed. The black curve indicates a quasi-steady test, where the angle of attack is varied sinusoidally at very low reduced frequency, $k = 0.003$. The solid portion of the black curve—obtained for increasing α —is very similar to the steady curve, except that the onset of stall is delayed by about 2° . For decreasing α , shown as the dashed black curve, there is significant hysteresis with a gradual recovery to the steady lift. The right-hand panel of Fig. 3.2 shows the lift residuals as calculated by Eq. (3.12). Occasionally, only quasi-steady data may be available. When that is the case (such as for the VR-12 airfoil treated below), the quasi-steady data for increasing α can be used with a negative shift in stall onset on the order of $1^\circ - 2^\circ$.

3.2 NACA 0012 Airfoil

The NACA 0012 airfoil is a 12% thick symmetric airfoil, so the airfoil meanline has no slope or curvature. We desire to create a database of static data for morphing of the 0012 airfoil. At first, it would seem that to analyze stall for a morphing airfoil, one would need to perform static tests for every possible combination of morphing variables and angle of attack. This would be quite a daunting experimental task, and would limit the value of this approach. However, we propose that a small subset of

static data at various values of the morphing variables be parameterized in terms of h'_0 , h'_1 , and h'_2 . This database can then be used to analyze any morphing airfoil in terms of these generalized coordinates, regardless of the particular morphology used to create them.

3.2.1 Definitions

To consider small perturbations in meanline geometry around the 0012 airfoil, we turn to published data on eighteen NACA four-digit airfoils, digitized from Ref. [49]. NACA four-digit airfoils are denoted $NACA\bar{m}\bar{p}xy$. The first digit \bar{m} represents the percent camber. The second digit \bar{p} is the chordwise position of the maximum ordinate, in tenths of a chord. The last two digits xy indicate the percent thickness of the airfoil. Thus, the variables $m = 0.01\bar{m}$ and $p = 0.10\bar{p}$ directly relate to the shape of the meanline (as described in Appendix B). The lift and pitching moment data are shown in the top-left panels of Figs. 3.3 and 3.4. The thickness distribution of these airfoils is identical to the 0012, but the airfoils have cambered mean lines. The data were collected in the NACA variable-density wind tunnel under uniform flow conditions—with 12% thickness and with camber ranging from 0 to 6%. The point of maximum camber ranges from 0.2 to 0.7 chord.

For NACA four digit airfoils, the shape of the mean line is known in closed form, so the velocity contributions due to mean line geometry can be computed directly. The first three terms of the expansion are given below, where $q = 2p - 1$.

$$h'_0 = \frac{4mq}{(1-q^2)^2} \left[\frac{4}{\pi} \left(q \sin^{-1} q + \sqrt{1-q^2} \right) - (1+q^2) \right] \quad (3.15)$$

$$h'_1 = \frac{4m}{(1-q^2)^2} \left[(1+q^2) - \frac{4}{\pi} \left(q \sin^{-1} q + q^2 \sqrt{1-q^2} \right) \right] \quad (3.16)$$

$$h'_2 = \frac{32m}{3\pi} \frac{q}{\sqrt{1-q^2}} \quad (3.17)$$

The complete derivation of the first four terms is included in Appendix B, as well as some useful approximations. However, only h'_0 , h'_1 , and h'_2 are considered in building the static stall model developed herein.

Table 3.1 shows the computed angle of zero lift from $-(h'_0 + 0.5h'_1)$, along with a comparison with experimental results from Ref. [49] for the eighteen airfoils being considered. In order to improve the fit of α_{0L} , an empirical correction is made with an additional term in h'_2 . The corrected angle is given by:

$$\alpha_{0L} = -0.87(h'_0 + \frac{1}{2}h'_1) + 0.087h'_2 \quad (3.18)$$

The correction factor is consistent with the correction made to the slope of the lift curve, in order to compensate for thickness and viscous effects. Equation (3.18) agrees well with experimental values of α_{0L} , as shown in the predicted results from Fig. 3.5.

In the top right panel of Fig. (3.3), lift coefficient is plotted with $\alpha - \alpha_{0L}$ on the abscissa, ensuring that each of the lift curves passes through the origin. From the location of maximum C_L , the stall angle in radians is approximated in terms of h'_1 and h'_2 by:

$$\alpha_{ss} - \alpha_{0L} = 0.293 + 0.336h'_1 + 0.403h'_2 \quad (3.19)$$

Table 3.1 compares this fit of α_{ss} with the experimental values for the eighteen airfoils. The fit is excellent. It should be noted that in Eq. (3.19), h'_0 is absent. The effect of the h'_0 term is included in the definition of α_{0L} . The combination of Eqs. (3.18) and (3.19) gives the static stall angle as:

$$\alpha_{ss} = 0.293 - 0.870h'_0 - 0.099h'_1 + 0.490h'_2 \quad (3.20)$$

The constant term in Eq. (3.20) represents the stall angle of the baseline NACA 0012 airfoil, for which $h'_0 = h'_1 = h'_2 = 0$. The stall angles of the other airfoils are shifted in proportion to their h'_n coefficients. Figure 3.6 compares the observed stall angle to the curve fit given by Eq. (3.20). The angle by which each of the morphed airfoil curves is shifted with respect to the baseline 0012 curve is given by

$$\alpha_{\text{shift}} = 0.336h'_1 + 0.403h'_2 \quad (3.21)$$

As expected, α_{shift} depends only on the morphing h'_1 and h'_2 .

The bottom-left panel of Fig. 3.3 shows the static lift residuals as functions of $\alpha - \alpha_{0L}$. It can be seen that each of the cambered airfoils has similar post-stall

behavior, but the angle at which the large increase in ΔC_L associated with static stall occurs is a function of the airfoil shape. In the bottom-right panel of Fig. 3.3, the lift residuals are plotted as a function of $\alpha - \alpha_{0L} - \alpha_{\text{shift}}$, where α_{shift} is calculated by Eq. (3.21). At this point, a single *typical* curve or polynomial fit can be used to give the static lift residual for any morphed airfoil in terms of h'_0 , h'_1 , and h'_2 . An approximate closed-form expression for the mean lift residual is given by

$$\Delta C_L \approx 0.2689 \tan^{-1}(54.54z) + 15.89(z + 0.3192)^4 + 0.4070 \quad (3.22)$$

where $z = \alpha - \alpha_{ss} = [\alpha - \alpha_{0L} - \alpha_{\text{shift}}] - [\alpha_{ss(b)} - \alpha_{0L(b)}]$, assumed greater than or equal to $z_0 = -0.3192$. Tabulated values of the mean lift residuals are given in Table 3.2.

3.2.2 Pitching Moment

As shown in top-left and top-right panels of Fig. 3.4, there is vertical offset in the moment curves due to the non-zero pitching moment created by a cambered airfoil. A fit of the data shows the moment offset to be

$$C_{M0} = -0.615(h'_1 + h'_2) \quad (3.23)$$

This is approximately 20% less than the theoretical value of $-(\pi/4)(h'_1 + h'_2)$. Again, this is consistent with the types of static corrections made in the linear airload theory. The static pitching moment residuals are shown in the bottom-left and bottom-right panels of Fig. 3.4.

For simplicity, it is assumed that stall occurs simultaneously on the lift and moment curves. Comparison of the curves shows that this approximation is reasonable. If one desired a finer texture in the model, this angle could be derived independently for pitching moment. With this assumption, α_{shift} is determined by Eq. (3.21) in the bottom-right panel. Using this approach, it is again possible to fit all of the data with a typical ΔC_M curve or a polynomial fit. An approximate closed-form expression for the mean pitching moment residual is given by

$$\Delta C_M \approx 0.0276 \tan^{-1}(54.54z) + 2.177(z + 0.3048)^4 + .0435 \quad z \geq -0.3192 \quad (3.24)$$

Tabulated values of the mean pitching moment residuals are given in Table 3.2. One can see the marked rise in residuals for angles greater than the static stall angle, $\alpha_{ss} = 0.29$ (17°).

3.3 SC1095 Airfoil

The NACA 0012 airfoil is frequently used as a baseline for demonstrating the validity of an analytical or computational approach, as was done in the previous section. However, this airfoil is not commonly used in helicopter rotors. Reference [50] presents a CFD study on various morphologies of the SC-1095 airfoil, which is used in the UH-60A helicopter. The authors consider three different morphologies: trailing-edge deflection (TED), leading-edge deflection (LED), and active twist. The latter does not involve sectional airfoil shape changes, so it is not considered here. The TED and LED geometries are generated using a non-uniform rational B-spline methodology (NURBS), with control points to ensure a smooth transition to the baseline geometry. This results in a more streamlined geometry than either a simple hinged flap or a nose droop.

The geometric details of the deflected upper and lower surfaces from the study were not released. However, only the meanline geometry is needed for analysis of airloads in the current theory. Therefore, an approximate parabolic representation of the meanline is sufficient. The geometry is illustrated in Fig. 3.7, and a detailed description of the methodology is found in Appendix C for the LED and TED geometry, respectively. As before, the static characteristics are parameterized in terms of h'_0 , h'_1 , and h'_2 . These generalized gradients are given as functions of the deflection angles (θ_{LE} or δ_{TE}) and the transition points to the baseline geometry (e or d). The leading-edge and trailing-edge deflections are considered separately in Ref. [50], but they can be combined into a single expression for the generalized deflections and gradients, as shown in Appendix C.

As verification of the mean-line approximation of Appendix C, consider the angle of zero lift. Equation (3.18) indicates that the experimentally determined angle

for a morphing 0012 airfoil is given by:

$$\alpha_{0L} = -0.87(h'_0 + \frac{1}{2}h'_1) + 0.087h'_2 \quad (3.25)$$

Based on the mean-line expansion in Appendix C, the angle of zero lift from CFD data for the SC-1095 airfoil is given by:

$$\alpha_{0L} = -0.88(h'_0 + \frac{1}{2}h'_1) - 0.012 \quad (3.26)$$

The correction factor is nearly identical to the 0012 (0.88 vs. 0.87), which indicates that the mean-line does indeed predict the zero-lift angle. The constant offset -0.012 is due to the camber of the baseline airfoil, because the SC-1095 is not symmetric. Figure 3.8 shows the correlation of the zero lift angles for both leading-edge and trailing-edge deflections. The fit is excellent.

The same four-step process used to parameterize the 0012 static data is used for the SC-1095 airfoil. The resulting fit for the shift angle is given by

$$\alpha_{\text{shift}} = 0.481h'_1 + 1.10h'_2 \quad (3.27)$$

Figures 3.9 and 3.10 show the lift and pitching moment correlations for the leading-edge deflection. Figures 3.11 and 3.12 show the correlations for the trailing-edge deflection. Figures 3.13 and 3.14 show all of the correlations on one plot. The shifted data in the bottom-right panel of Fig. 3.13 show that all fourteen morphed configurations of the baseline airfoil can be collapsed very well onto a single curve. The heavy black curve indicates the least-squares fit of all of the collapsed curves. This single curve can be used in a simulation to compute the static lift residual for any arbitrary morphing of the SC-1095 airfoil.

Note that we earlier plotted the NACA data for positive angles of attack only. Here, for the SC-1095, we plot both positive and negative angles of attack. Interestingly, the stall behavior of the residuals ΔC_L or ΔC_M at both positive and negative angles of attack (shown in Figs. 3.9-3.14) all collapse onto a single curve when shifted by the same α_{0L} and α_{shift} . There is not a separate shift required for positive and negative angles of attack (i.e., for positive and negative stall). The post-stall behavior is different for the positive and negative realms, and there are

distinctly different values of $|\alpha_{ss}|$ for the onset of stall on the negative and positive sides. Despite these differences, the curves for ΔC_L or ΔC_M at both positive and negative angles—and for either leading-edge or trailing-edge droop—collapse onto a single unified curve with only one shift parameter.

Table 3.3 gives ΔC_L and ΔC_M versus the shifted variable $\alpha - \alpha_{0L} - \alpha_{\text{shift}}$ for both positive and negative angles. On the positive side, we can see the rapid rise in the residuals for angles greater than 0.22 (12.6°). On the negative side, residuals begin to rise for angles less than -0.09 (-5.2°). These are the positive and negative shifted static stall angles. An approximate fit of ΔC_L and ΔC_M at positive angles of attack, with either leading-edge or trailing-edge morphing, and for morphing angles from -10° to $+15^\circ$, is given by the following formulas:

$$\Delta C_L \approx 0.2959 \tan^{-1}(42.76z) + 21.83(z + 0.2320)^4 + 0.4351 \quad (3.28)$$

$$\begin{aligned} \Delta C_M \approx & 0.9246 \tan^{-1}(7.940z) - 5.956z - 0.166z^2 \\ & + 50.23z^3 + 5.354z^4 - 248.9z^5 + 0.0561 \end{aligned} \quad (3.29)$$

where $z = \alpha - \alpha_{ss} = [\alpha - \alpha_{0L} - \alpha_{\text{shift}}] - [\alpha_{ss(b)} - \alpha_{0L(b)}]$; and where α_{0L} is from Eq. (3.26), α_{shift} is from Eq. (3.27), $\alpha_{ss(b)} = 0.21$ (12°), and $\alpha_{0L(b)} = -0.012$ (-0.7°). The formulas in Eqs. (3.28) and (3.29) can be considered valid for $z > -0.22$. This is equivalent to the parameter $\alpha - \alpha_{0L} - \alpha_{\text{shift}}$ being greater than 0. That all of these results can be combined in this way—and that the equations for the residuals (along with α_{0L} and α_{shift}) are each represented by unified formulas in terms of h'_n —is validation of the approach that we are using in this thesis.

The shifted data in the bottom-right panel of Fig. 3.14 show that the pitching moment data are more sensitive to the type of morphing employed. For example, for the largest positive and negative trailing-edge deflections, there is a significant curvature in the pitching moment curve, while for other morphologies the pitching moment curve is fairly linear in the small-angle regime. Thus, the correlation of ΔC_M at higher deflections has some discrepancies near the stall angle. At large angles of attack, the curves once again coalesce. The heavy black curve indicates the least-squares fit of all of the collapse pitching-moment curves, which can be used in a

numerical simulation. Reference [51] proposes a method of improving the correlation by blending the two extreme curves as a function of the generalized gradients. This method would result in improved correlations of the static data near the onset of stall.

3.4 Boeing VR-12 Airfoil

For the VR-12 airfoil considered in Ref. [33], variety of static data are available, from which the lift, moment, and drag residuals may be computed. Static curves are available for fixed nose droop angles of 0° , 5° , 10° , 15° , and 20° , and for the Variable Droop Leading Edge (VDLE) configuration. In the VDLE configuration, the leading 25% of the airfoil is fixed at zero incidence to the oncoming flow, while the remainder of the airfoil undergoes pitch oscillations ($e = 0.5$). Thus, the nose droop angle is equal to the pitch angle at all times. It is logical that the static curves for the VDLE airfoil should be a cross-plot of the fixed droop cases. For instance, at 5° angle of attack (with droop of 5°), the VDLE airfoil should intersect the curve of the 5° fixed droop airfoil. At 10° angle of attack it will follow the 10° fixed droop curve, etc. Figure 3.15 shows the static lift, moment, and drag curves for the VDLE airfoil at $M = 0.3$, as well as the fixed droop cases from 0° to 15° . The square markers indicate points at which the VDLE curve should intersect the fixed droop curves. For instance, at 5° the VDLE curve (dashed line) should intersect the 5° curve (green line). The figure shows that the VDLE static characteristics follow the predicted values from the fixed droop tests reasonably well.

Dynamic cases for the baseline VR-12 and VDLE airfoil configurations are given in Ref. [33] at Mach numbers of 0.2, 0.3, and 0.4. Each of these cases has corresponding quasi-static data from which to calculate the stall residuals directly. Therefore, for the purpose of correlating dynamic data, it is not necessary to create a generalized static database for the VR-12 airfoil. Figures 3.16 and 3.17 show the lift and pitching moment residuals for the VR-12 baseline and VDLE airfoils at each Mach number. The values have been corrected to $M = 0$, so the linear portion of the curves are expected to align. The top panels show the raw data versus α . As expected, the VDLE airfoil has a reduced lift slope due to the effective reduction in

angle of attack at the leading edge. To allow for a better comparison, the middle panels show the data plotted with $\alpha + h'_0 + 0.5h'_1$ on the abscissa. This represents the effective angle of attack, including the effects of morphing. The bottom panels shows the lift and moment residuals, ΔC_L and ΔC_M , plotted in the same way.

The effect of Mach number is clearly visible. At higher Mach numbers the onset of stall occurs earlier. This shift is more pronounced for the baseline VR-12 airfoil than the VDLE configuration. Figure 3.18 shows the static stall angle for each of the cases. The experimental data are given by the individual data points. The lines indicate a least-squares fit for the stall angle as a function of Mach number. The static stall angles are given approximately by

$$\alpha_{ss} = 0.271(1 - 2.02M^2) \quad (\text{Baseline VR} - 12) \quad (3.30)$$

$$\alpha_{ss} = 0.241(1 - 1.30M^2) \quad (\text{VDLE VR} - 12) \quad (3.31)$$

These three figures, taken together, indicate that Mach number significantly affects the onset of stall, with the onset of stall occurring at a lower angle of attack for higher Mach number flows. However, the lift and pitching moment residuals have the same general shape at each of the Mach numbers, and could be approximated by a single curve, which could be shifted as a function of Mach number.

3.5 Conclusions on Static Data

Static data have been presented for three morphing airfoils: NACA 0012, SC-1095, and VR-12. For the first two cases, the airfoil mean-line shapes are transformed into generalized slopes. The static data are then parameterized in terms of the first three components of this expansion. The result is a single static curve that can be used to predict the static section characteristics for any arbitrary morphology of the baseline airfoil. For the VR-12 airfoil, the effect of Mach number is explored. At higher Mach numbers, the airfoil tends to stall more quickly than at lower Mach numbers, and this variation in the static stall angle can be fit by a quadratic expression in M . Even though the onset of stall is affected by Mach number, the overall shape of the static

residuals is relatively independent of Mach number and can be approximated to first order by a single curve.

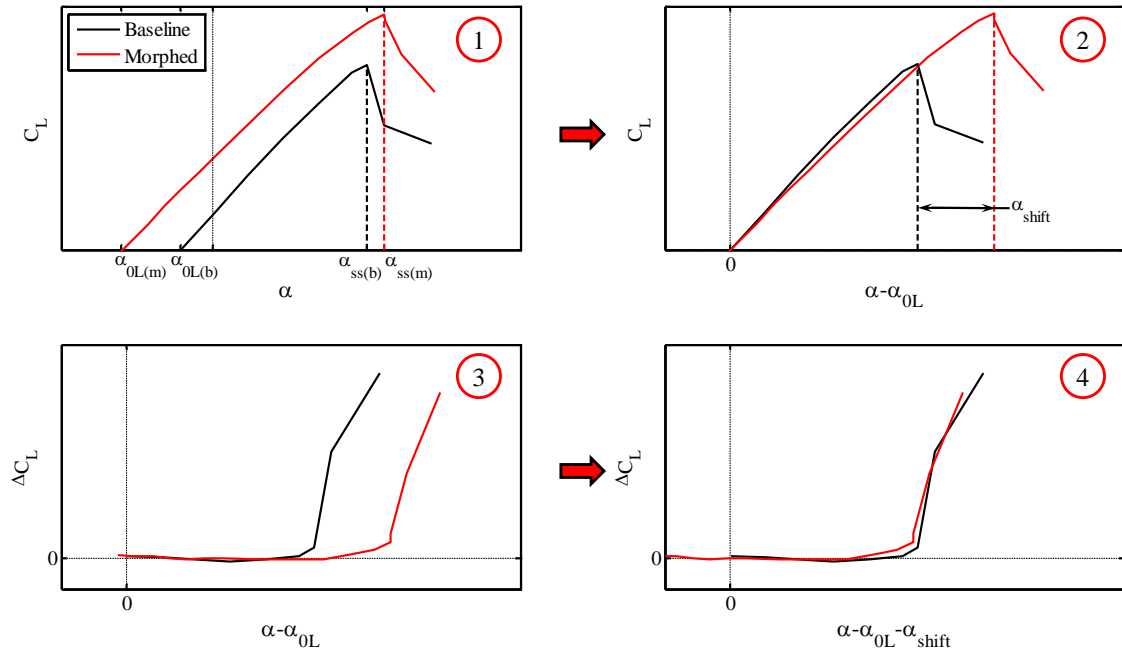


Figure 3.1: Schematic for the parameterization of static characteristics.

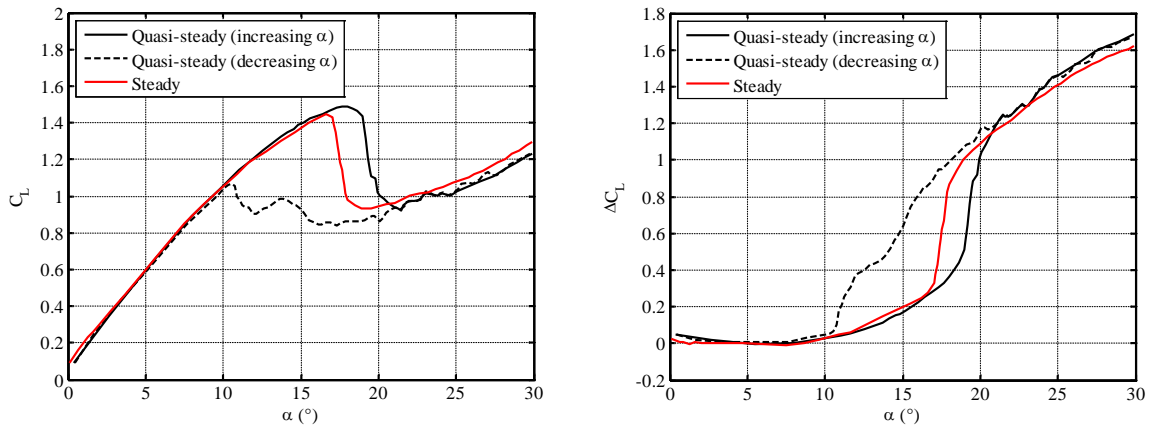


Figure 3.2: Comparison of steady and quasi-steady airloads for VR-12 airfoil.

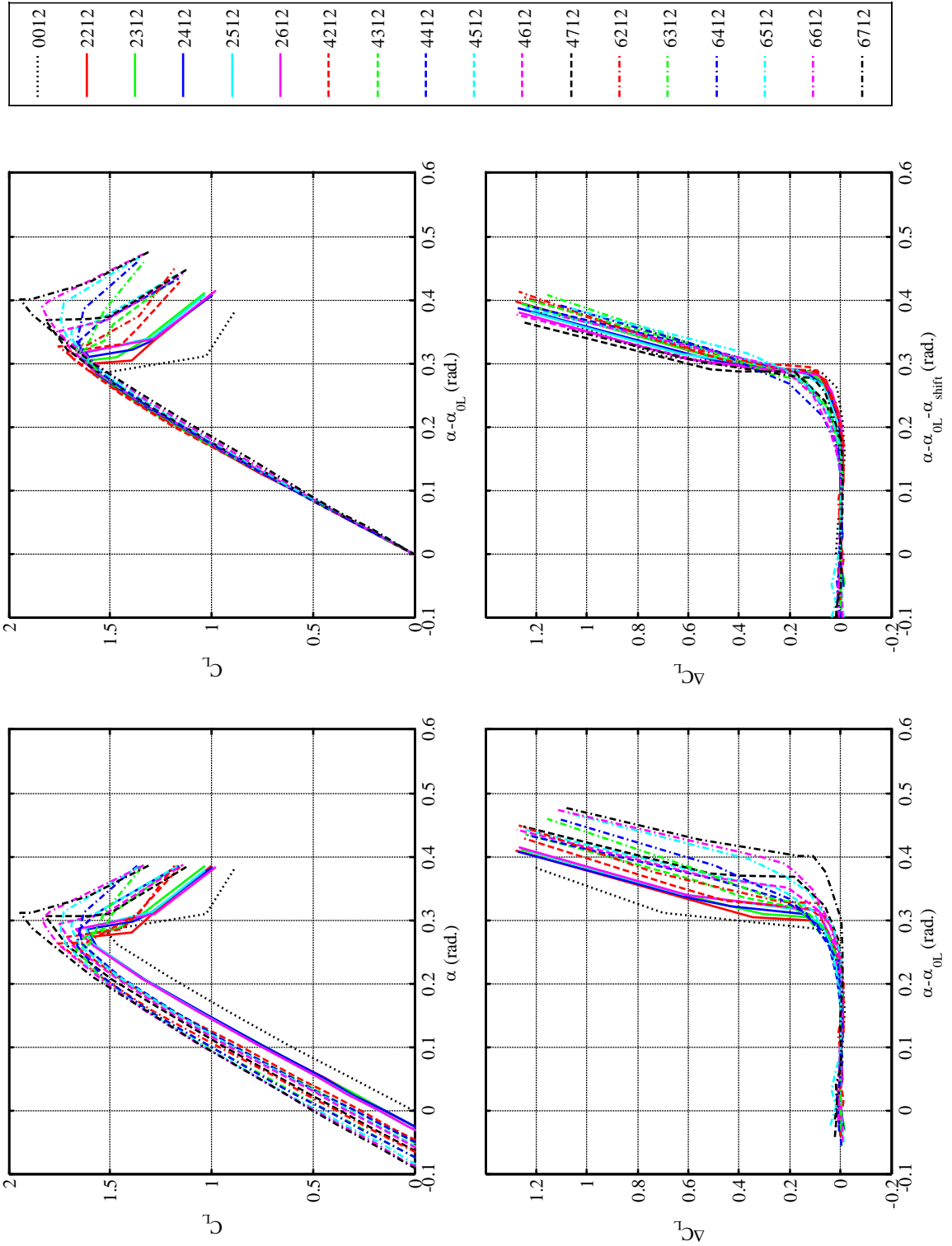


Figure 3.3: Section lift curves for NACA $\overline{m}p12$ airfoils.

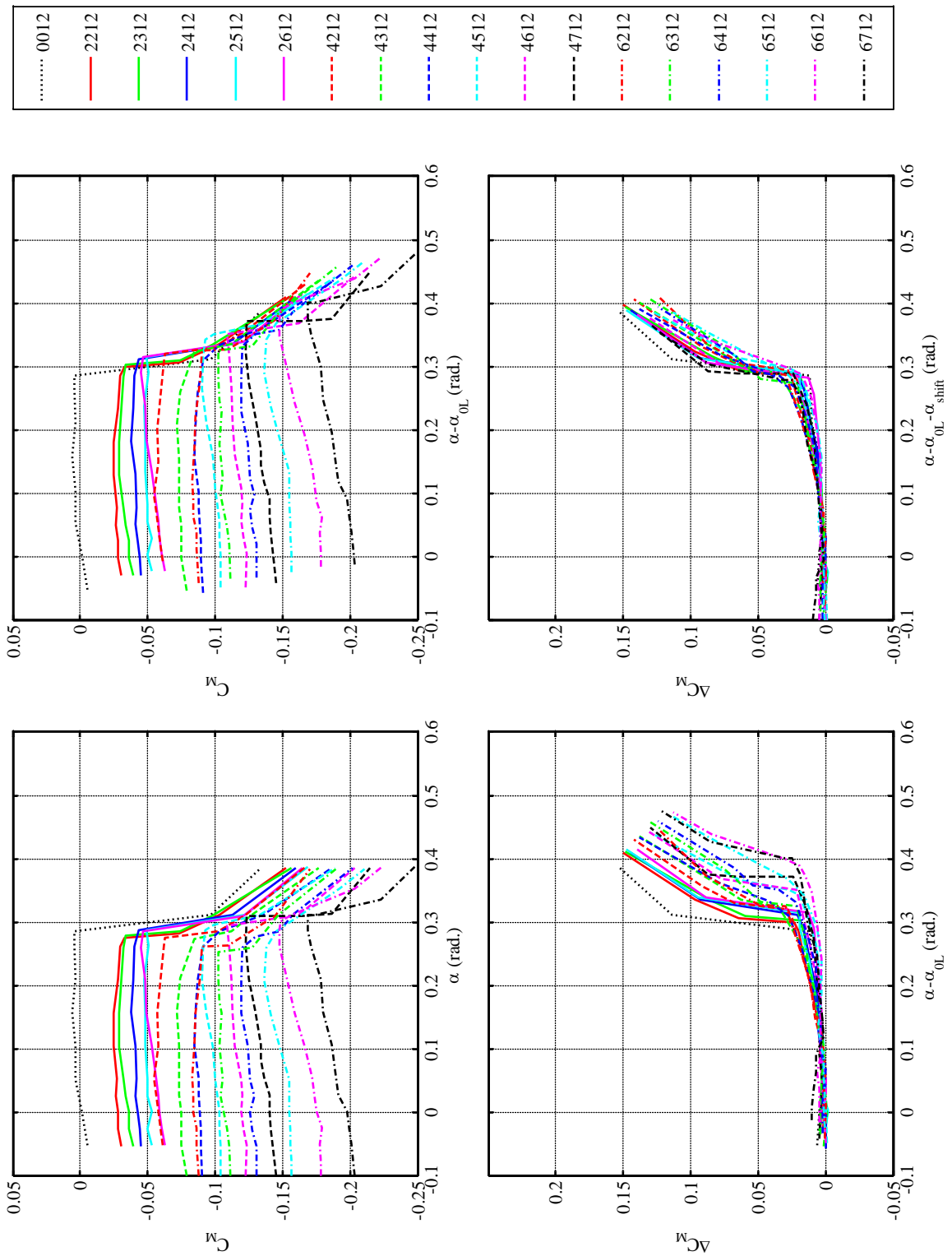


Figure 3.4: Section moment curves for NACA $\overline{mp}12$ airfoils.

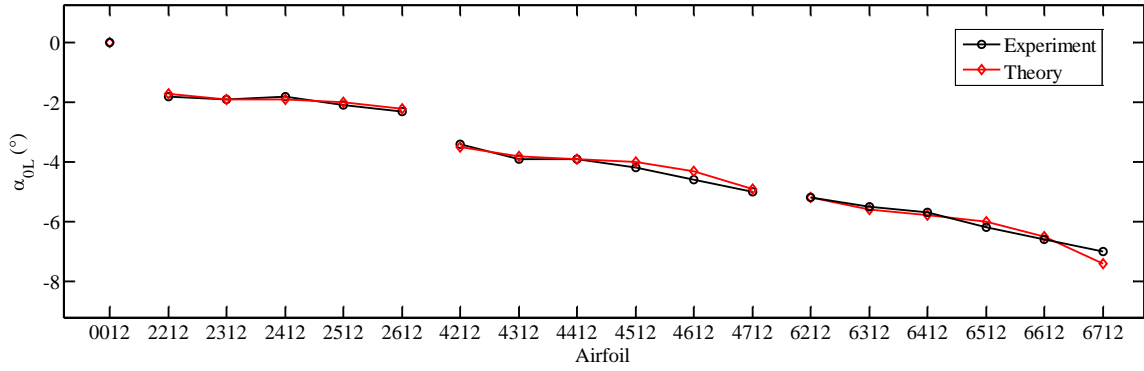


Figure 3.5: Angle of zero lift for NACA $\overline{m}p12$ airfoils.

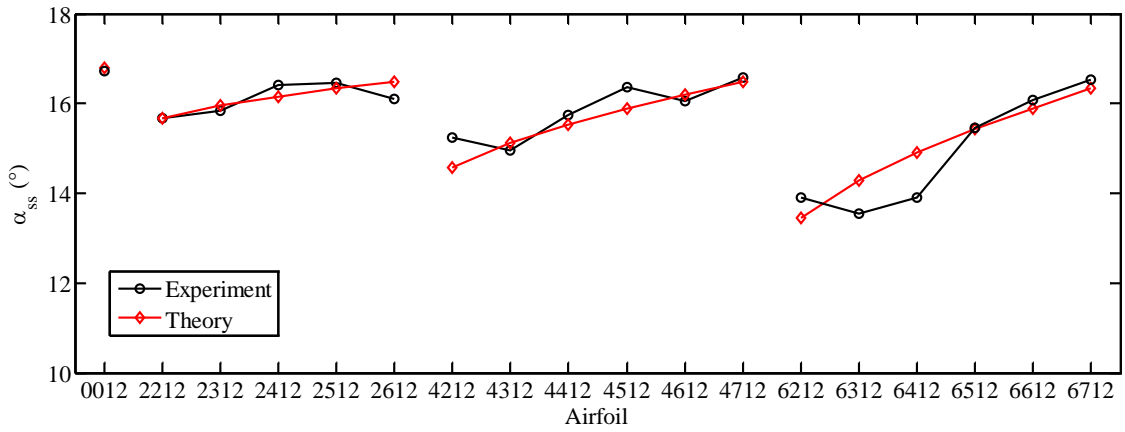


Figure 3.6: Static stall angle for NACA $\overline{m}p12$ airfoils.

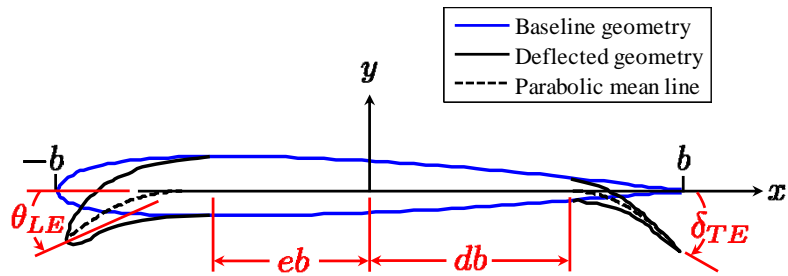


Figure 3.7: Deflected geometry for LED and TED SC1095 airfoils.

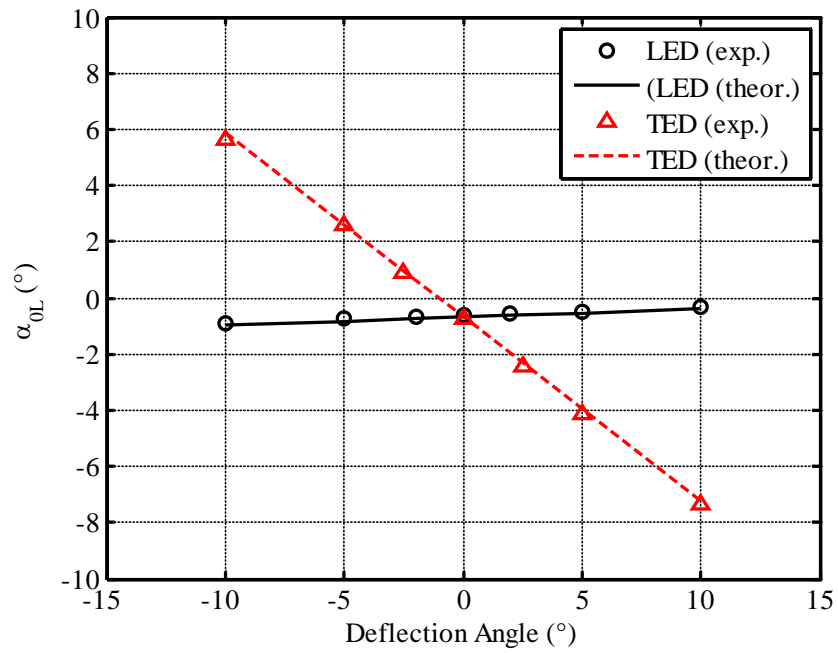


Figure 3.8: Angle of zero lift for SC-1095 airfoil with LED and TED.

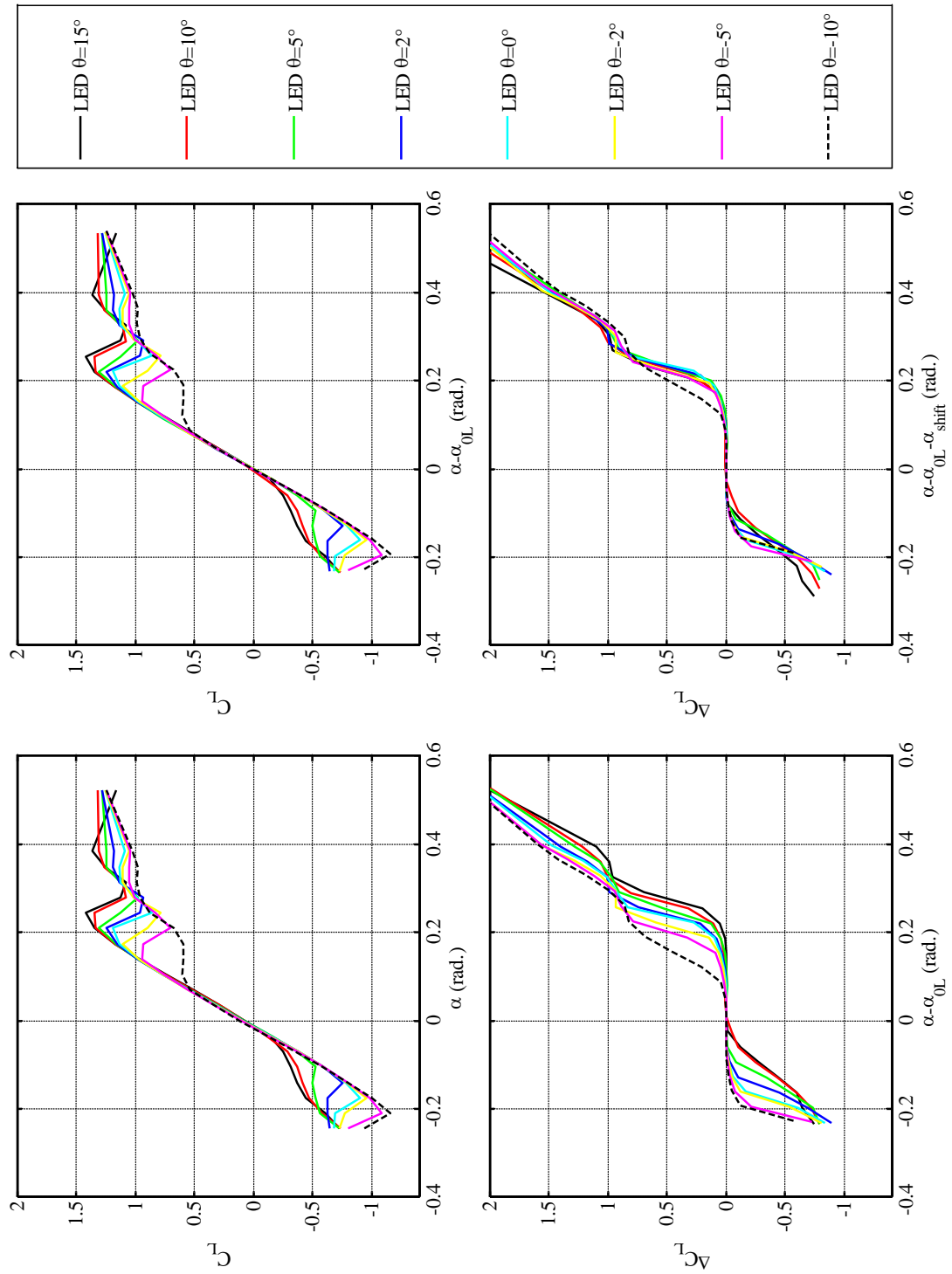


Figure 3.9: Section lift curves for SC-1095 airfoil with leading-edge deflection.

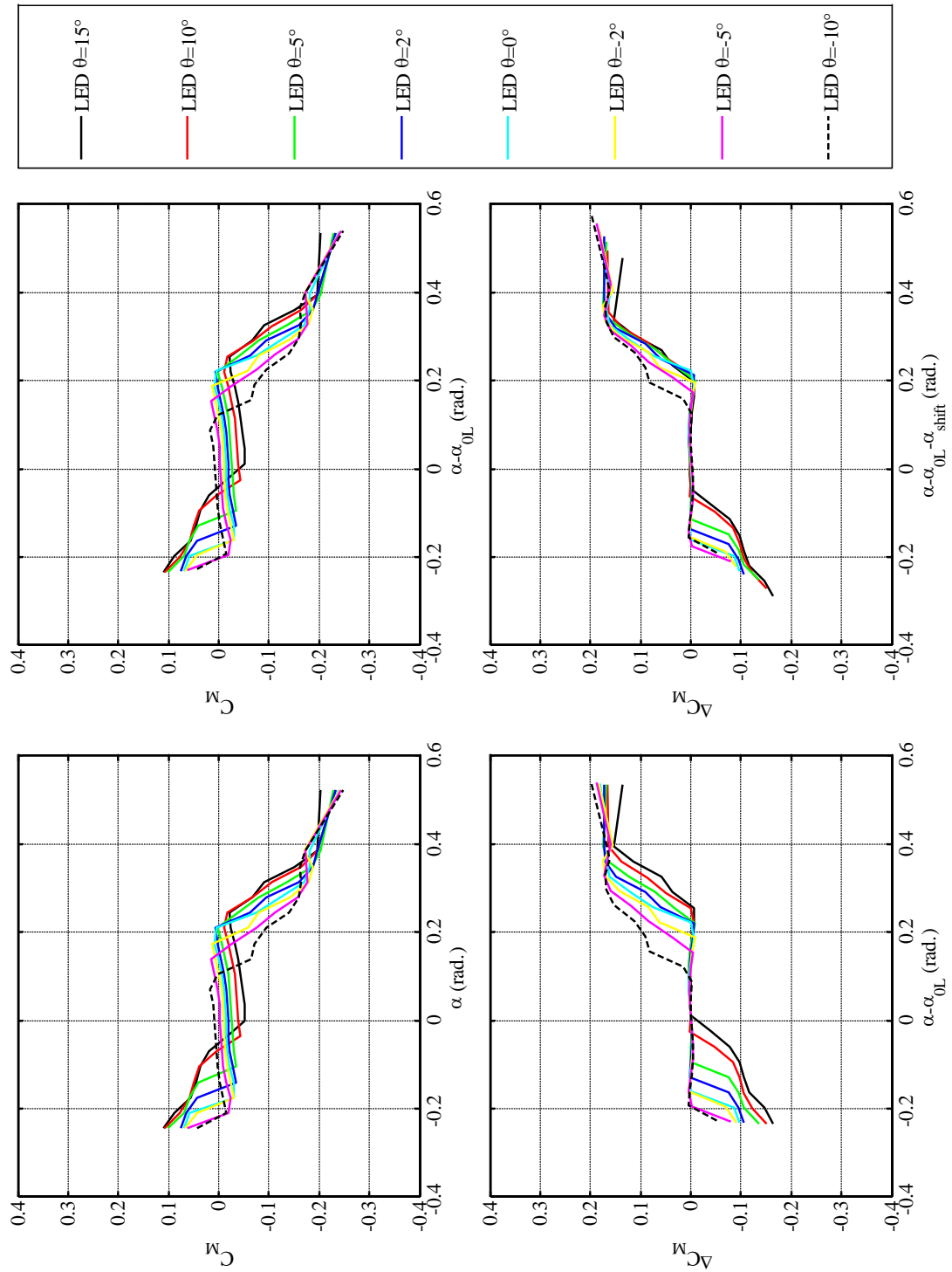


Figure 3.10: Section moment curves for SC-1095 airfoil with leading-edge deflection.

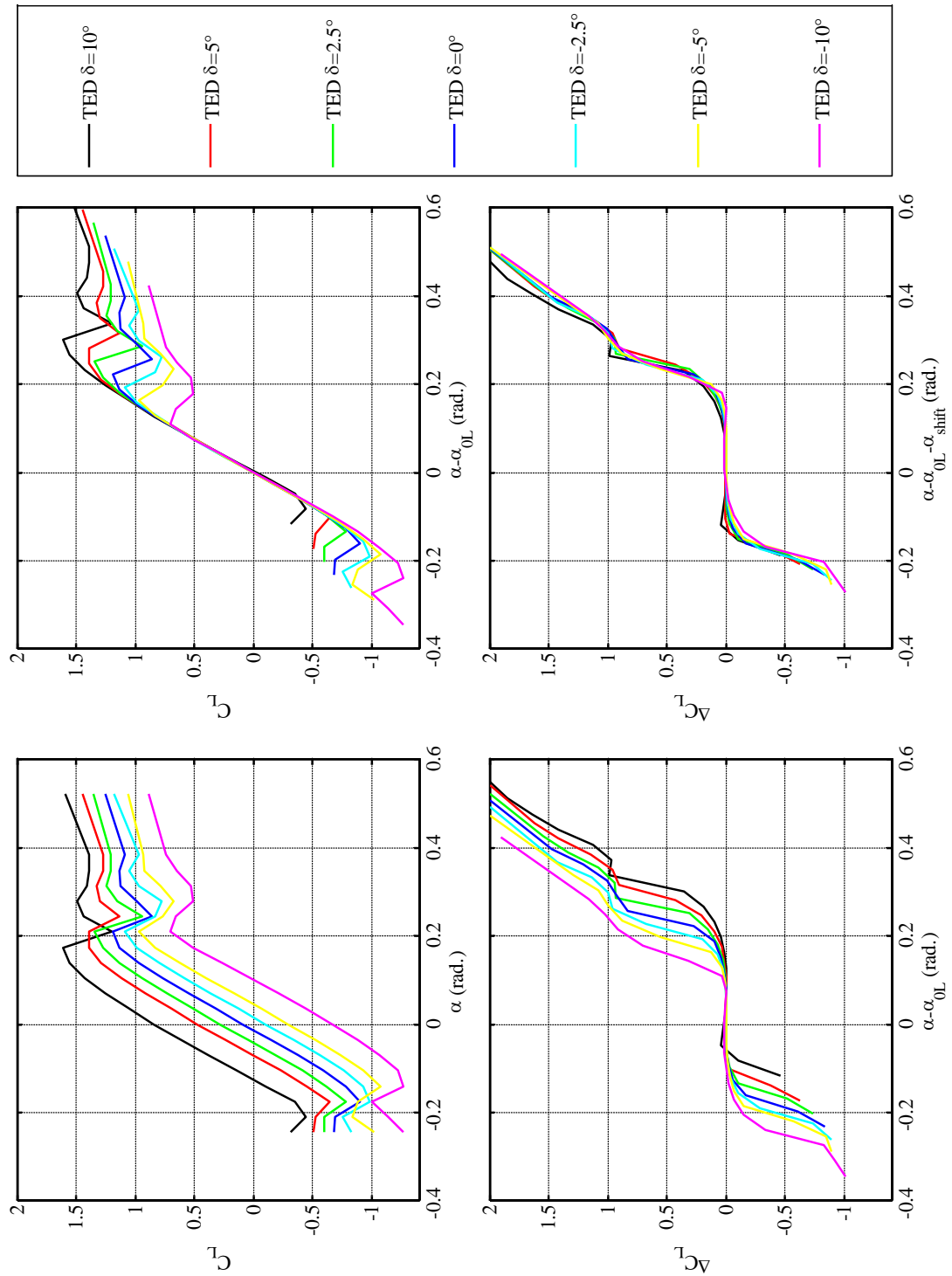


Figure 3.11: Section lift curves for SC-1095 airfoil with trailing-edge deflection.

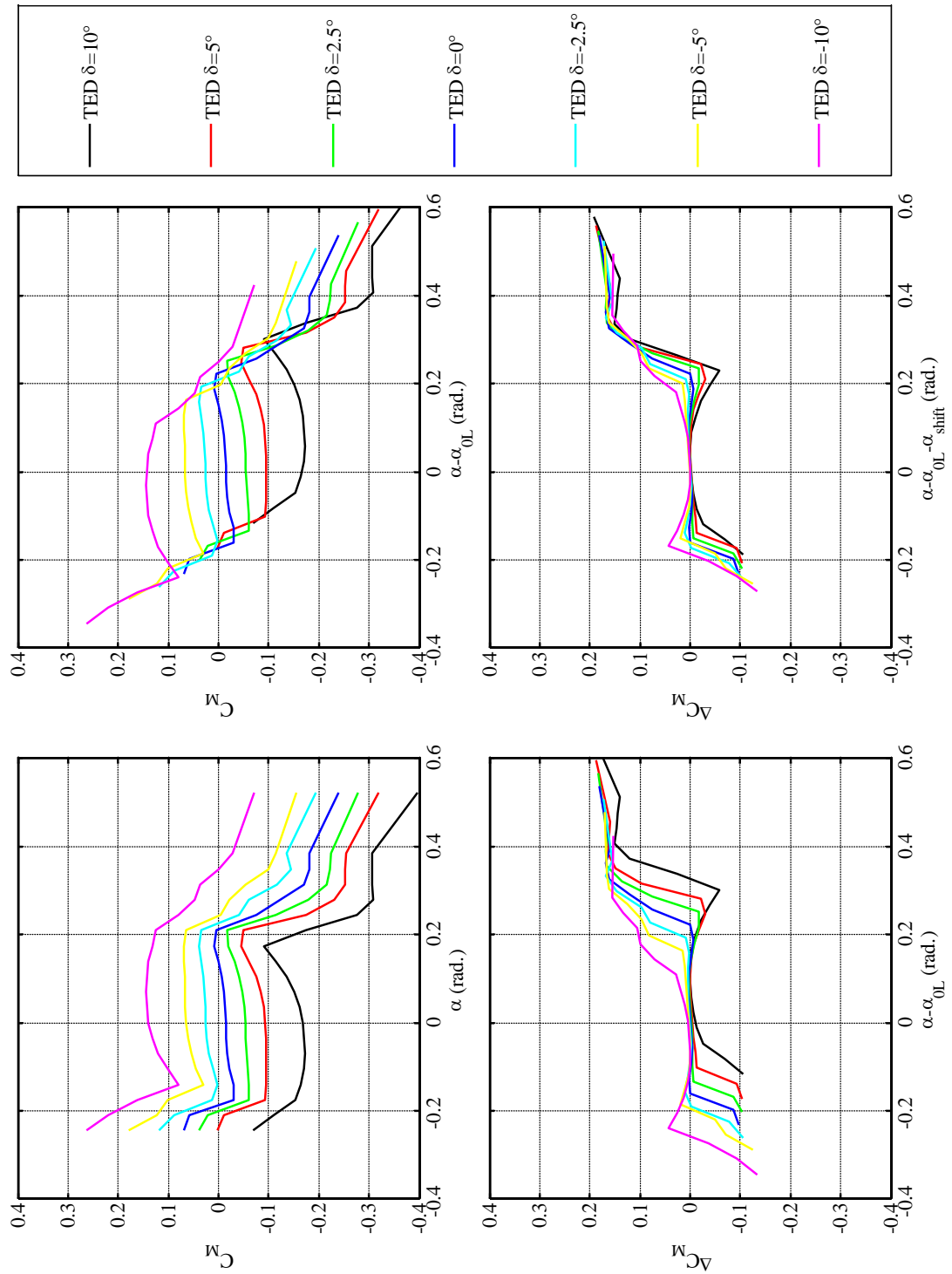


Figure 3.12: Section moment curves for SC-1095 airfoil with trailing-edge deflection.

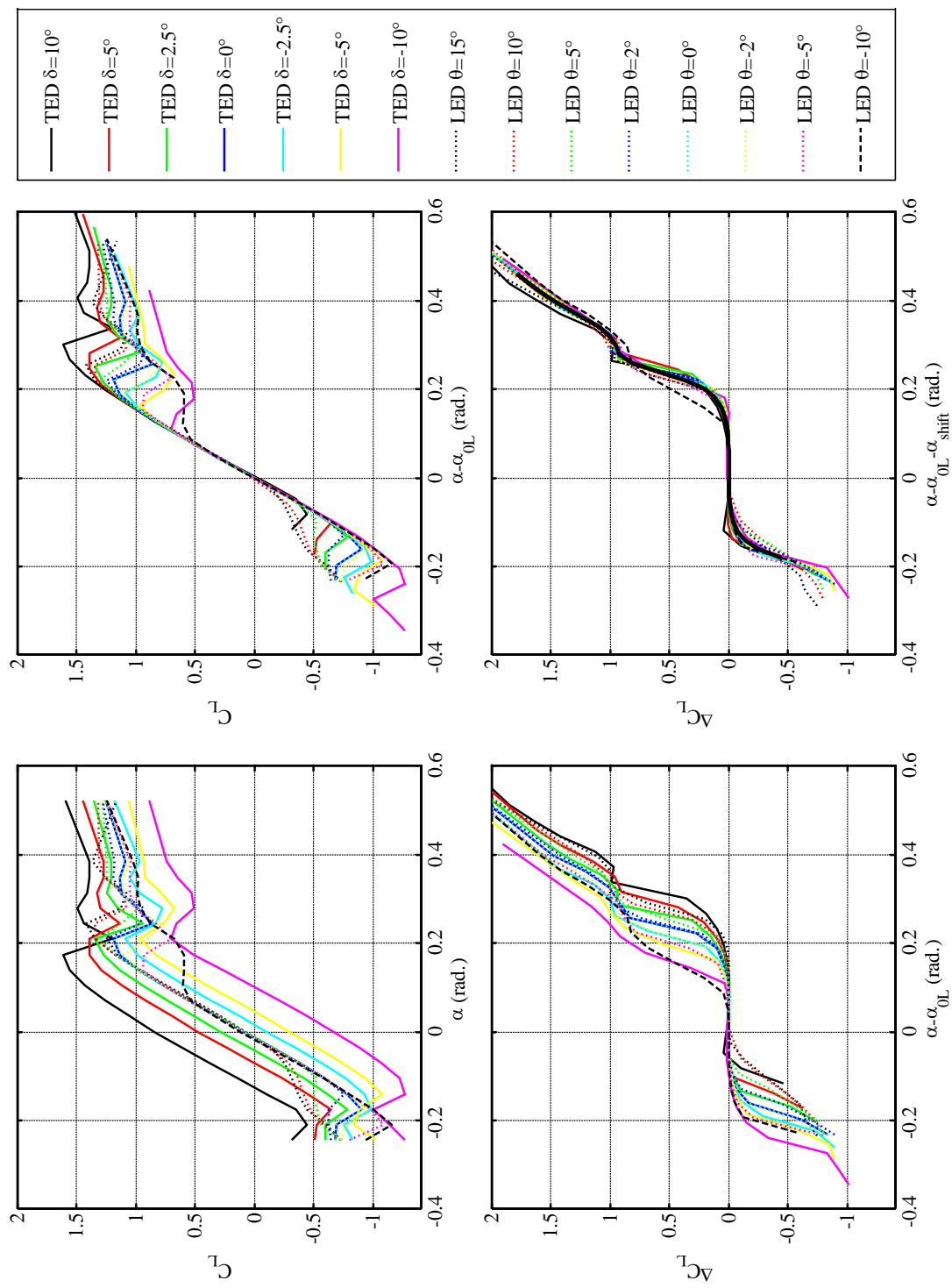


Figure 3.13: Section lift curves for SC-1095 airfoil with arbitrary morphing.

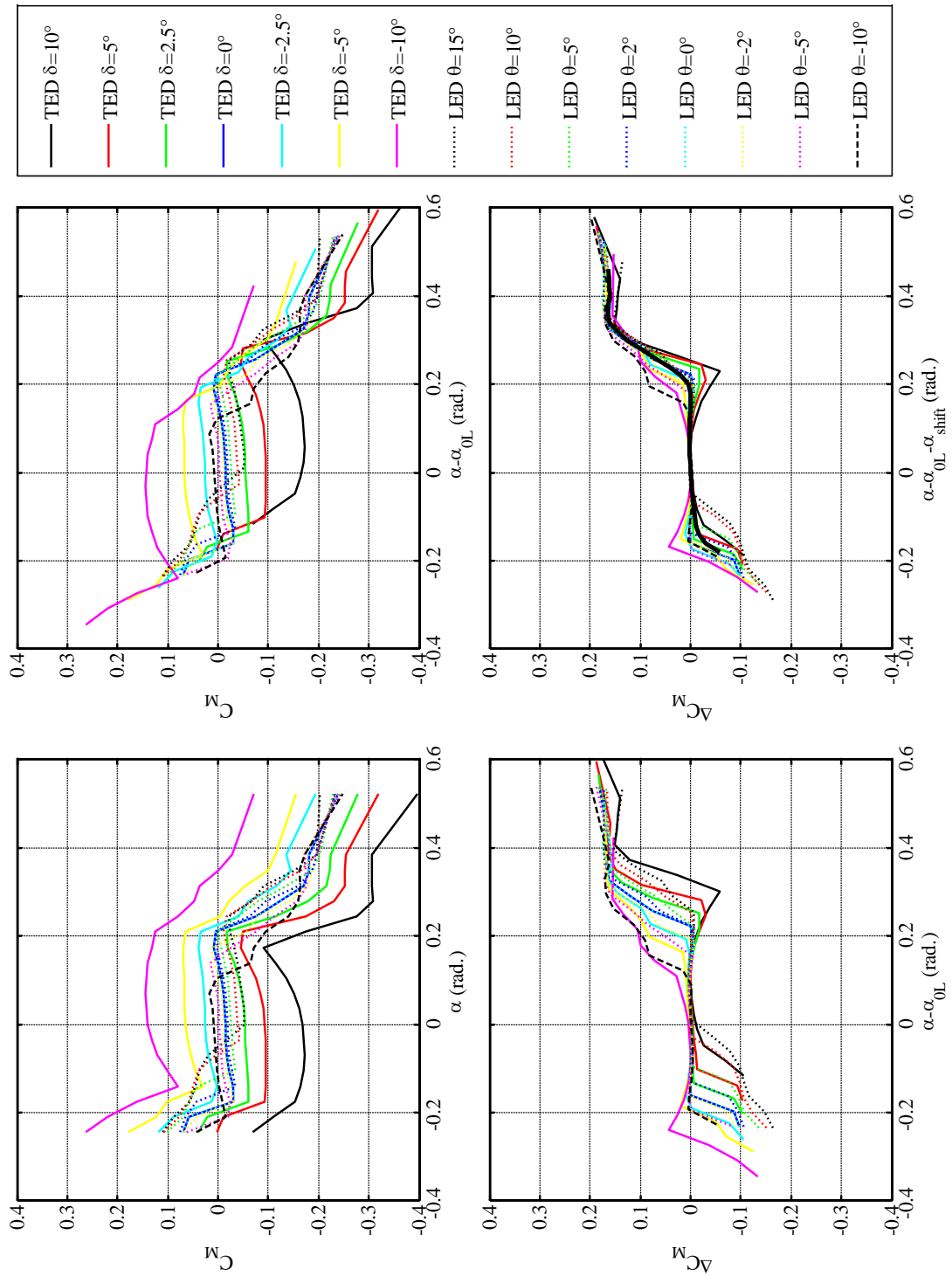


Figure 3.14: Section moment curves for SC-1095 airfoil with arbitrary morphing.

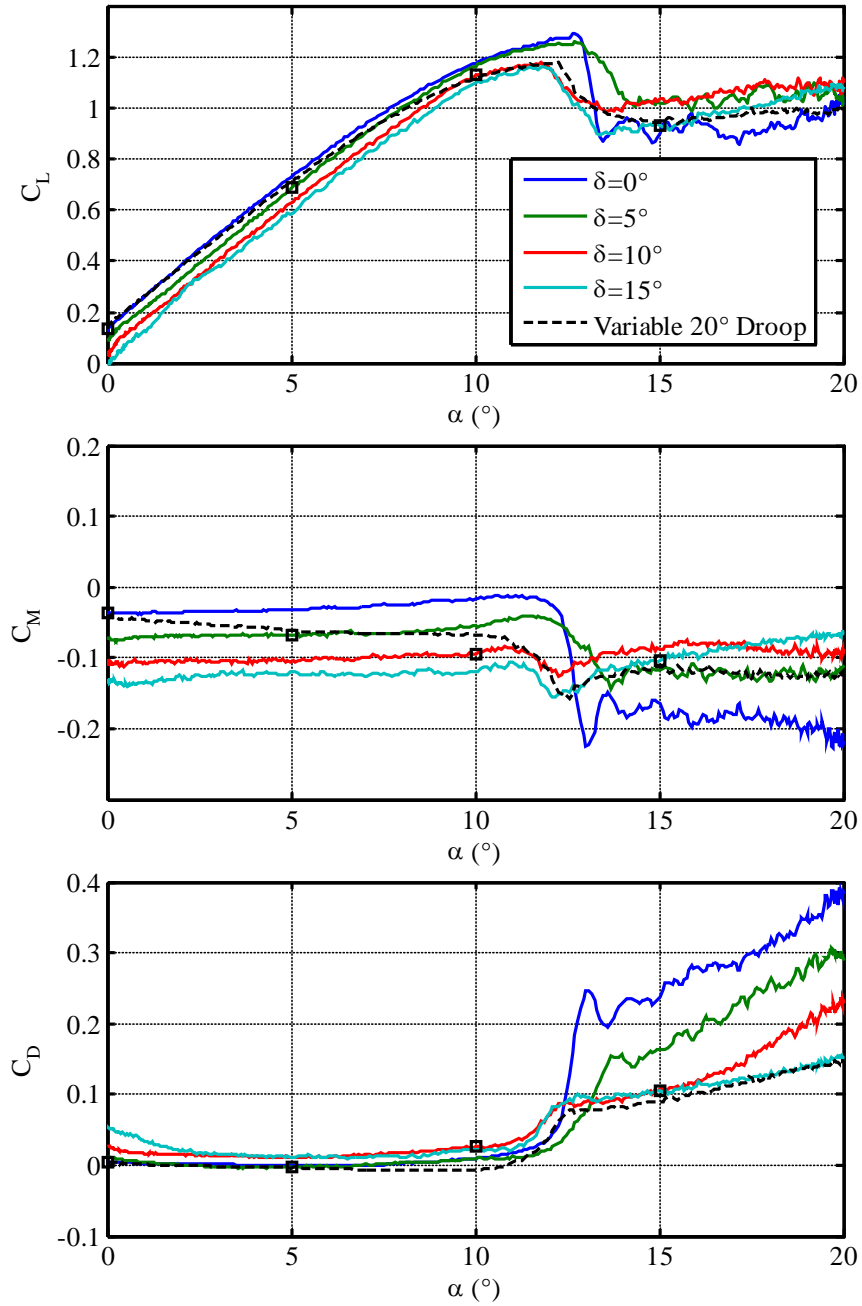


Figure 3.15: Static section characteristics for the Boeing VR-12 airfoil, $M = 0.3$.

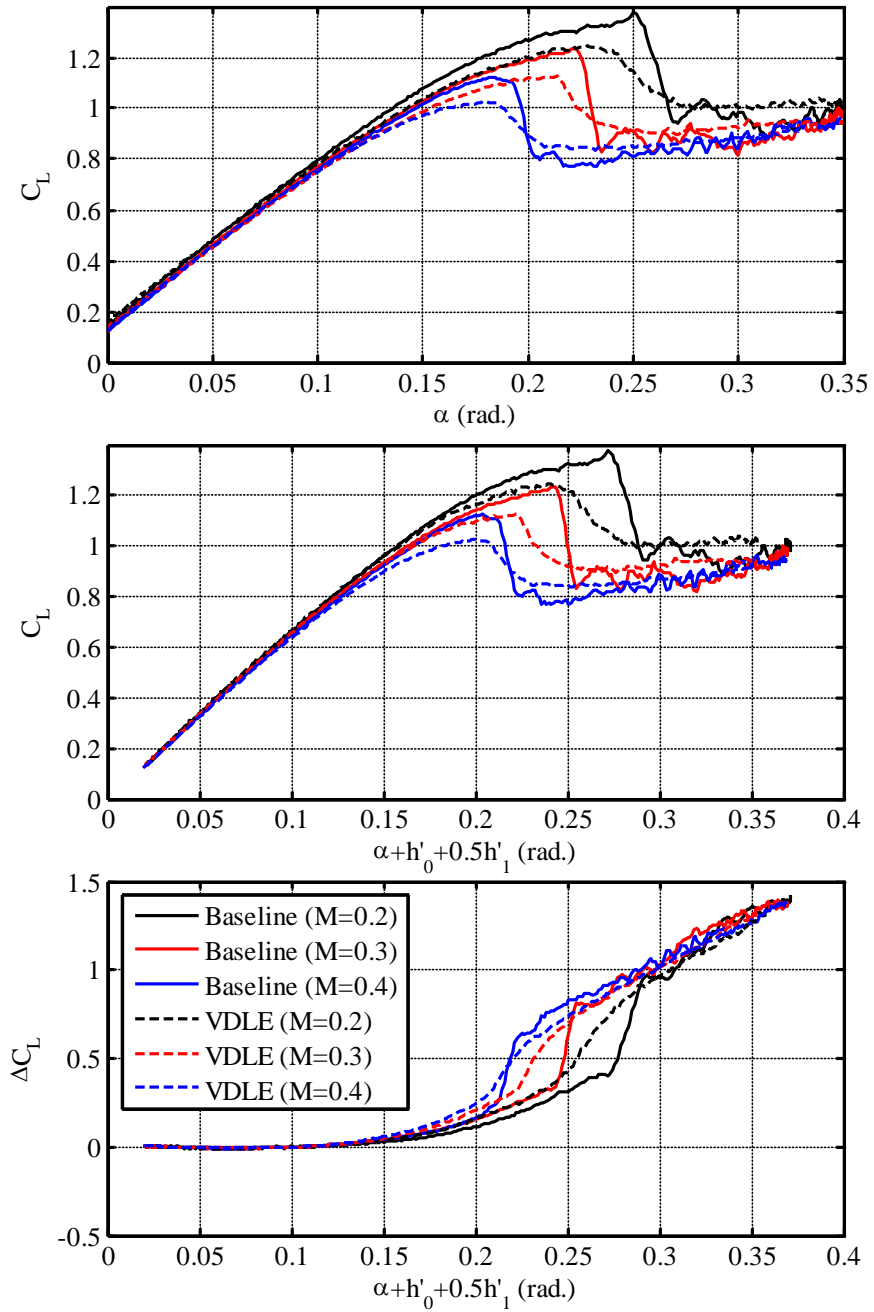


Figure 3.16: Static lift residuals for the VR-12 baseline and VDLE airfoils at $M = 0.2, 0.3, 0.4$.

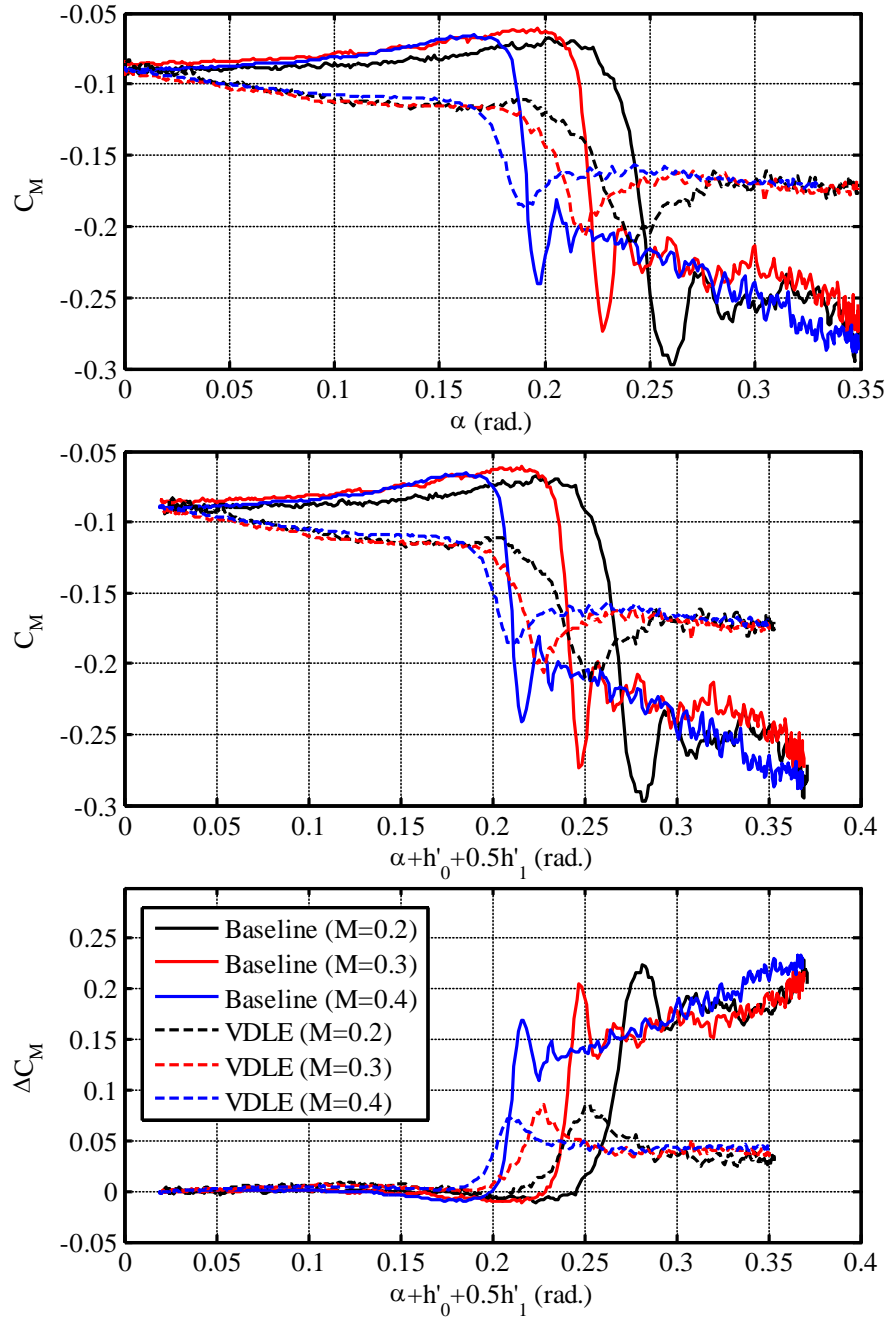


Figure 3.17: Static moment residuals for the VR-12 baseline and VDLE airfoils at $M = 0.2, 0.3, 0.4$.

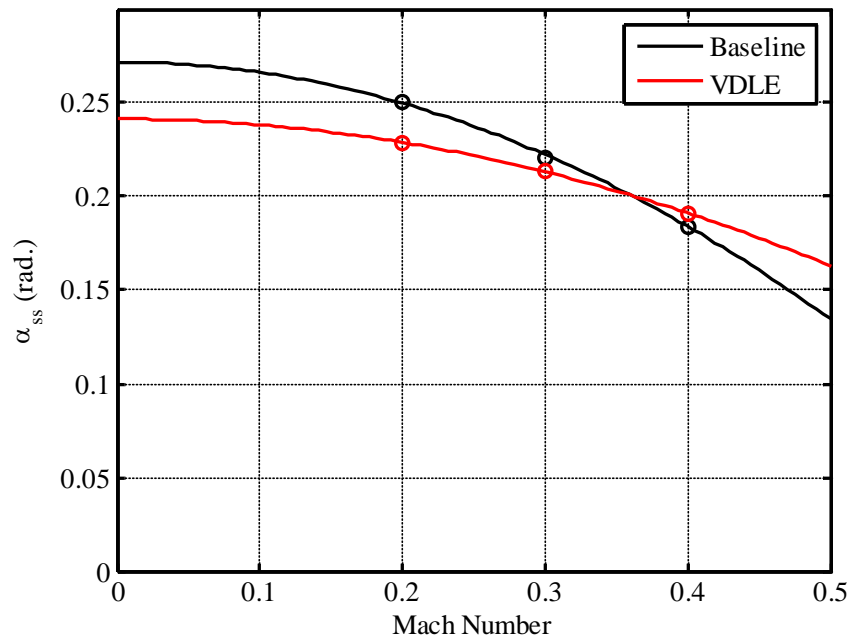


Figure 3.18: Static stall angle vs. Mach number for VR-12 airfoil.

Table 3.1: Angle of zero lift for NACA $\overline{m\overline{p}12}$ airfoils.

Airfoil	h'_0	h'_1	h'_2	Exp. α_{0L} ($^\circ$)	$-(h'_0 + 0.5h'_1)$ α_{0L} ($^\circ$)	Pred. α_{0L} ($^\circ$)	Exp. α_{ss} ($^\circ$)	Pred. α_{ss} ($^\circ$)
0012	0.0000	0.0000	0.0000	0.0	0.0	0.0	16.3	16.8
2212	-0.0176	0.0980	-0.0509	-1.8	-1.8	-1.8	15.8	15.7
2312	-0.0098	0.0866	-0.0296	-1.9	-1.9	-1.8	16.0	16.0
2412	-0.0045	0.0815	-0.0139	-1.8	-2.1	-1.9	16.4	16.2
2512	0.0000	0.0800	0.0000	-2.1	-2.3	-2.0	16.5	16.3
2612	0.0045	0.0815	0.0139	-2.3	-2.6	-2.2	16.4	16.5
4212	-0.0352	0.1960	-0.1019	-3.4	-3.6	-3.6	15.7	14.6
4312	-0.0196	0.1732	-0.0593	-3.9	-3.8	-3.6	15.7	15.1
4412	-0.0090	0.1630	-0.0277	-3.9	-4.2	-3.8	16.4	15.5
4512	0.0000	0.1600	0.0000	-4.2	-4.6	-4.0	17.0	15.9
4612	0.0090	0.1630	0.0277	-4.6	-5.2	-4.4	16.9	16.2
4712	0.0196	0.1732	0.0593	-5.0	-6.1	-5.0	17.5	16.5
6212	-0.0528	0.2940	-0.1528	-5.2	-5.4	-5.5	15.1	13.5
6312	-0.0295	0.2598	-0.0889	-5.5	-5.8	-5.4	14.6	14.3
6412	-0.0135	0.2445	-0.0416	-5.7	-6.2	-5.6	15.0	14.9
6512	0.0000	0.2400	0.0000	-6.2	-6.9	-6.0	16.4	15.4
6612	0.0135	0.2445	0.0416	-6.6	-7.8	-6.6	17.3	15.9
6712	0.0295	0.2598	0.0889	-7.0	-9.1	-7.5	17.9	16.3

Table 3.2: Tabulated values for ΔC_L and ΔC_M for morphed NACA 0012 airfoil.

$\alpha - \alpha_{0L} - \alpha_{\text{shift}}$	ΔC_L	ΔC_M
0.00	0.0000	0.0000
0.14	0.0000	0.0000
0.16	0.0006	0.0073
0.18	0.0072	0.0090
0.20	0.0174	0.0109
0.22	0.0323	0.0130
0.24	0.0560	0.0154
0.26	0.0867	0.0182
0.28	0.1476	0.0238
0.30	0.3842	0.0578
0.32	0.5977	0.0839
0.34	0.7826	0.0994
0.36	0.9653	0.1140
0.38	1.1480	0.1285

Table 3.3: Tabulated values for ΔC_L and ΔC_M for SC-1095 airfoil.

$\alpha - \alpha_{0L} - \alpha_{\text{shift}}$	ΔC_L	ΔC_M
-0.18	-0.4401	-0.0403
-0.16	-0.2527	-0.0146
-0.14	-0.1358	-0.0019
-0.12	-0.0735	0.0020
-0.10	-0.0383	0.0025
-0.08	-0.0177	0.0029
-0.06	-0.0076	0.0035
-0.04	0.0000	0.0027
0.08	0.0000	-0.0044
0.10	0.0087	-0.0066
0.12	0.0180	-0.0095
0.14	0.0364	-0.0124
0.16	0.0649	-0.0158
0.18	0.1134	-0.0168
0.20	0.2001	-0.0140
0.22	0.3634	-0.0017
0.24	0.5954	0.0217
0.26	0.8101	0.0467
0.28	0.9197	0.0713
0.30	0.9542	0.0979
0.32	1.0076	0.1181
0.34	1.0921	0.1301
0.36	1.2134	0.1322
0.38	1.3485	0.1292
0.40	1.4742	0.1256
0.42	1.5844	0.1244
0.44	1.6876	0.1246
0.46	1.7876	0.1255

Chapter 4

Determination of Stall Parameters

Due to the highly non-linear nature of dynamic stall, there is currently no physical model that adequately describes the phenomenon. Reference [30] lists various techniques that have been employed over the years to model dynamic stall. All of the models are empirical, based on wind-tunnel test data. All of these models share a dependence on the pitch rate associated with the unsteady motion. For simple harmonic motion, this implies that stall depends on the reduced frequency of oscillation (k). One model of this phenomenon is the ONERA model of Refs. [1] [2]. This model takes the form of a second-order ordinary differential equation with non-constant coefficients. The dynamic behavior of the response is governed by the choice of six model parameters. Reference [2] makes some suggestions regarding the lower and upper bounds for the parameters. The purpose of this chapter is to outline the procedure used to identify appropriate dynamic stall parameters using large-amplitude test data. The examples used to illustrate the approach are the identification of stall parameters for lift on the variable-droop Boeing VR-12 airfoil and of a morphed NACA 0012 airfoil.

Model parameters for the VR-12 are identified to give the best correlation to experimental data for lift coefficient, as published in Ref. [33]. The data were collected in the NASA Ames wind tunnel for a modified Boeing VR-12 airfoil undergoing simple harmonic motion at four different frequencies ($k = 0.025$, $k = 0.050$, $k = 0.075$, and $k = 0.100$). The problem is posed as an optimization of six design variables, with side constraints on each of the variables. The fitness function is a weighted combination of the error between the experimental data and the mathematical model at each of the four frequencies. A genetic algorithm is used to find the optimum set of parameters.

4.1 Characteristics of Dynamic Stall Response

Consider an airfoil undergoing harmonic oscillations of pitch in a free stream, as shown in Fig. 4.1. As the angle of attack increases during the upstroke, small pockets of detached flow arise, originating near the leading edge. The vortex disturbance continues to build until the boundary layer finally detaches from the airfoil. The disturbance then moves across the airfoil, resulting in a highly unsteady pressure profile. As the angle of attack is reduced during the down stroke, the flow gradually reattaches, eventually returning to its predicted value from thin-airfoil theory. The result is a hysteresis loop in the lift curve, as shown in Fig. 4.2. The solid lines indicate the portion of the curve when the angle of attack is increasing (the upstroke). The dashed lines indicate the portion of the curve when the angle of attack is decreasing (the downstroke).

Some features of the lift curve should be noted. First, for the oscillating airfoil, the onset of stall is delayed significantly compared to the static curve. However, when stall finally does occur, the drop in lift is more pronounced and persistent than it is for the static case. Second, as the frequency of oscillation increases, the amount of hysteresis increases. For low frequency oscillations (about $k = 0.025$), the lift curve has the general shape of the static curve, with a small amount of hysteresis. However at higher frequency oscillations (about $k = 0.10$), the lift barely recovers to the value predicted by theory before beginning another cycle. Thus, in order to correctly model dynamic stall for various frequencies, the model must include both a time delay and overshoot that increase with reduced frequency.

4.2 Mathematical Model

Flow over airfoils in dynamic stall is highly non-linear, which has precluded the development of a rigorous physical model of the phenomenon. The ONERA dynamic stall model is based on the observation that non-linear systems behave in an essentially linear fashion for small perturbations about a mean value. If an airfoil is placed in a wind tunnel at some mean angle of attack, then oscillated with a small amplitude of 0.5° the resulting variation in lift is well described by a second-order transfer function.

Strictly speaking, this transfer function is valid only for small perturbations about that mean angle of attack. However, if the test is repeated over a range of mean angles, one can construct a global transfer function, whose coefficients are a function of angle of attack. This is the methodology ONERA adopted to derive mathematical models for dynamic stall.

During the mid-1980's, ONERA and NASA performed small-amplitude oscillation tests on several airfoils, including the OA212, NACA 0012, and others. Reference [31] details one such study on the Vertol VR-7 airfoil at NASA. Small amplitude tests were performed at 13 different mean angles of attack and at 11 reduced frequencies. Transfer functions were found for each angle of attack, and a crude optimization was used to curve fit the parameters from the transfer functions. This work yielded several important results. First, it confirmed that the ONERA model is capable of providing reasonable correlation to experimental data; and this correlation is as good as other more complicated dynamic stall models. Second, it provided a functional form for the parameters. All of the parameters seemed to vary as ΔC_L^2 . Third, Ref. [2] suggests a reasonable range of parameter values that are used as side constraints for the optimization. It is expensive to use the small-amplitude approach to derive model parameters for every airfoil. This leads to the motivation of the present work to identify the stall parameters from large amplitude oscillation data using optimization methods.

The stall model in dimensional form is defined by Eq. (2.41), reprinted below for clarity.

$$\begin{aligned} \frac{b^2}{u_T^2} \ddot{\Gamma}_n + \hat{\eta} \frac{b}{u_T} \dot{\Gamma}_n + \hat{\omega}^2 \Gamma_n \\ = -b u_T \hat{\omega}^2 \left[\Delta C_n + \hat{e} \frac{d\Delta C_n}{dt} \frac{b}{u_T} \right] \end{aligned} \quad (4.1)$$

The parameters $\hat{\omega}$, $\hat{\eta}$, and \hat{e} are assumed to be of the functional form

$$\begin{aligned} \hat{\omega} &= \omega_0 + \omega_2 (\Delta C_L)^2 \\ \hat{\eta} &= \eta_0 + \eta_2 (\Delta C_L)^2 \\ \hat{e} &= e_0 + e_2 (\Delta C_L)^2 \end{aligned} \quad (4.2)$$

In Eq. (4.1), Γ_n is the loss in generalized circulation due to dynamic stall of the n th generalized load. For the current illustrative example, we are considering only lift. The total lift coefficient on the airfoil is given by the sum of the lift coefficient from thin-airfoil theory and the loss due to dynamic stall, given by Eq. (4.1).

$$C_L = C_{L(\text{linear})} + \frac{\Gamma_L}{u_T b} \quad (4.3)$$

where Γ_L is generally negative (but not always).

4.3 Stall Parameter Exercise for Variable-Droop VR-12

Reference [32] provides experimental data collected on a Boeing VR-12 airfoil, which was modified to have a variable-droop leading edge. In these tests, the forward 25% of the airfoil remains at zero angle of attack with respect to the free stream ($e = 0.5$), while the rear 75% of the airfoil perform pitch oscillations given by:

$$\alpha = 10^\circ + 10^\circ \sin k\tau \quad (4.4)$$

Wind tunnel data were collected at the following reduced frequencies: $k = 0.002$, 0.025 , 0.050 , 0.075 , and 0.100 . The first case, $k = 0.002$ is considered quasi-steady; that is, the frequency of oscillation is so low that it approximates the static lift curve. The static stall, ΔC_L is given by the difference between the static lift curve and the projected linear lift from thin-airfoil theory. Thus, the ONERA model, given by Eq. (4.1), utilizes the experimental values of ΔC_L with assumed motion of the form given by Eq. (4.4). The differential equation is solved numerically in *Matlab* using the *ODE45* solver. The numerical solution is compared to the experimental data for each of the four reduced frequencies from 0.025 to 0.100 . Finally, a fitness function E is calculated, which is the sum of the error norms at each of the four reduced frequencies.

To define the fitness function for the optimization, first a measure of error for each iteration is needed. The following error norm is defined for each variable g at

each of the reduced frequencies:

$$E_k = \frac{\frac{1}{N} \sum_{i=1}^N |\hat{g}(\alpha) - g(\alpha)|}{g_{max} - g_{min}} \quad (4.5)$$

where g is the experimental data of interest (in this case C_L), \hat{g} is the numerical solution, and N is the number of points at which the function is evaluated. The error norm defined by Eq. (4.5) is a measure of relative error that can be used for any airload of interest. The fitness function E is simply the sum of the error norms at each reduced frequency.

$$E = E_{0.025} + E_{0.050} + E_{0.075} + E_{0.100} \quad (4.6)$$

In Eq. (4.6), the error norms are evaluated at 0.25° intervals from 0° to 20° .

Each evaluation of the fitness function involves time-marching a differential equation to convergence (for four cases) followed by computation of the error norms. The average time to complete one evaluation is about 16 sec on a 2.60 GHz PC with 1.5 GB of RAM. In the light of the computation time required, the genetic algorithm method was selected, because it does not require gradient or Hessian evaluations. The problem is written as a formal optimization:

$$\begin{aligned} \text{Minimize } E(\omega_0, \omega_2, \eta_0, \eta_2, e_0, e_2) &= E_{0.025} + E_{0.050} + E_{0.075} + E_{0.100} & (4.7) \\ \text{subject to } 0.10 &\leq \omega_0 \leq 0.40 \\ &0.00 \leq \omega_2 \leq 0.50 \\ &0.10 \leq \eta_0 \leq 0.40 \\ &0.00 \leq \eta_2 \leq 0.60 \\ &-0.20 \leq e_0 \leq 0.20 \\ &-0.20 \leq e_2 \leq 0.00 \end{aligned}$$

The *Genetic Algorithm* toolbox in *Matlab* was used with the following parameters:

Parameter	Value
Population Type	Double
Population Size	70
Crossover Fraction	0.8
Creation Function	Uniform
Selection Function	Stochastic Uniform
Crossover Function	Heuristic
Mutation Function	Adaptive Feasible

A preliminary estimate of the dynamic stall parameters was based on a simple line search in Matlab, using the *fminunc* function. Figure 4.3 shows the fit at each of the four reduced frequencies using this initial estimate. These parameters result in a fitness function of 0.759. Figure 4.4 shows the fit at each frequency after running the genetic algorithm for thirteen generations (a total of 910 iterations). The algorithm converges to an optimal solution in about nine generations, with a final fitness function of 0.271. This is a 64% reduction in error from the initial estimate. The model captures the correct shape and character of the curves for all of the frequencies. The final parameters from the optimization are given by

$$\begin{aligned}
 \hat{\omega} &= 0.226 + 0.318(\Delta C_L)^2 \\
 \hat{\eta} &= 0.404 + 0.341(\Delta C_L)^2 \\
 \hat{e} &= 0.129 - 0.194(\Delta C_L)^2
 \end{aligned}
 \tag{4.8}$$

An indicator that the genetic algorithm is working is a rapid change in the fitness function during the first few generations, followed by a tapering off in subsequent generations as the optimum solution is approached asymptotically. Figure 4.5 shows the minimum, maximum, and average fitness function over the first thirteen generations of the genetic algorithm. As expected, there is a rapid improvement in fitness over the first five generations, followed by a more gradual linear trend from the fifth through ninth generations. By the tenth generation, the fitness function value changes by less than 0.05% per generation.

These results illustrate the procedure and demonstrate typical results that can be obtained by optimization methods. In the following sections, other results

are presented, which are obtained from a procedure similar to that described above. Depending on the context of the optimization, different objective functions can be used. In the previous example, stall parameters were optimized for a range of four different frequencies for a single load (lift). However, one may wish to identify a single set of stall parameters for both lift and pitching moment simultaneously. In that case, the objective function would include error norms for both lift and pitching moment.

4.4 NACA 0012 Stall

Although it is not commonly used in modern helicopter rotor blades, the NACA 0012 airfoil is often used as a baseline for evaluating airfoil theories. Many static and dynamic data are available for this airfoil from a variety of sources. [See Ref. [52] for a comprehensive evaluation of 0012 wind tunnel test data.] In addition, this is often the platform used for evaluation of morphing airfoil technologies. Reference [53] measures dynamic lift and pitching moments for a NACA 0012 airfoil which was modified to include a 20% chord trailing-edge flap. Thus, the proper characterization of the dynamic stall parameters for the 0012 airfoil is important in order to correlate this data.

In a report which describes the phenomenon of dynamic stall, Ref. [30] published static and dynamic lift and pitching moment results for several airfoils, including the NACA 0012. These data are used to identify stall parameters for the 0012 airfoil. The static lift residual is computed from the static data by Eq. (3.12). The lift residual is then passed through the dynamic stall filter by a numerical simulation. The optimal stall parameters are identified through a genetic algorithm optimization (as noted above). The fitness function is defined as

$$E = E_{k=0.025} + E_{k=0.100} \quad (4.9)$$

The final set of optimal stall parameters for the NACA 0012 airfoil is given by

$$\begin{aligned}
 \hat{\omega} &= 0.27 + 0.13(\Delta C_L)^2 \\
 \hat{\eta} &= 0.52 + 0.22(\Delta C_L)^2 \\
 \hat{e} &= -0.10(\Delta C_L)^2
 \end{aligned}
 \tag{4.10}$$

Figure 4.6 shows a comparison of the numerical results to the published results of Ref. [30]. This set of stall parameters is used for all of the subsequent dynamic airload correlations for the NACA 0012 morphing airfoils presented in Chapter 5.

4.5 SC-1095 Stall

In Ref. [54], static and dynamic airload data are presented for seven advanced airfoil sections typical of modern helicopters. One of the airfoils considered is the SC-1095, which is used in the UH-60 helicopter. In order to apply the stall database derived for this airfoil in Chapter 3, an estimate of the dynamic stall parameters is needed. Using the same method described above for the 0012 airfoil, the following dynamic stall parameters are determined for the SC-1095 by a genetic algorithm optimization.

$$\begin{aligned}
 \hat{\omega} &= 0.26 + 0.51(\Delta C_L)^2 \\
 \hat{\eta} &= 0.49 + 0.21(\Delta C_L)^2 \\
 \hat{e} &= 0.013(\Delta C_L)^2
 \end{aligned}
 \tag{4.11}$$

Correlations of our model with the NASA stall data for the baseline SC-1095 airfoil are shown in Fig. 4.7.

4.6 Boeing VR-12 Stall

The Boeing VR-12 airfoil is more representative of current helicopter rotor airfoils than the NACA 0012. For this reason, NASA and the US Army have studied various morphing airfoil technologies to mitigate the effect of dynamic stall on this airfoil,

Refs. [32], [33], [48]. The dynamic data of Ref. [32] are used to determine the stall parameters. As before, a genetic algorithm optimization technique is used to identify the optimal parameters.

Dynamic data for this airfoil are available for both the baseline VR-12 airfoil and the Variable Droop Leading Edge (VDLE) configuration, at Mach numbers of 0.2, 0.3, and 0.4 and reduced frequencies of $k = 0.05$ and $k = 0.10$. In order to identify representative dynamic stall parameters for correlating dynamic VR-12 data, only Mach 0.3 data are used. The objective of the optimization is to find the stall parameters that minimize the error in lift *and* pitching moment simultaneously for both airfoils and both frequencies. Thus, unlike the VR-12 discussed earlier, a total of eight correlations are used in determining the fitness of each iteration. The fitness function used in the optimization is given by

$$E = \left[E_{L, k=0.05} + E_{L, k=0.10} + E_{M, k=0.05} + E_{M, k=0.10} \right]_{\text{baseline}} + \left[E_{L, k=0.05} + E_{L, k=0.10} + E_{M, k=0.05} + E_{M, k=0.10} \right]_{\text{VDLE}} \quad (4.12)$$

Rather than using the stall parameters identified by the exercise in Section 4.3., which were optimized only for lift on the variable-droop airfoil, for this work we use data for both lift and pitching moment, for both the baseline and VDLE configurations. This is more in keeping with what a typical user would do in the future for morphing airfoils. If dynamic data are available for the baseline unmorphed geometry, the stall parameters are identified from this data and applied to morphing airfoil data. If both baseline and morphed dynamic data are available, stall parameters are identified to minimize error for both data sets simultaneously. Also, the assumption that lift and pitching moment follow the same stall dynamics ensures consistency in the model. This implies that the stall model can be applied either directly to the airloads of interest, or to the generalized Glauert loads. Furthermore, if there are any other airloads of interest, for instance flap hinge moment, these would follow the same dynamics as well.

Figure 4.8 shows the results of the optimization for the VR-12 stall parameters. The final set of optimal stall parameters is given by

$$\begin{aligned}\hat{\omega} &= 0.237 + 0.330(\Delta C_L)^2 \\ \hat{\eta} &= 0.406 + 0.206(\Delta C_L)^2 \\ \hat{e} &= -0.10(\Delta C_L)^2\end{aligned}\tag{4.13}$$

One can see from the figure that it is a quite good approximation. The parameters in Eq. (4.13) are very close to the variables found in the exercise of Eq. (4.10). This shows the robustness of the parameter identification process. This set of stall parameters is used for all of the subsequent dynamic airload correlations for the VR-12 morphing airfoils presented in Chapter 5.

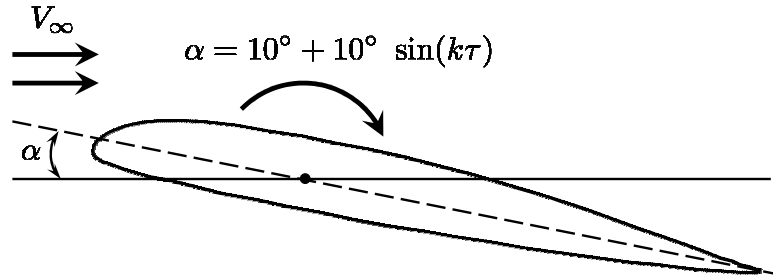


Figure 4.1: Oscillating airfoil in a free stream

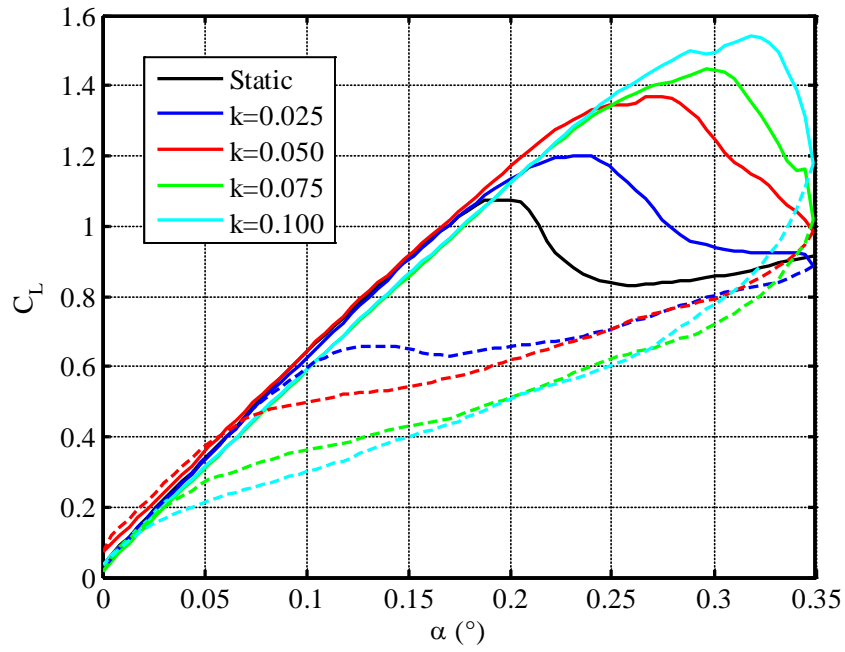


Figure 4.2: Lift coefficient for VR-12 airfoil at $k \leq 0.1$

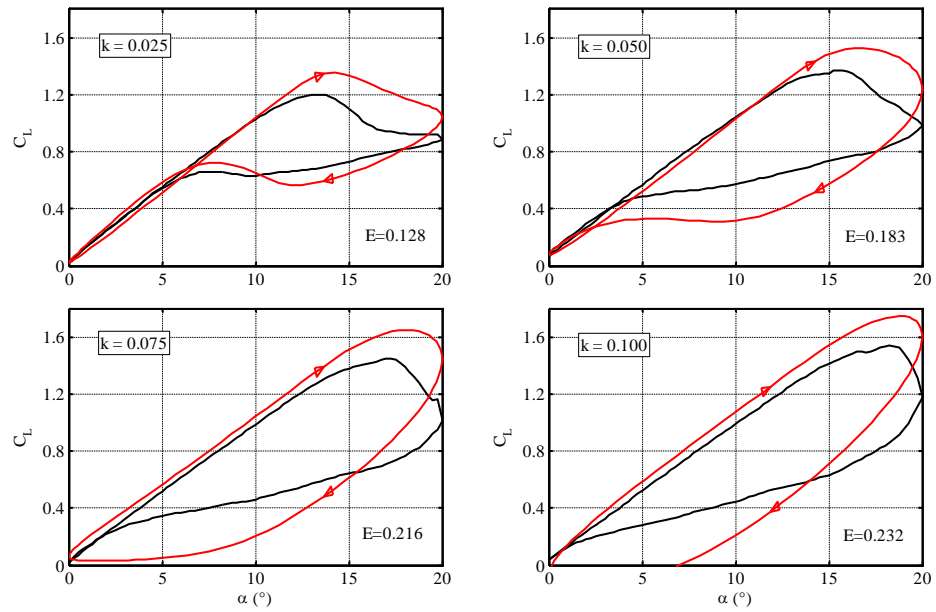


Figure 4.3: Experimental correlation with initial parameter estimates

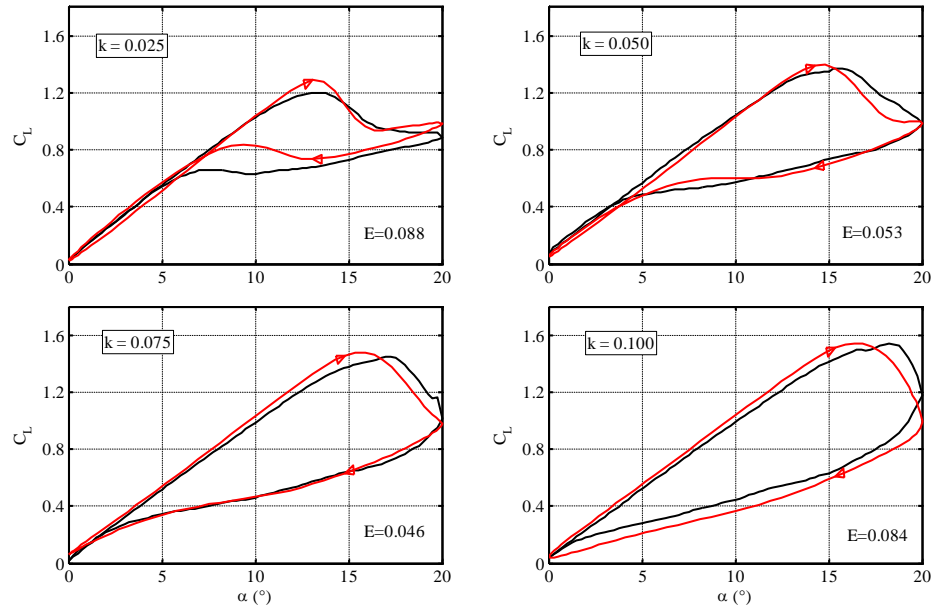


Figure 4.4: Experimental correlation with final results from genetic algorithm

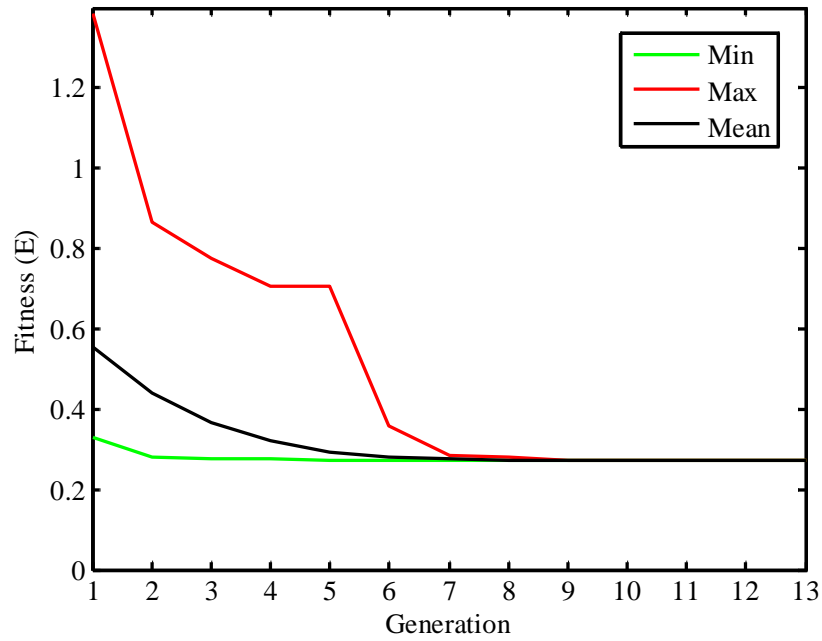


Figure 4.5: Fitness value per generation of genetic algorithm

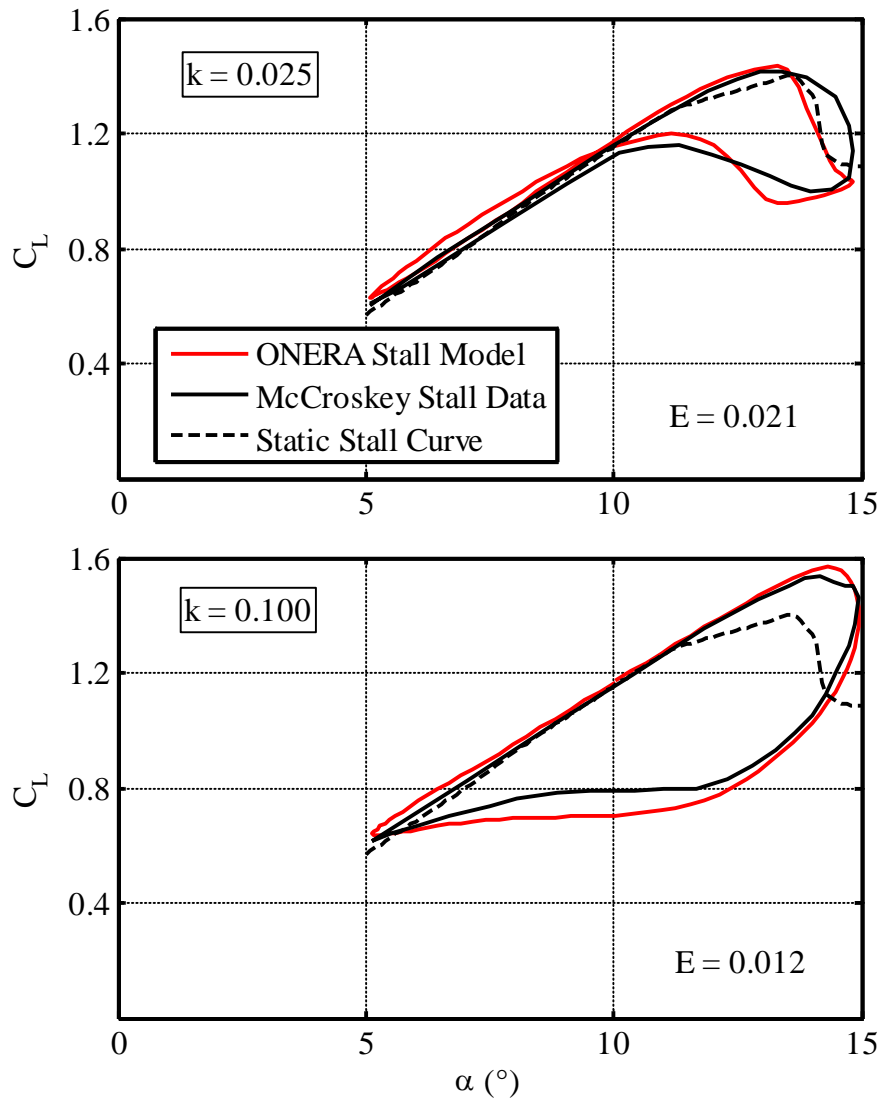


Figure 4.6: Comparison of NACA 0012 dynamic stall with Ref. [30]

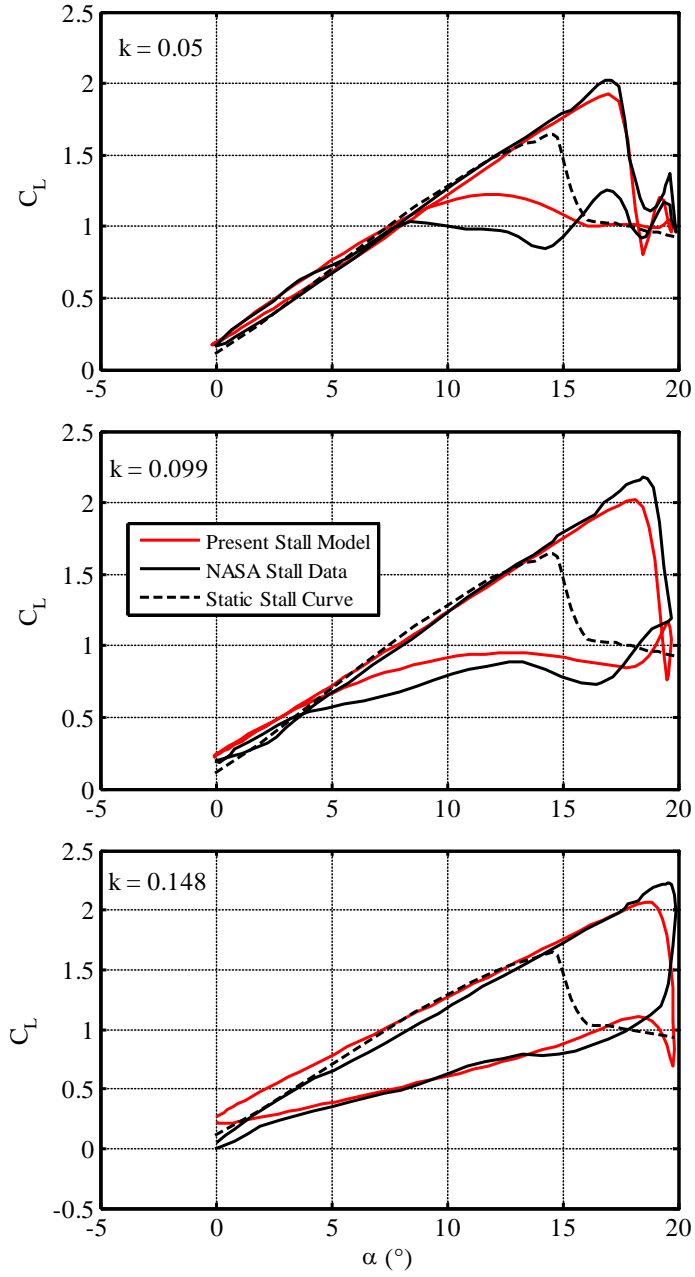


Figure 4.7: Comparison of SC1095 dynamic stall with Ref. [54]

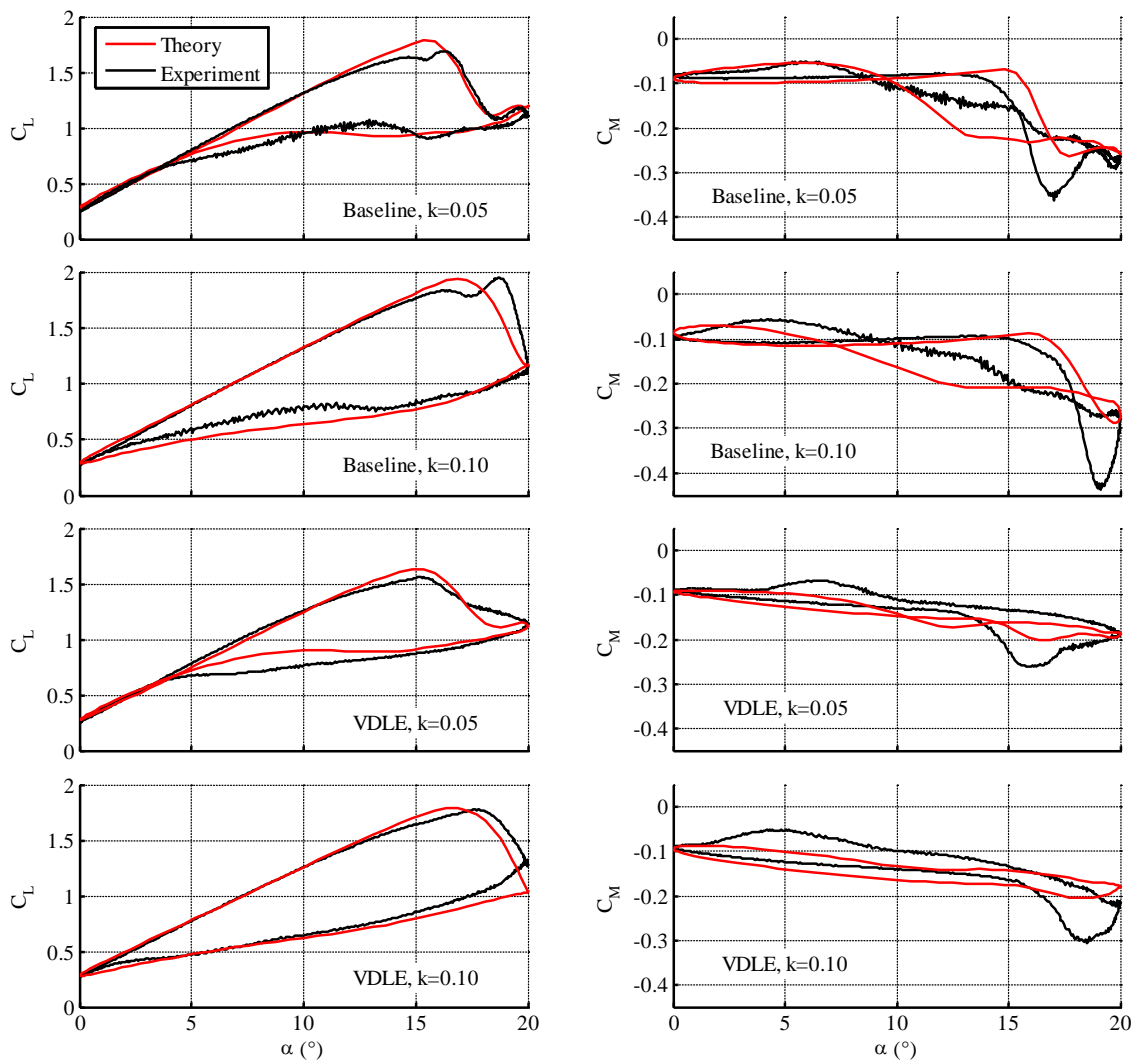


Figure 4.8: Comparison of VR-12 dynamic stall with Ref. [32]

Chapter 5

Dynamic Airload Correlations

The purpose of this chapter is to verify the accuracy of the airload theory in correlation of dynamic data. First, we demonstrate that the current theory recovers Theodorsen theory for harmonic pitch and flap motions. Then, correlations are presented for experimental data on both a NACA 0012 airfoil with trailing-edge flap deflections, and a VR-12 airfoil with leading-edge droop. Finally, we illustrate how the theory is used to predict airloads for an drooped leading-edge SC-1095 airfoil, with various deployment schedules. A list of all of the dynamic cases that have been correlated to date is given in Tab. 5.1. For the stalled cases below, one must evaluate $d(\Delta C_n)/dt$ by the chain rule. Appendix D provides a tutorial on how this can be done under the present assumptions.

5.1 Harmonic Pitch and Flap Simulations

The experimental data correlated in the following sections are 2D wind tunnel data for airfoils undergoing simple harmonic variation in pitch angle, trailing-edge flap deflection, and leading-edge droop. Therefore, it is of particular interest to show that the unified model recovers Theodorsen theory for pitch and flap deflections without dynamic stall. For simplicity, the two cases will be considered separately.

For a symmetric airfoil undergoing simple harmonic pitching motion about a point located ab aft of the mid-chord, Ref. [9] shows the lift to be

$$C_L = 2\pi \left\{ \frac{1}{2} \dot{\alpha}^* - \frac{a}{2} \ddot{\alpha}^{**} + C(k) \left[\alpha + \left(\frac{1}{2} - a \right) \dot{\alpha}^* \right] \right\} \quad (5.1)$$

where $C(k)$ is the Theodorsen lift deficiency function. For the unified model, with $h_0 = -ba\alpha$ and $h_1 = b\alpha$, the lift is given by

$$\begin{aligned} C_L &= 2\pi \left\{ \frac{h_0^*}{b} + \frac{h_1}{b} - \frac{\lambda_0}{u_0} + \frac{h_1^*}{b} + \frac{1}{2} \frac{h_0^{**}}{b} \right\} \\ &= 2\pi \left\{ -\frac{a^{**}}{2}\alpha^* - a\alpha^* + \alpha^* - \frac{\lambda_0}{u_0} + \alpha \right\} \end{aligned} \quad (5.2)$$

Balance of Eqs. (5.1) and (5.2) shows that the steady-state induced flow is given by

$$\lambda_0 = \left[\alpha + \left(\frac{1}{2} - a \right) \alpha^* \right] [1 - C(k)] \quad (5.3)$$

To validate the present methodology, the unified model equations are time marched from zero initial conditions for an input of $\alpha = 5^\circ \sin k\tau$ for reduced frequencies of $k = 0.05$ and $k = 0.1$. The left panel of Fig. 5.1 shows the induced flow in the solid line from the unified model and the Theodorsen result from Eq. (5.3) in the dotted line. After two cycles the transients in the unified model have died out and the solution has settled to the particular solution, which is indistinguishable from the Theodorsen result. The right panel of Fig. 5.1 shows the lift coefficient from the unified model after three cycles compared to the Theodorsen lift. For this case, the geometry of the airfoil is represented exactly by the two generalized deformations h_0 and h_1 , and the inflow is approximated by the finite-state induced flow theory with eight states.

The next case to consider is an airfoil fixed at zero angle of attack, undergoing simple harmonic deflections of a trailing-edge flap located db aft of the mid-chord. Reference [9] shows the lift due to a trailing-edge flap to be

$$C_L = -T_4\beta^* - T_1\beta^{**} + C(k) \left[2T_{10}\beta + T_{11}\beta^* \right] \quad (5.4)$$

where

$$\begin{aligned}
T_1 &= -\frac{1}{3}\sqrt{1-d^2}(2+d^2) + d\cos^{-1}d \\
T_4 &= -\cos^{-1}d + d\sqrt{1-d^2} \\
T_{10} &= \sqrt{1-d^2} + \cos^{-1}d \\
T_{11} &= (\cos^{-1}d)(1-2d) + \sqrt{1-d^2}(2-d)
\end{aligned}$$

For the unified model, the deflected flap geometry is represented by the Glauert expansion, $\{h\} = \{T\}\beta$, where

$$\{T\} = \begin{pmatrix} \frac{1}{\pi}[\sin\varphi_m - \varphi_m\cos\varphi_m] \\ \frac{1}{\pi}[\varphi_m - \sin\varphi_m\cos\varphi_m] \\ \frac{1}{\pi}\left[\frac{1}{n+1}\sin[(n+1)\varphi_m] + \frac{1}{n-1}\sin[(n-1)\varphi_m]\right] \\ -\frac{2}{n}\cos\varphi_m\sin(n\varphi_m) \\ \vdots \end{pmatrix}$$

The lift coefficient is given by

$$C_L = 2\pi \left\{ \left(\frac{1}{2}t_0 - \frac{1}{4}t_2 \right)^{**} \beta + (t_0 + t_1)^* \beta - \lambda_0 + \sum_{n=0}^{\infty} nt_n \beta \right\} \quad (5.5)$$

Equating Eq. (5.4) and Eq. (5.5), the induced flow becomes

$$\lambda_0 = \left(t_0 + t_1 + \frac{T_4}{2\pi} \right)^* \beta - \frac{C(k)}{2\pi} \left[2T_{10}\beta + T_{11}\beta^* \right] + \sum_{n=0}^{\infty} nt_n \beta \quad (5.6)$$

It should be noted that the β^{**} drops out of the λ_0 equation because of the cancellation of terms. Also, unlike the pitching case, the induced flow now involves an infinite sum over the generalized blade deformations. For the validation study, ten terms of the geometric expansion are used. The left panel of Fig. 5.2 shows the induced flow in the solid lines from the numerical results from time marching the unified model equations. The steady-state Theodorsen result from Eq. (5.6) is shown in the dotted line. The right panel of the figure shows the lift coefficient after three cycles compared to the

Theodorsen lift. Figures 5.1 and 5.2 show that the unified airload model recovers Theodorsen results for harmonic pitch and flap deflections.

5.2 Combined Pitch-Flap Oscillation

The first wind tunnel data to be correlated are from Ref. [53]. A NACA 0012 is oscillated in pitch about a center of rotation 35% chord from the leading edge at a reduced frequency of $k = 0.021$. At the same time, a 20% chord trailing-edge flap is oscillated at twice the pitch frequency. Lift and pitching moment coefficients are obtained by integrating pressure transducer readings along the airfoil. Eight different cases are studied, with different mean angles and different phases lag between pitch and flap motions.

The equations describing the intended motion of the airfoil are given by

$$\begin{aligned}\alpha &= \alpha_0 + \bar{\alpha} \sin(k\tau) \\ \beta &= \beta_0 + \bar{\beta} \sin(2k\tau - \phi)\end{aligned}\tag{5.7}$$

Due to inaccuracies in the mechanism that oscillates the airfoil in the wind tunnel, the actual airfoil motions were not simple harmonic. The authors of Ref. [53] provided to us the measured values of α , β , C_L , and C_M at each time step, so that the actual values of α and β could be used as the input to the unified model. The motions are transformed into the generalized coordinate system by expansion of the trailing-edge flap geometry in a Glauert series [15]. The expansion in terms of β is

$$\begin{aligned}h_0 &= \frac{\beta b}{\pi} [\sin \varphi_m - \varphi_m \cos \varphi_m] \\ h_1 &= \frac{\beta b}{\pi} [\varphi_m - \sin \varphi_m \cos \varphi_m] \\ h_n &= \frac{\beta b}{\pi} \left[\frac{1}{n+1} \sin[(n+1)\varphi_m] + \frac{1}{n-1} \sin[(n-1)\varphi_m] - \frac{2}{n} \cos \varphi_m \sin(n\varphi_m) \right]\end{aligned}\tag{5.8}$$

where $\varphi_m = \cos^{-1}(d)$, the Glauert variable at the flap hinge location. The above expansion allows for a matrix transformation between the user variables α and β and

the generalized blade deformations h_n as follows:

$$\{h_n\} = [T] \begin{Bmatrix} \alpha \\ \beta \end{Bmatrix} \quad (5.9)$$

where $[T]$ is defined in Appendix A.

The system is simulated in *Matlab* by a simultaneous solution of Eqs. (2.19), (2.28), (2.41), and (2.42) via time marching. Time derivatives are estimated with a central-difference approximation. The static airfoil data of Section 3.2 are used for the input to the dynamic stall model.

Static correction factors are determined to match the slope of the experimental static lift and pitching moment curves. Since only four of the five correction factors are linearly independent, it is convenient to assign $f_\alpha = 1$, as static data are typically given as a function of α . The experimental partial derivatives of the loads, $(\partial C_L/\partial\alpha)_{\text{exp.}}$ and $(\partial C_L/\partial\beta)_{\text{exp.}}$ are determined by the assumption that the loads are quasi-static. The data are then fit by a least squares method in *Matlab*, [i.e., the effect of induced flow is neglected]. With this approach, the best fit expression for the experimental lift and pitching moment are:

$$\begin{aligned} (C_L)_{\text{exp.}} &= 5.394\alpha + 1.944\beta - 0.04331 \\ (C_M)_{\text{exp.}} &= 0.1194\alpha - 0.4719\beta + 0.007395 \end{aligned} \quad (5.10)$$

The lift correction becomes

$$f_L = \frac{(\partial C_L/\partial\alpha)_{\text{exp.}}}{f_\alpha(\partial C_L/\partial\alpha)_{\text{theor.}}} = \frac{5.394}{2\pi} = 0.8584 \quad (5.11)$$

Similarly, the flap effectiveness correction factor is given by

$$f_\beta = \frac{(\partial C_L/\partial\beta)_{\text{exp.}}}{f_L(\partial C_L/\partial\beta)_{\text{theor.}}} = \frac{1.944}{0.8584(3.486)} = 0.6497 \quad (5.12)$$

The pitching moment about the center of rotation is comprised of two components: the moment about the mid-chord and the moment generated by the lift offset from the center of rotation, as shown in Fig. 2.6. The corrected location of the center of rotation $a_{\text{corr.}}$ adjusts the effect of lift in the overall pitching moment; that is, it

controls the slope of the pitching moment curve. The pitching moment correction factor f_M must satisfy two equations simultaneously.

$$f_M = \frac{(\partial C_M / \partial \alpha)_{\text{exp.}}}{f_\alpha (\partial C_M / \partial \alpha)_{\text{theor.}}} = \frac{(\partial C_M / \partial \beta)_{\text{exp.}}}{f_\beta (\partial C_M / \partial \beta)_{\text{theor.}}} \quad (5.13)$$

From the definition of the force coefficients,

$$(C_M)_{\text{theor.}} = \frac{1}{2\rho u_0^2 b} (L_1 - a_{\text{corr.}} b L_0) \quad (5.14)$$

Differentiation gives:

$$\left(\frac{\partial C_M}{\partial \alpha} \right)_{\text{theor.}} = \frac{1}{2\rho u_0^2 b} \left(\frac{\partial L_1}{\partial \alpha} - a_{\text{corr.}} b \frac{\partial L_0}{\partial \alpha} \right) \quad (5.15)$$

$$\left(\frac{\partial C_M}{\partial \beta} \right)_{\text{theor.}} = \frac{1}{2\rho u_0^2 b} \left(\frac{\partial L_1}{\partial \beta} - a_{\text{corr.}} b \frac{\partial L_0}{\partial \beta} \right) \quad (5.16)$$

Equations (5.13), (5.15), and (5.16) can be combined and simplified, giving closed form expressions for $a_{\text{corr.}}$ and f_M . The final set of correction factors used for all of the cases in the correlation is:

$$\begin{aligned} f_\alpha &= 1 & f_\beta &= 0.6497 \\ f_L &= 0.8584 & f_M &= 1.2352 \\ a_{\text{corr.}} &= -0.4692 & [a_{\text{uncorr.}} &= -0.4000] \end{aligned} \quad (5.17)$$

Figures 5.3-5.10 show correlations for eight different dynamic cases at a nominal reduced frequency of $k = 0.02$. (Since the motion is not purely harmonic, there is not an exact reduced frequency.) In each figure, the top panel shows the flap deflection β as a function of α . The middle and bottom panels show the dynamic lift and pitching moment behavior, respectively. The error norm defined in Eq. (4.5) is inset on each figure. In Figs. 5.3-5.5, the angle of attack varies between -6° and $+6^\circ$, with various phase lags from 59° to 239° . In this range, the airload behavior is linear. Therefore, the stall residuals ΔC_L and ΔC_M are zero, and there is no loss in circulation due to dynamic stall. The correlation between theory and experiment is excellent for all of these cases (less than 5% error), serving to validate the static correction factors derived above.

In Figs. 5.6-5.8, the angle of attack varies between -2° and 10° , where the effect of dynamic stall is moderate. Phase angles (between α and β) of 148° , 206° and 298° are considered. The correlation between theory and experiment is still quite good, with less than 6% error norm E for all cases.

For the final two cases considered, shown in Figs. 5.9-5.10, the angle of attack varies between 5° and 15° , where the effect of dynamic stall is quite large. Phase angles of 177° and 343° are shown. In these figures, the blue dashed line indicates what the airloads would be if no dynamic stall losses were included. The red line shows the results of the unified model, including dynamic stall. The model provides reasonable correlation to the experimental data for both lift and pitching moment, $E < 0.09$. From these correlations, we conclude the model captures the essential physics of the dynamic stall phenomenon.

It should be emphasized that, in Figs. 5.3-5.10, a single set of four linearly independent correction factors correlate steady, 1/rev, and 2/rev components of lift and pitching moment for eight different mean angle and phase lag combinations. This is a total of $2 \times 3 \times 8 = 48$ different components correlated. Not only does a single set of correction factors apply to all data for this airfoil, but a single set of five dynamic stall parameters applies to either lift or pitching moment. Although the theory allows distinct parameters for each generalized load, practice has shown that a unified set is adequate. However, one always has the option of separate parameters, as suggested by Ref. [1].

5.3 VR-12 Variable Droop

The experimental setup of Refs. [32] and [33] is shown in Fig. 5.11. A VR-12 airfoil is placed in a horizontal wind tunnel and undergoes oscillation in pitch angle, α , about the quarter chord. The airfoil is modified with a hinge at the quarter chord to allow for variable droop of the leading edge ($e = 0.5$). Wind tunnel tests with oscillating angle of attack are given for two different configurations. In the baseline configuration, the nose droop angle is fixed at 0° , and the entire airfoil oscillates in

pitch, where the angle of attack is given by

$$\alpha = 10^\circ + 10^\circ \sin(k\tau) \quad (5.18)$$

In the VDLE configuration, the leading 25% of the airfoil is fixed at zero incidence to the oncoming flow, while the remainder of the airfoil undergoes pitch oscillations. Thus, the nose droop angle is equal to the pitch angle at all times. Note that in this configuration, the angle of attack is referenced with respect to the trailing 75% of the airfoil. Since static stall data are available for each of the configurations (Chapter 3), there is no need to parameterize them versus δ or α . Those static curves can be put directly through the stall filter.

The motions are transformed into the generalized coordinate system by expansion of the leading-edge flap geometry in a Glauert series [15]. The expansion in terms of δ is

$$\begin{aligned} h_0 &= \frac{\delta b}{\pi} [\sin \varphi_m - \varphi_m \cos \varphi_m] \\ h_1 &= \frac{\delta b}{\pi} [\varphi_m - \sin \varphi_m \cos \varphi_m] \\ h_n &= \frac{\delta b}{\pi} \left[\frac{1}{n+1} \sin[(n+1)\varphi_m] + \frac{1}{n-1} \sin[(n-1)\varphi_m] - \frac{2}{n} \cos \varphi_m \sin(n\varphi_m) \right] \end{aligned} \quad (5.19)$$

where $\varphi_m = \cos^{-1}(-e)$, the Glauert variable at the leading-edge flap hinge location. The above expansion allows for a matrix transformation between the user variables α and δ and the generalized blade deformations h_n as follows:

$$\{h_n\} = [T] \begin{Bmatrix} \alpha \\ \delta \end{Bmatrix} \quad (5.20)$$

where $[T]$ is defined in Appendix A.

Before correlating the dynamic data, the static correction factors must be determined. The static data are given as a function of α , so it is convenient to assign $f_\alpha = 1$. The slope of the linear portion of the lift curve for the baseline VR-12 airfoil is determined to be $\partial C_L / \partial \alpha = 6.8738$. Thus, the lift correction factor is given by

$$f_L = \frac{6.8738}{2\pi} = 1.0940 \quad (5.21)$$

The slope of the linear portion of the lift curve for the VDLE airfoil is 6.4767. The change in slope from the baseline airfoil is due entirely to the effect of the nose droop. Thus,

$$\frac{\partial C_L}{\partial \delta} = \left[\frac{\partial C_L}{\partial \alpha} \right]_{\text{VDLE}} - \left[\frac{\partial C_L}{\partial \alpha} \right]_{\text{baseline}} = -0.3791 \quad (5.22)$$

The nose droop effectiveness is given by

$$f_\delta = \frac{(\partial C_L / \partial \delta)_{\text{exp.}}}{f_L (\partial C_L / \partial \delta)_{\text{theor.}}} = 0.9565 \quad (5.23)$$

The remaining correction factors are determined from the moment data. The slope of the moment curve for the baseline airfoil is $\partial C_M / \partial \alpha = 0.0607$. The slope for the VDLE airfoil is $\partial C_M / \partial \alpha = -0.2123$. Thus, $\partial C_M / \partial \delta = -0.2730$. The moment correction factor must satisfy two equations simultaneously.

$$f_M = \frac{0.0607}{f_\alpha (\pi/2)(1 + 2a)} = \frac{0.2730}{f_\delta (0.6142 + 0.3623a)} \quad (5.24)$$

The final set of correction factors used for all of the cases in the correlation is:

$$\begin{aligned} f_\alpha &= 1 & f_\delta &= 0.9565 \\ f_L &= 1.0940 & f_M &= 1.3020 \\ a_{\text{corr.}} &= -0.4852 & [a_{\text{uncorr.}} &= -0.5000] \end{aligned} \quad (5.25)$$

These were determined at $M = 0.3$. Due to a small variation in Mach number for the cases considered, the affect of Mach number on these static corrections is negligible, and the same correction factors were used for all cases.

Figures 5.12-5.23 show correlations between the experimental results of Ref. [32] and the unified airloads model, as described above. Figures 5.12 through 5.17 show results for pitch oscillations at a reduced frequency of $k = 0.05$ and Mach numbers ranging from $M = 0.2$ to $M = 0.4$ for both the baseline VR-12 airoil and the VDLE airfoil. The model is consistent with the experimental data in the following ways:

1. The maximum lift coefficient is reduced in the VDLE airoil, because the effective angle of attack at the leading 25% of the airfoil is effectively reduced.

2. The extent of the hysteresis in the lift curve is well represented by the dynamic model.
3. The “negative damping” region of the pitching moment curve is significantly reduced in the VDLE airfoil, which is consistent with experimental observations.

In Ref. [33], it is noted that the lift coefficient has a double peak near its maximum for the baseline VR-12 case. As the stall vortex convects along the airfoil, the suction peak decreases rapidly at first, followed by a more gradual decrease as the airfoil approaches the maximum incidence. It is not possible to capture this level of detail with the simplified model. However, by minimizing the least-squares error with a genetic algorithm, the optimization procedure naturally splits the difference between the two distinct peaks, providing very good correlations.

Figures 5.18 and 5.23 show results for pitch oscillations at a reduced frequency of $k = 0.1$ and Mach numbers ranging from $M = 0.2$ to $M = 0.4$ for both the baseline VR-12 and VDLE airfoils. Again, the model agrees favorably with the experimental results in terms of the maximum C_L and the width of the hysteresis. In addition, for the VDLE airfoil, the negative damping region in the pitching moment curve is gone completely, which is consistent with the experimental data.

In Ref. [55], a comparison is made to the CFD data of Ref. [56] for the baseline and VDLE configurations at $M = 0.3$ and $k = 0.1$. In that work, the CFD model must be corrected for wall effects, since there is a constant offset in the data, as well as a discrepancy in the slope of the lift curve. This illustrates one of the benefits of the current theory. Static corrections to the theory to correlate experimental test results, are made in a very straightforward manner. The resulting correlations for lift, pitching moment, and drag, are qualitatively accurate and implicitly include wall corrections. Then, to apply to a test section not in a wind tunnel, the wall corrections can be analytically removed from the static corrections. The level of accuracy is in keeping with the purpose of the theory: a simplified aerodynamic tool for flight and simulation and preliminary design.

5.4 SC-1095 with LE Droop

In this section we demonstrate how the unified theory is applied to the SC-1095 airfoil with leading-edge droop. Reference [50] uses a comprehensive code to investigate various dynamic morphing concepts under various flight conditions for a UH-60 helicopter. In the high-thrust forward flight condition (C9017), dynamic stall has a significant impact on overall rotor performance. For this flight condition, the authors investigate harmonically deployed leading-edge droop to mitigate stall. Rotor performance, indicated by percent change in the effective rotor L/D compared to the baseline, is shown with 0/rev, 1/rev, 2/rev, 3/rev, and 4/rev deflections for various phase angles in Fig. 25 of Ref. [50]. This figure is reprinted as Fig. 5.24 for comparison.

To illustrate the application of the present theory, we investigate dynamic droop deployment for a two-dimensional airfoil to mitigate dynamic stall. [It should be noted that the induced flow for the current study is for a 2D flat wake, whereas the study in Ref. [50] is for a 3D wake.] The unified airloads model is used to compute dynamic lift for airfoil motions of the following form:

$$\begin{aligned}\alpha &= 10^\circ + 10^\circ \sin k\tau \\ \theta_{LE} &= \theta_0 \sin(nk\tau + \phi)\end{aligned}\tag{5.26}$$

where θ_0 is the amplitude of the leading-edge droop input, ϕ is the phase angle, and n is the number of times per revolution the deflection is deployed. A reduced frequency of $k = 0.05$ is used. Drag is assumed to be quasi-steady. Figure 5.25 shows the airfoil performance—indicated by the percent change in maximum L/D from the baseline airfoil—for various deflections. From the static CFD results shown in Fig. 3.9, a correction factor of $f_\alpha = 1.044$ is applied to α to correct the slope of the lift curve. All other static correction factors are assumed to be 1. Although these data are for 2D dynamic stall, the trends are similar to the 3D results from Ref. [50]. The two conditions that provide the most performance improvement are a 2° 1/rev droop with a phase angle of 120° and a 3° 2/rev droop with a phase angle of 60° . Figures 5.26-5.28 compare the baseline airfoil to the two alternative dynamically drooped airfoils. It can be seen that, while the 1/rev droop increases maximum lift (and hence maximum L/D), it actually increases the hysteresis in the lift curve. Thus, it is not effective in

mitigating dynamic stall. The 2/rev droop did not significantly increase maximum lift, but it did reduce the hysteresis. We conclude that a 2/rev dynamic droop can be utilized to mitigate the effect of 2D dynamic stall.

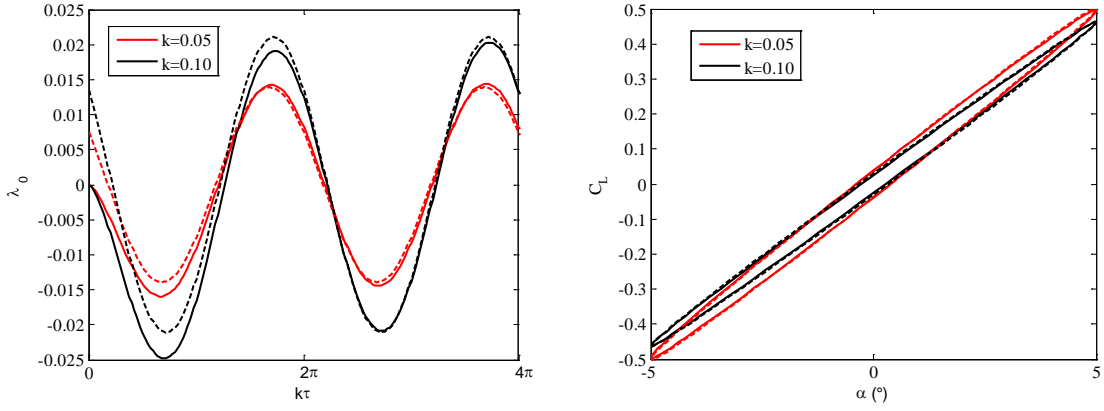


Figure 5.1: Comparison with Theodorsen theory for harmonic pitch oscillations.

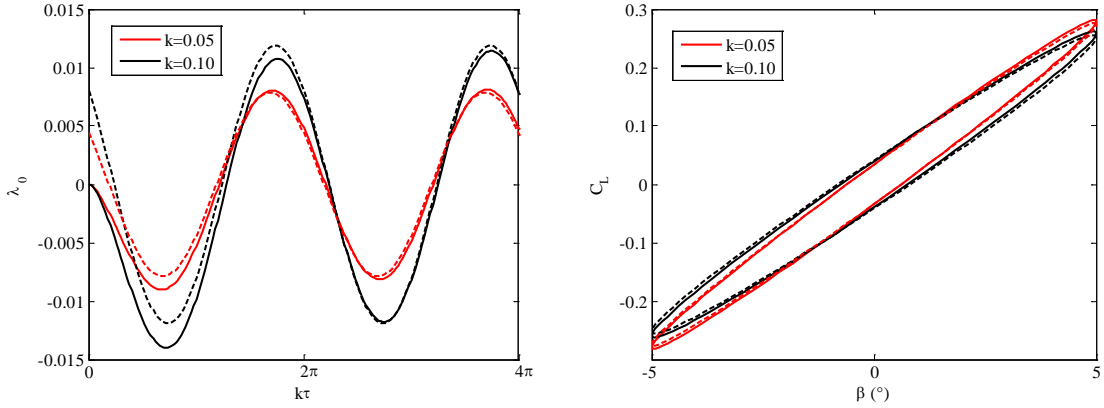


Figure 5.2: Comparison with Theodorsen theory for harmonic flap oscillations.

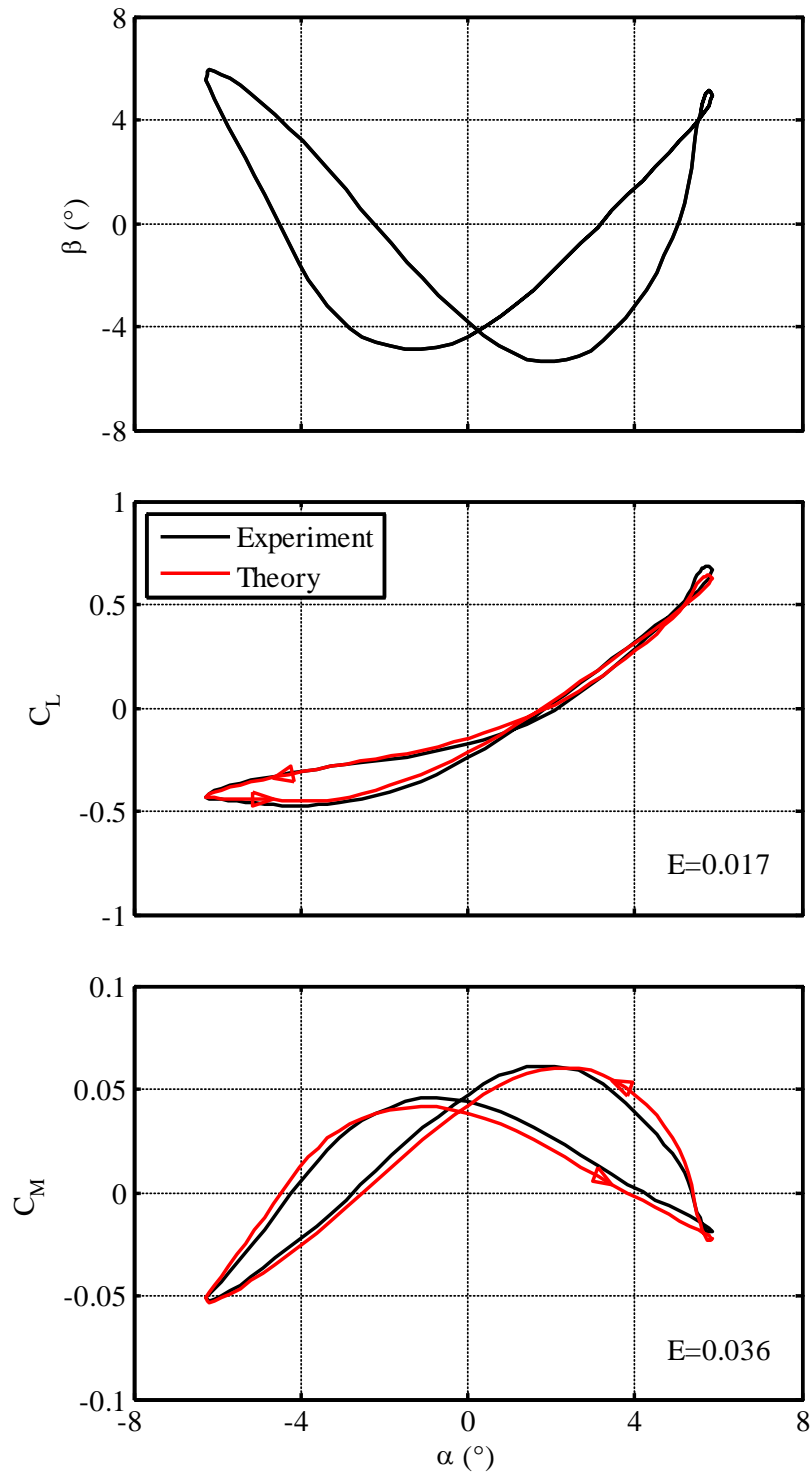


Figure 5.3: NACA 0012 airfoil with TE flap, no dynamic stall, $\phi = 59^\circ$.

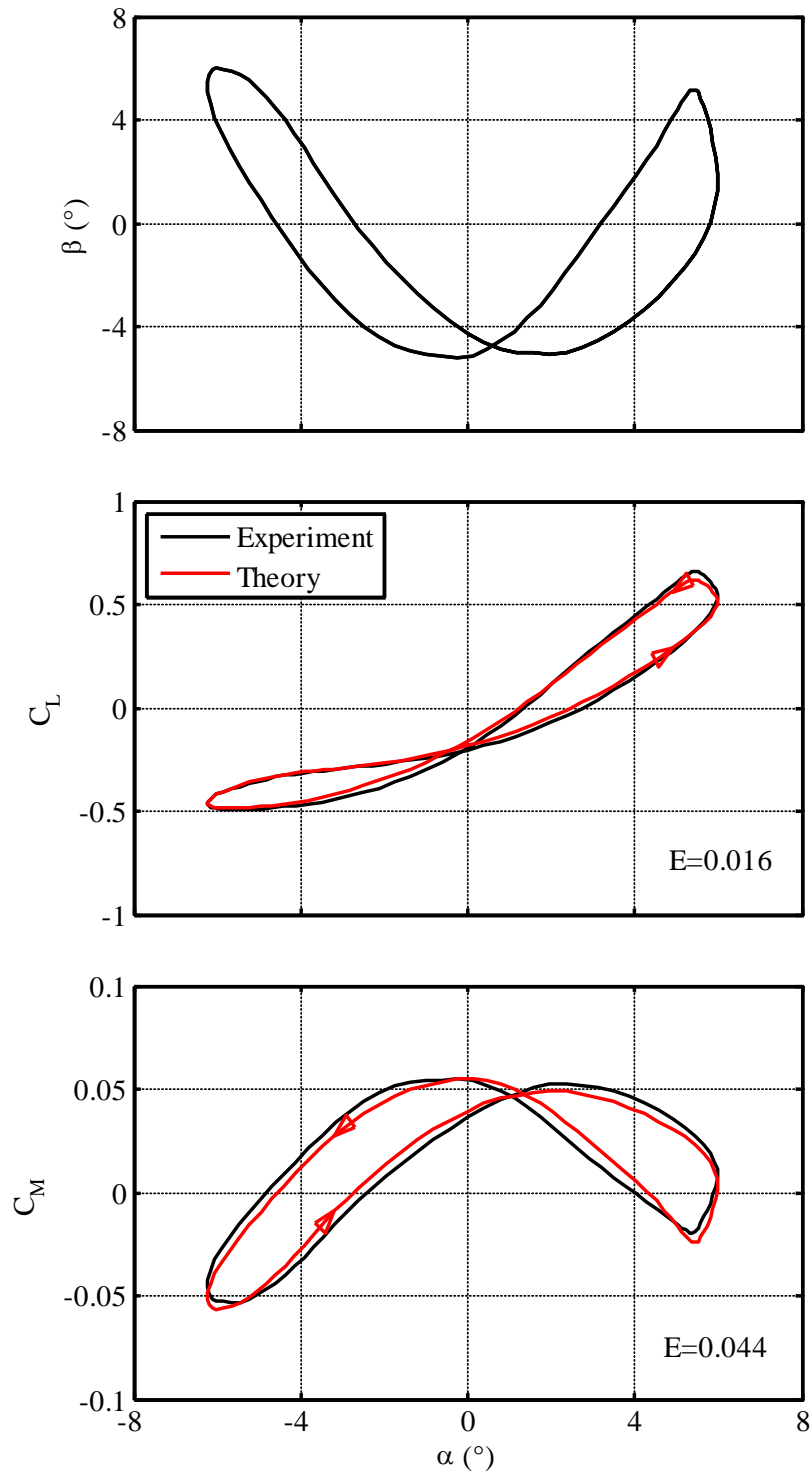


Figure 5.4: NACA 0012 airfoil with TE flap, no dynamic stall, $\phi = 122^\circ$.

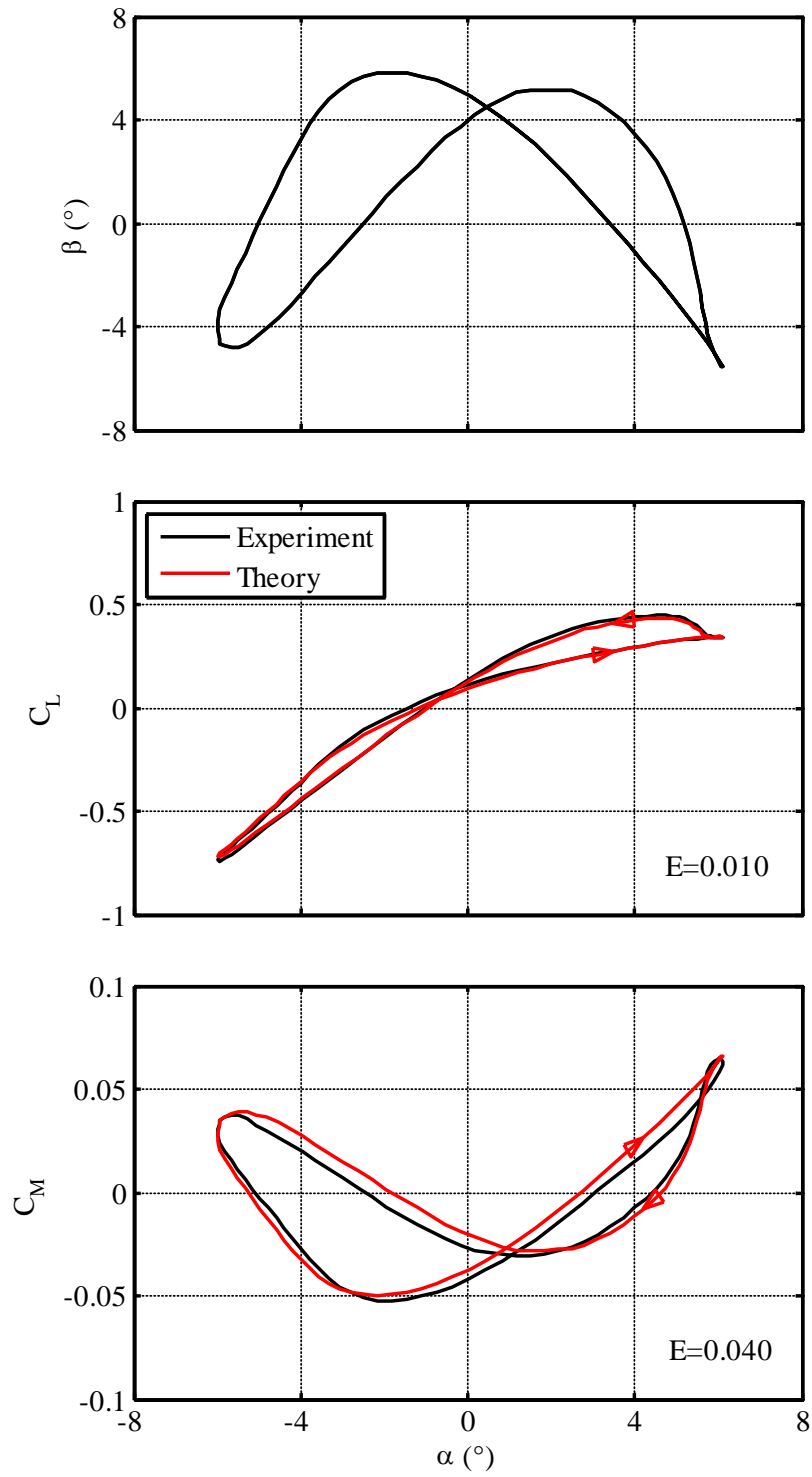


Figure 5.5: NACA 0012 airfoil with TE flap, no dynamic stall, $\phi = 239^\circ$.

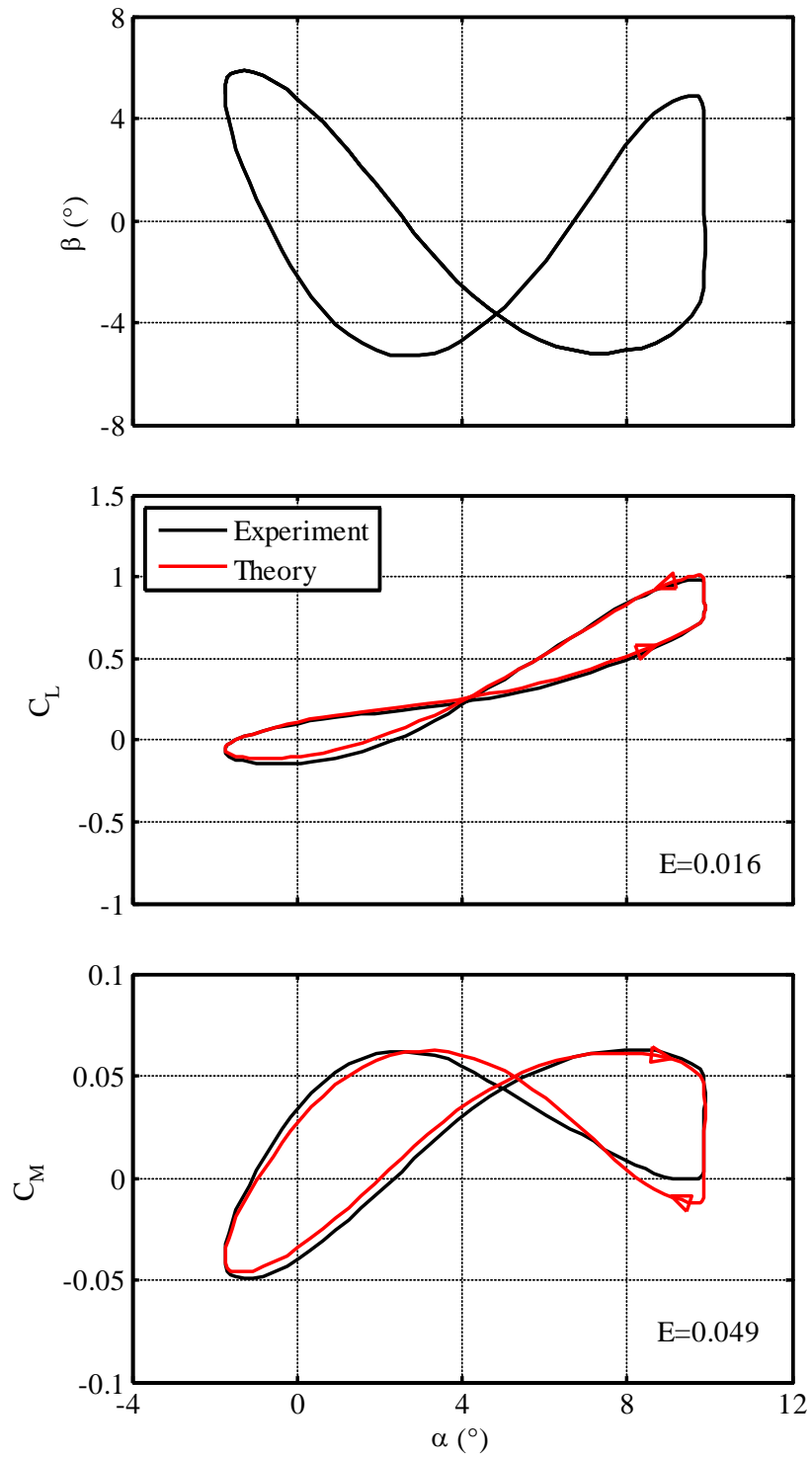


Figure 5.6: NACA 0012 airfoil with TE flap, moderate stall, $\phi = 148^\circ$.

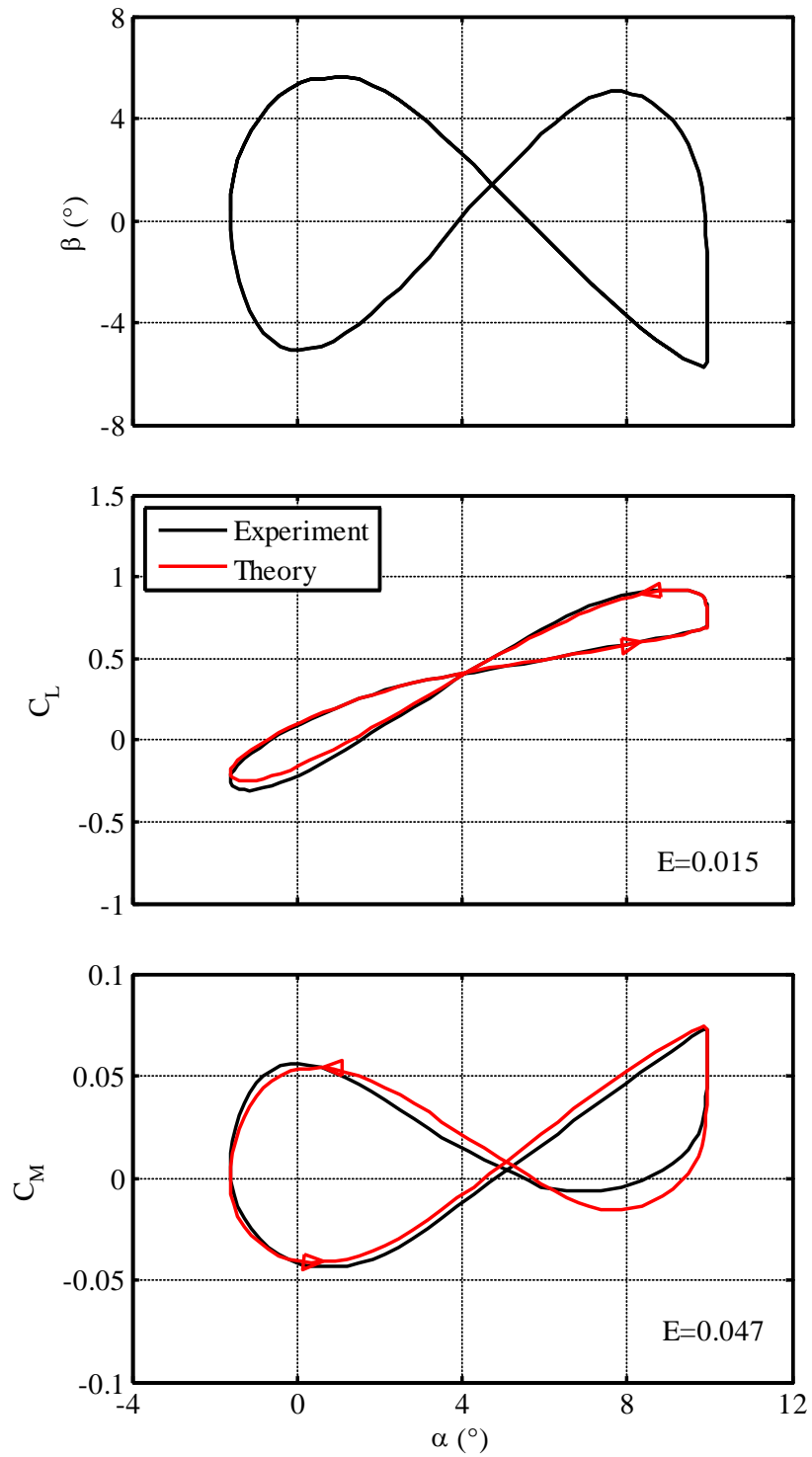


Figure 5.7: NACA 0012 airfoil with TE flap, moderate stall, $\phi = 206^\circ$.

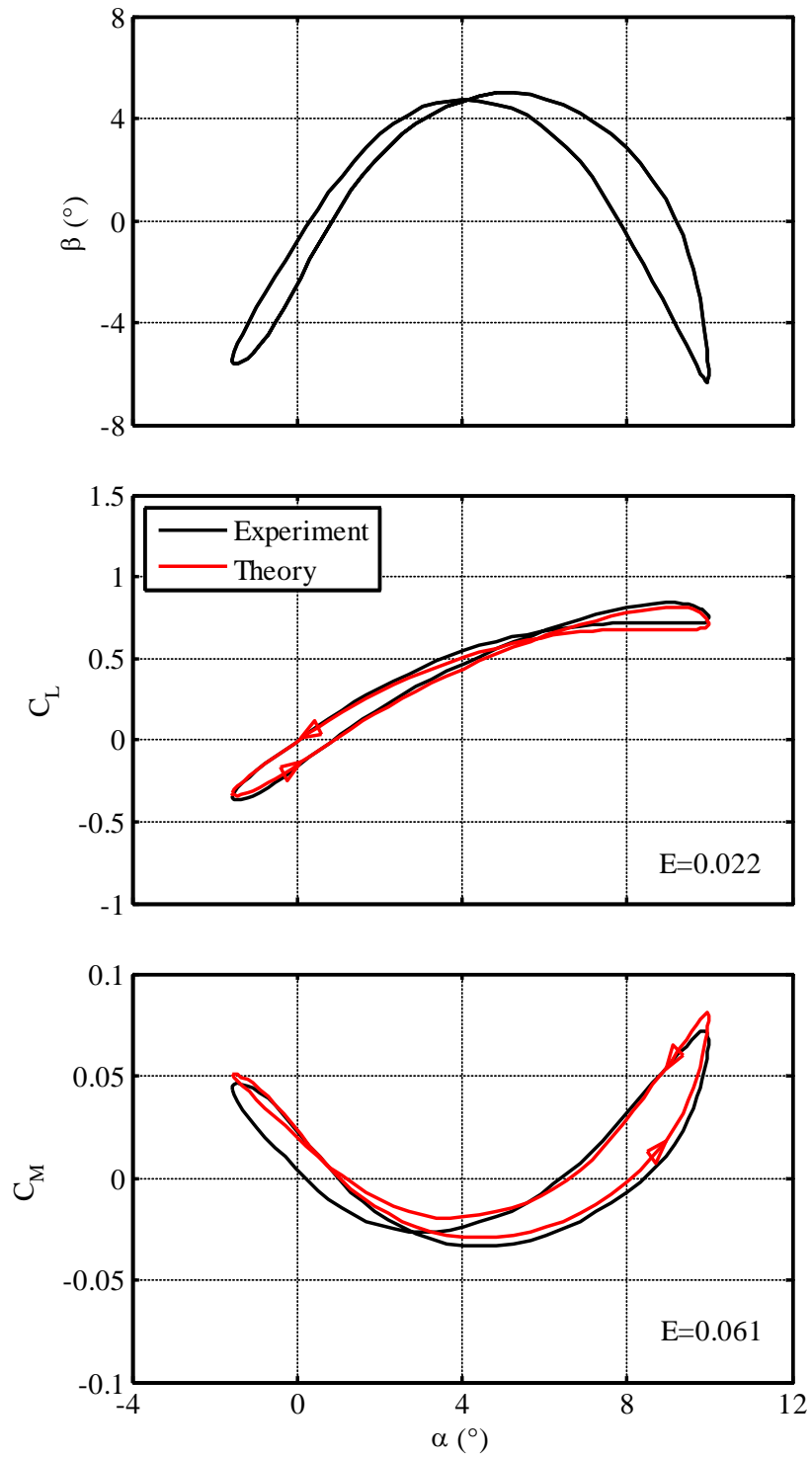


Figure 5.8: NACA 0012 airfoil with TE flap, moderate stall, $\phi = 298^\circ$.

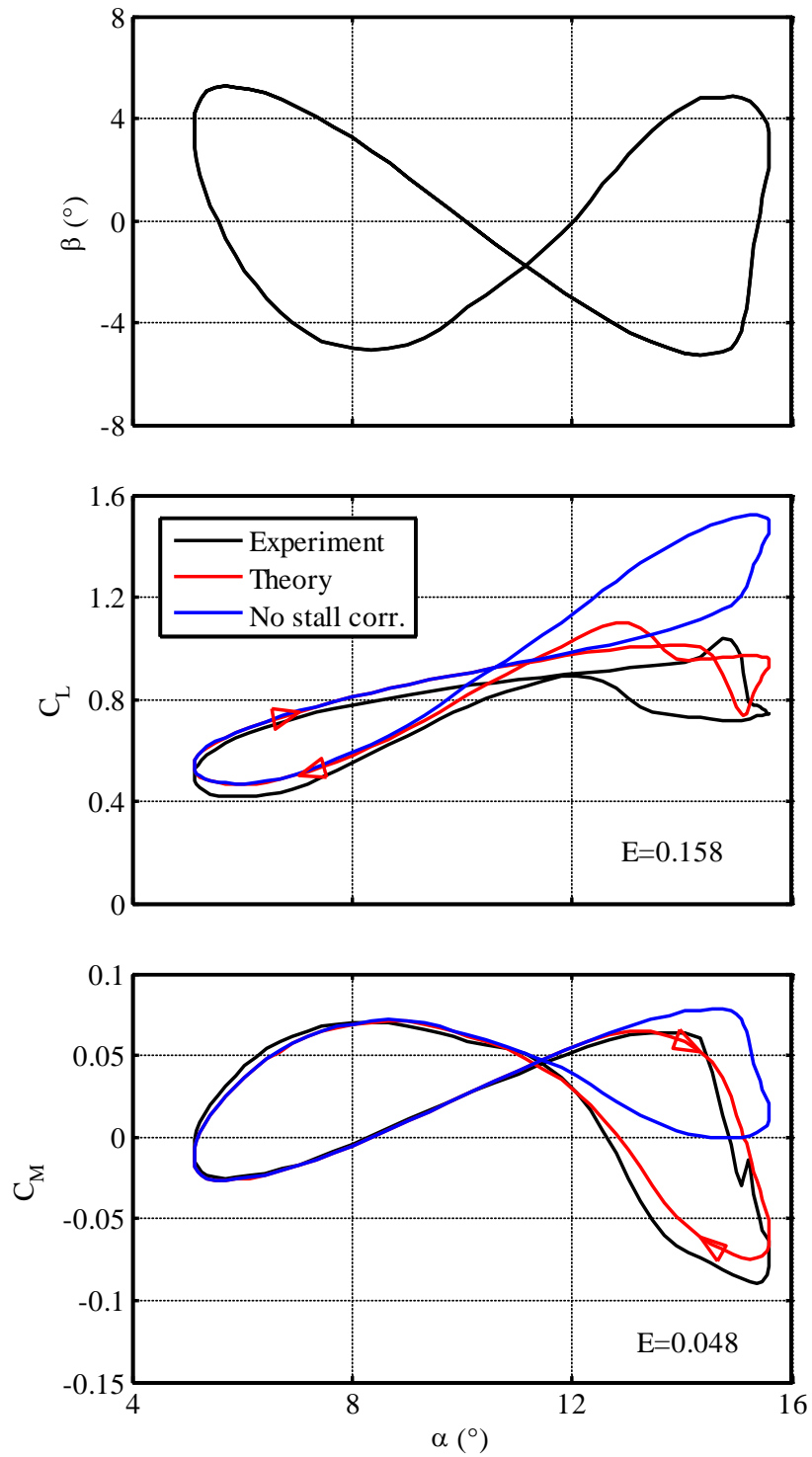


Figure 5.9: NACA 0012 airfoil with TE flap, heavy stall, $\phi = 177^\circ$.

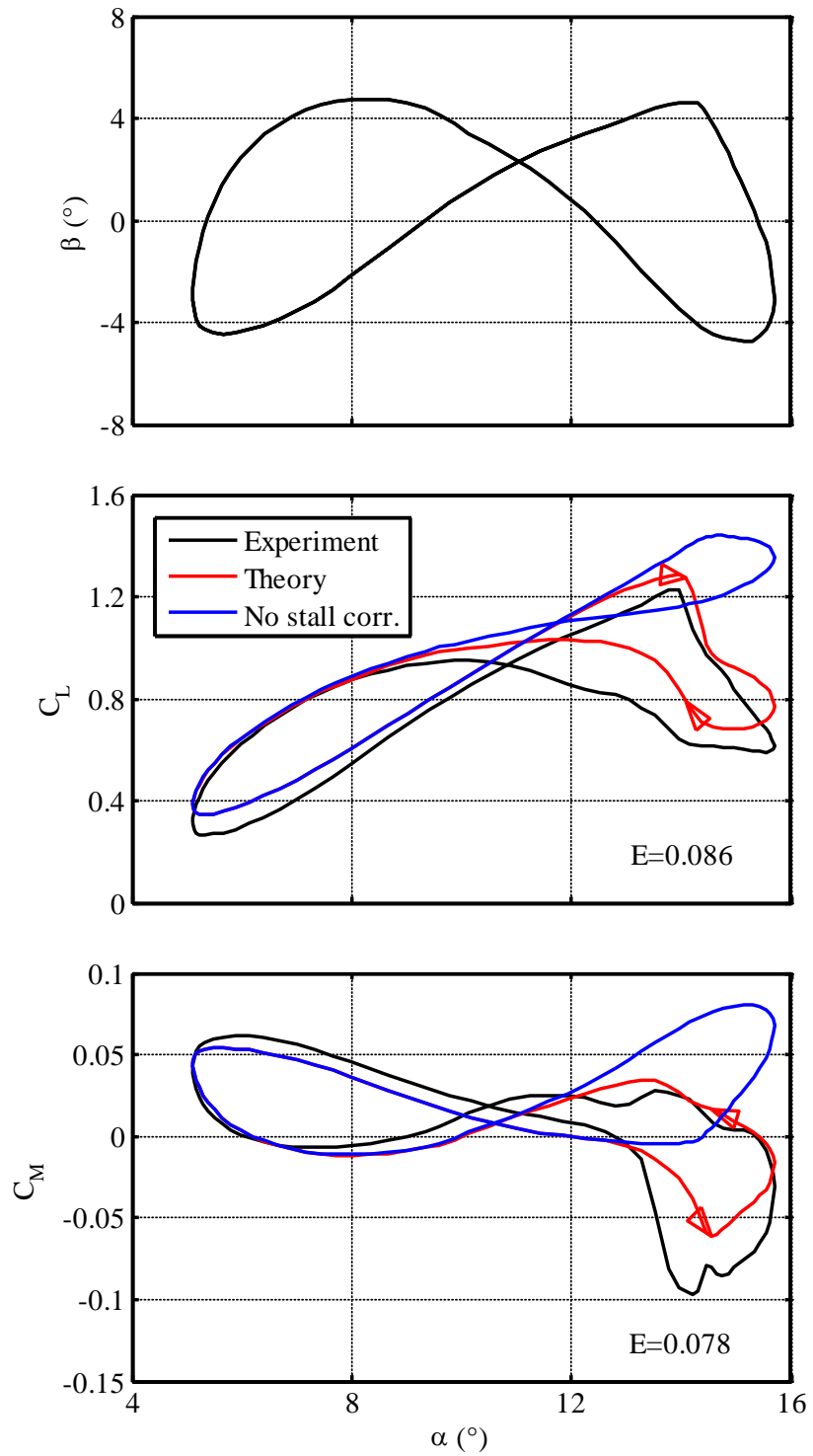


Figure 5.10: NACA 0012 airfoil with TE flap, heavy stall, $\phi = 343^\circ$.

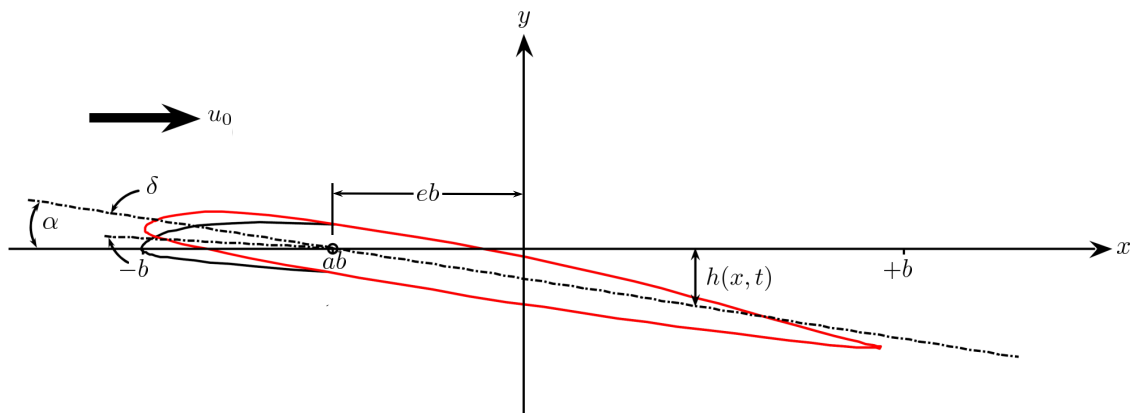


Figure 5.11: Experimental setup of VR-12 drooped leading-edge airfoil.

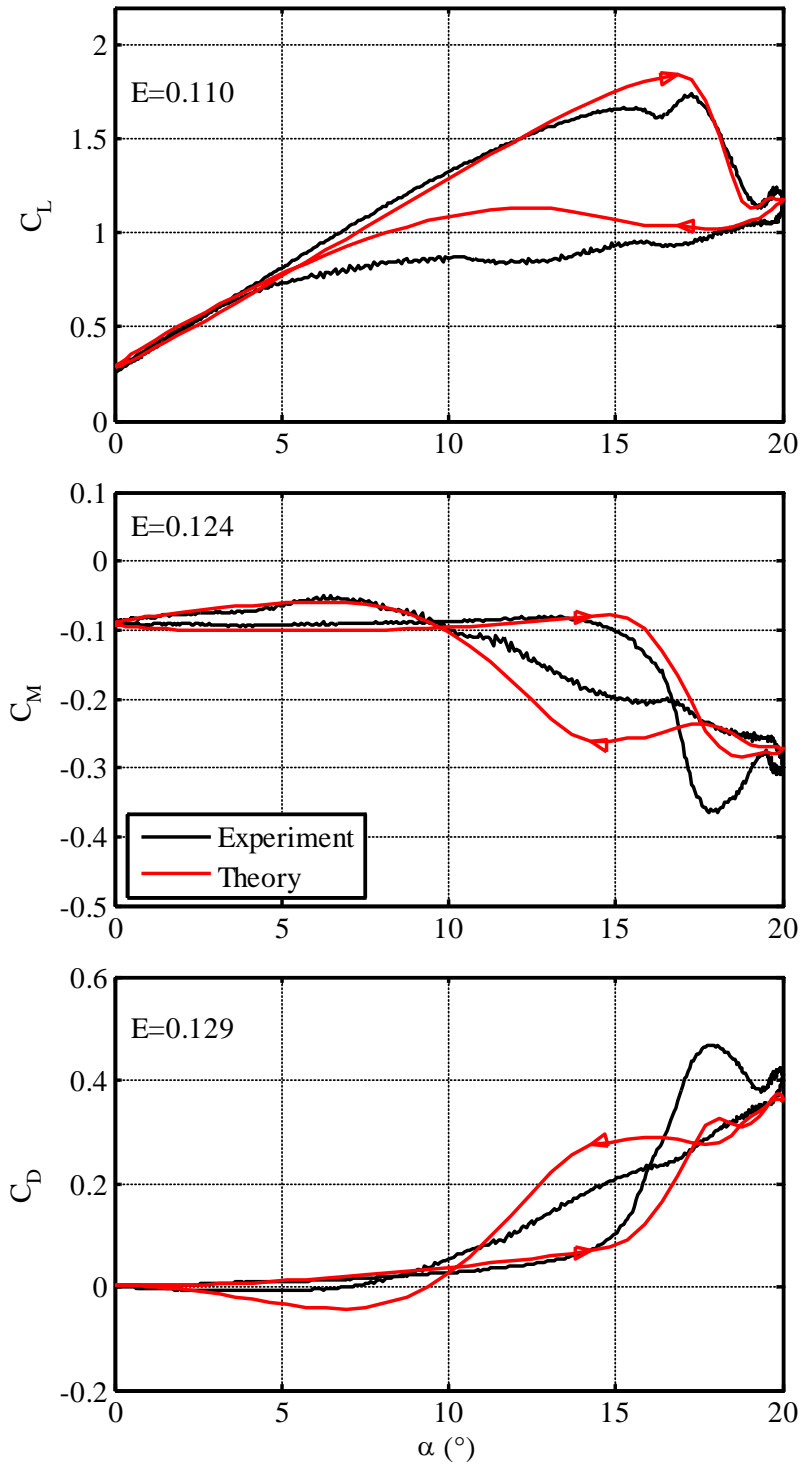


Figure 5.12: Dynamic airload correlation, VR-12 baseline airfoil, $k=0.05$, $M=0.2$

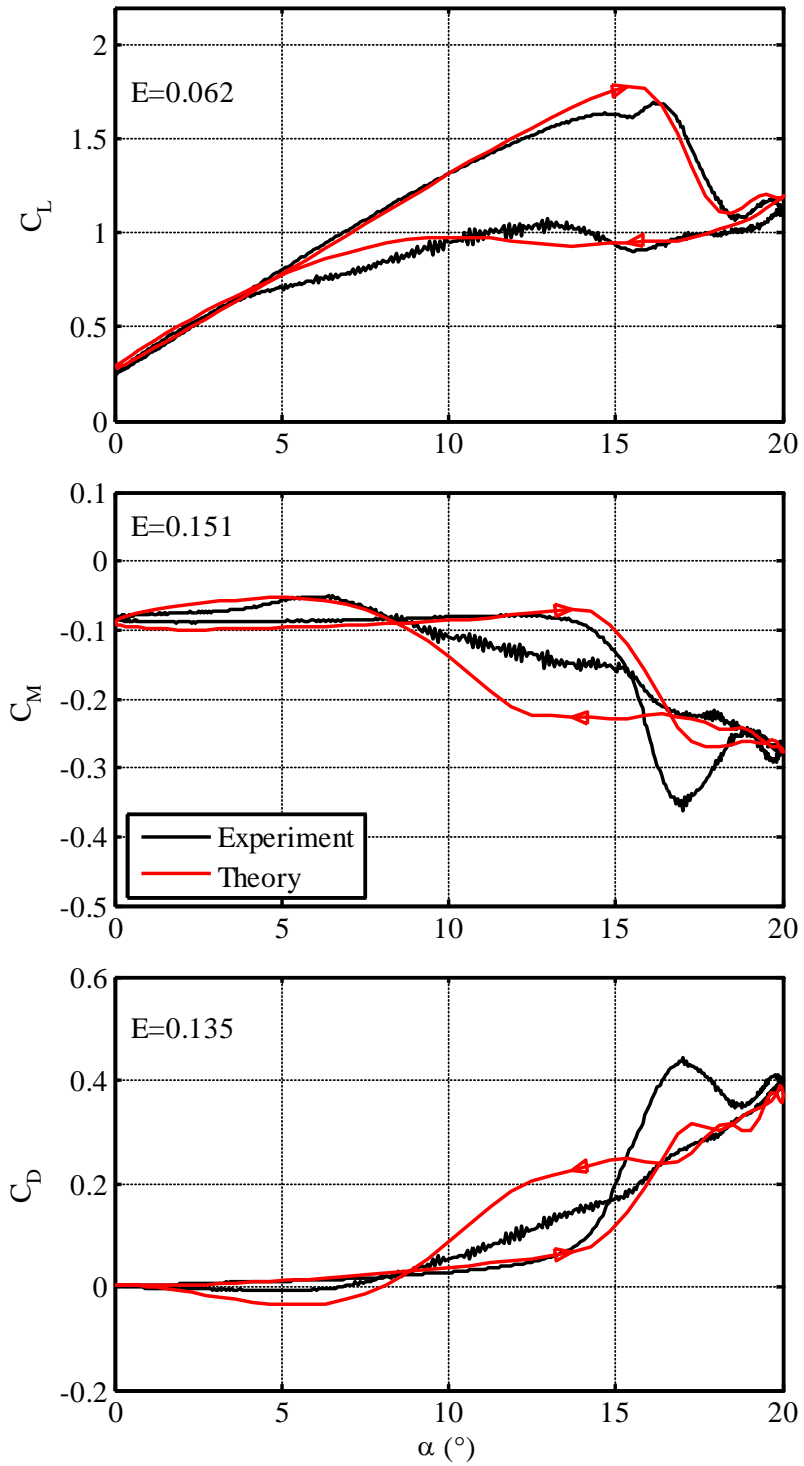


Figure 5.13: Dynamic airload correlation, VR-12 baseline airfoil, $k=0.05$, $M=0.3$

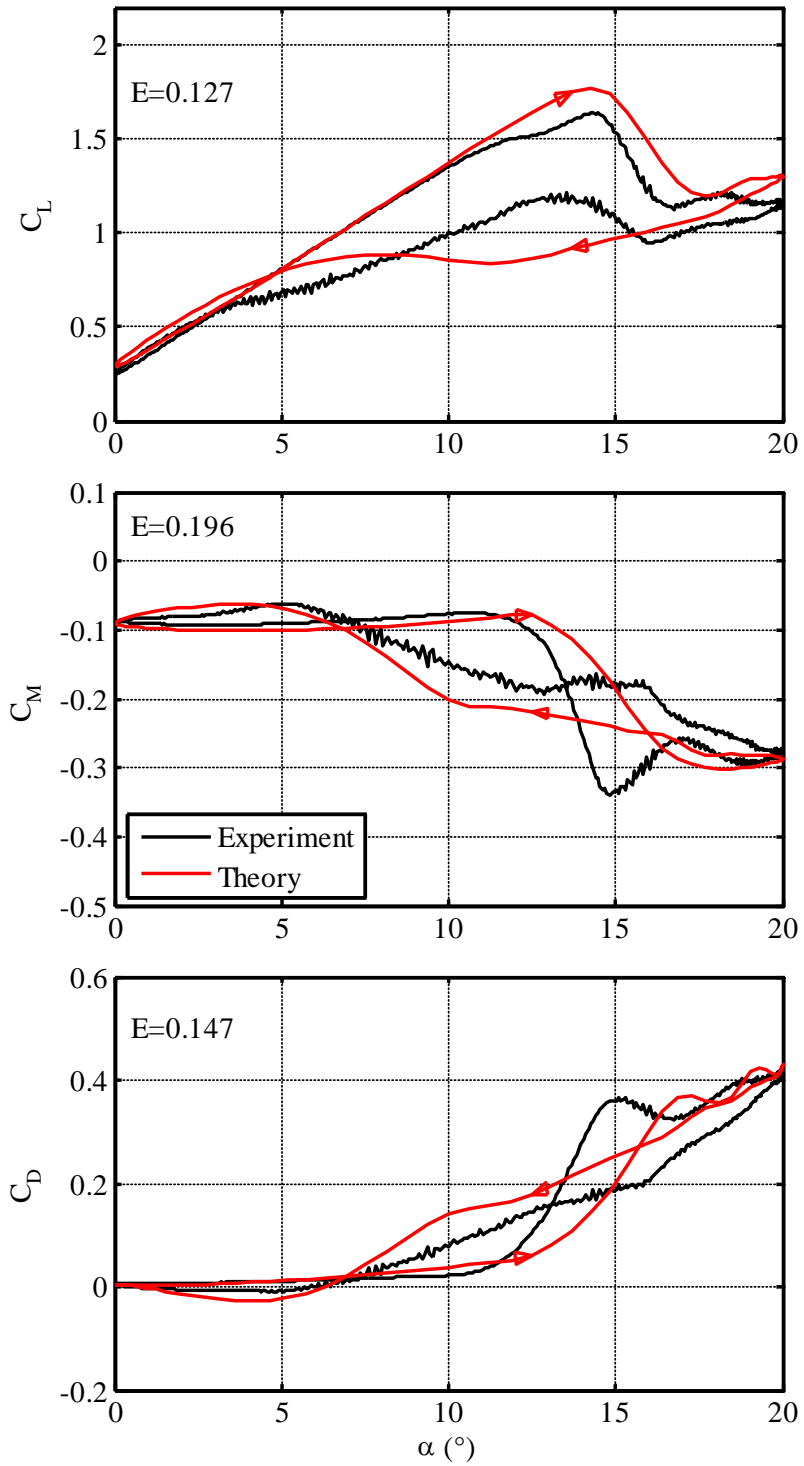


Figure 5.14: Dynamic airload correlation, VR-12 baseline airfoil, $k=0.05$, $M=0.4$

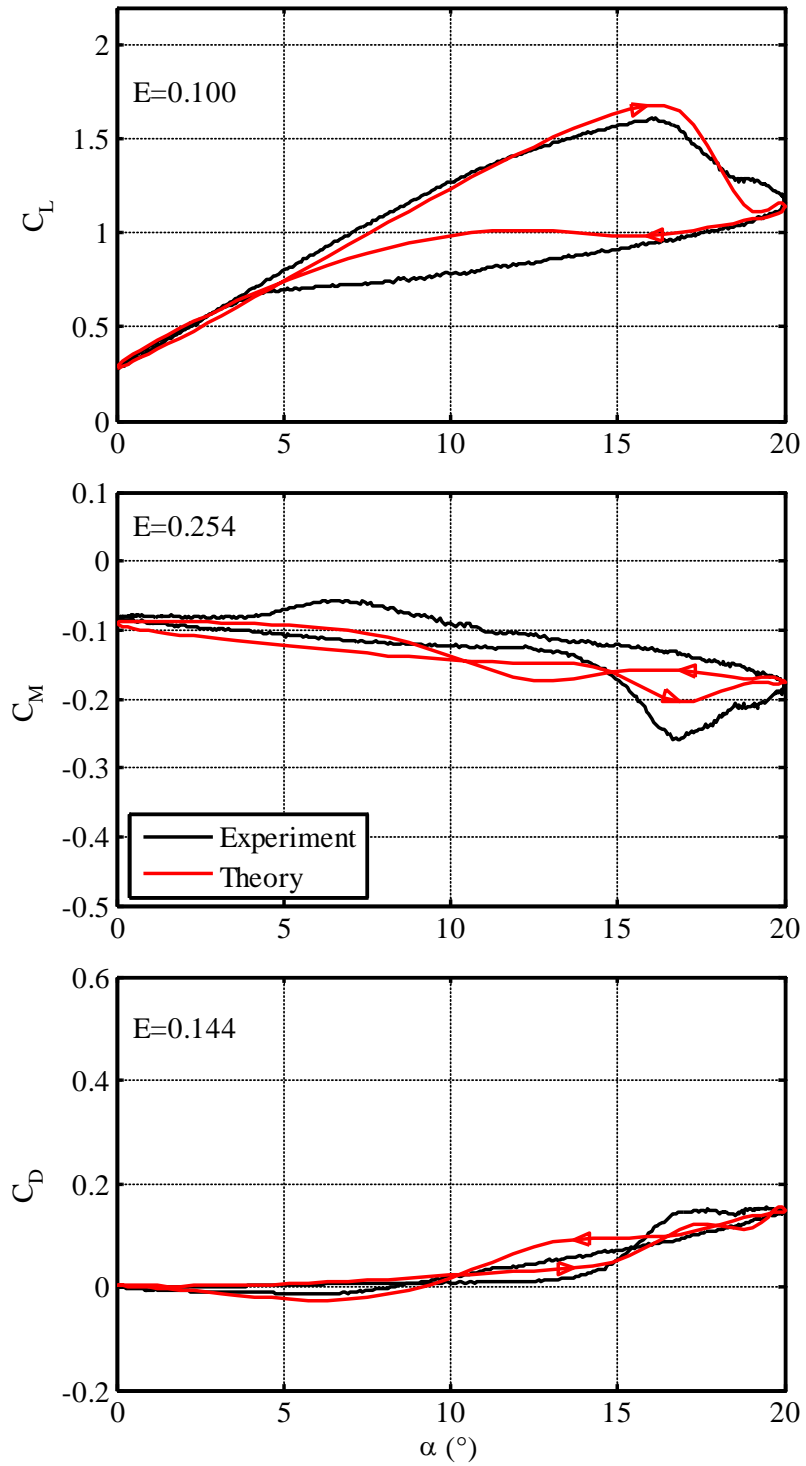


Figure 5.15: Dynamic airload correlation, VR-12 20° variable droop, $k=0.05$, $M=0.2$

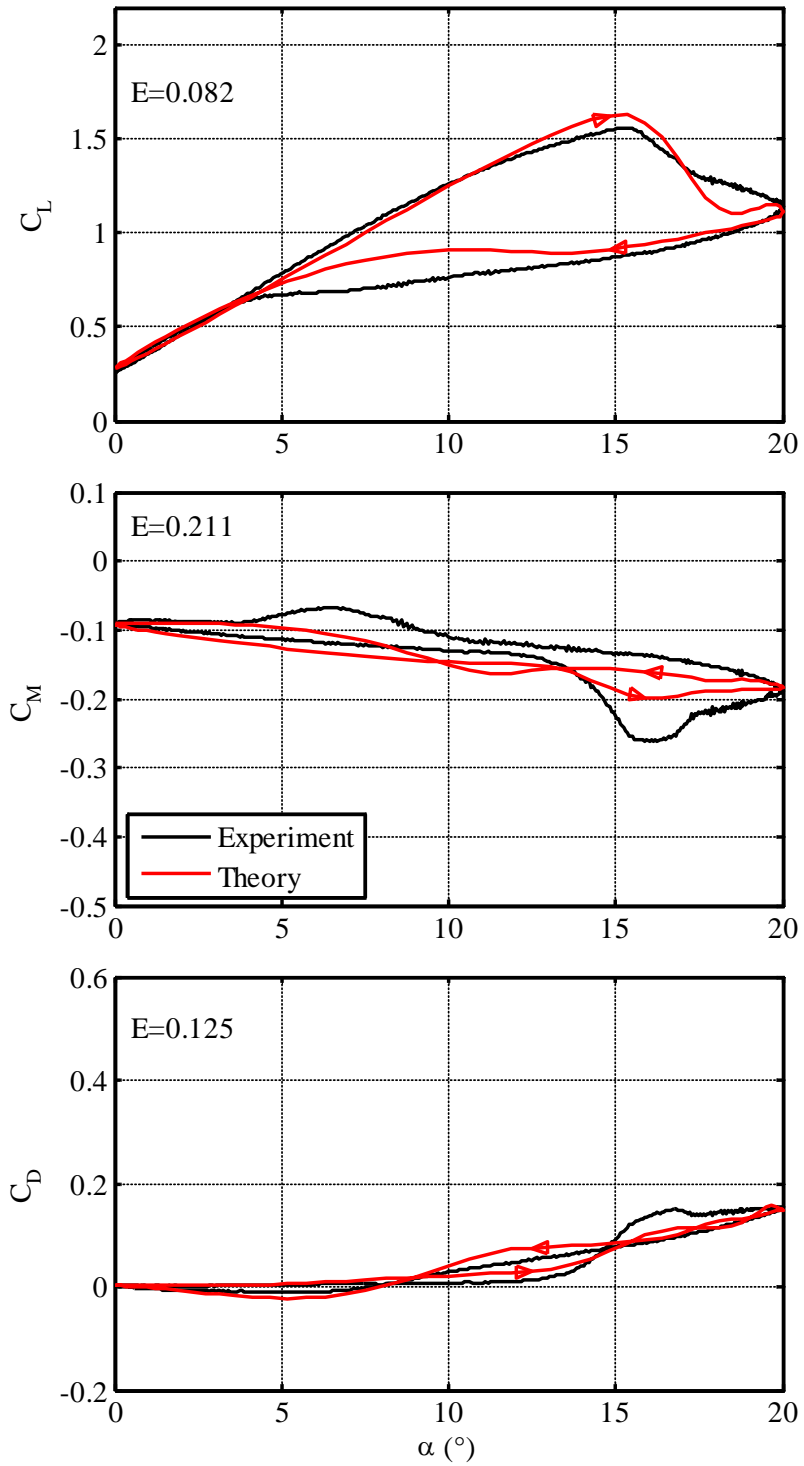


Figure 5.16: Dynamic airload correlation, VR-12 20° variable droop, $k=0.05$, $M=0.3$

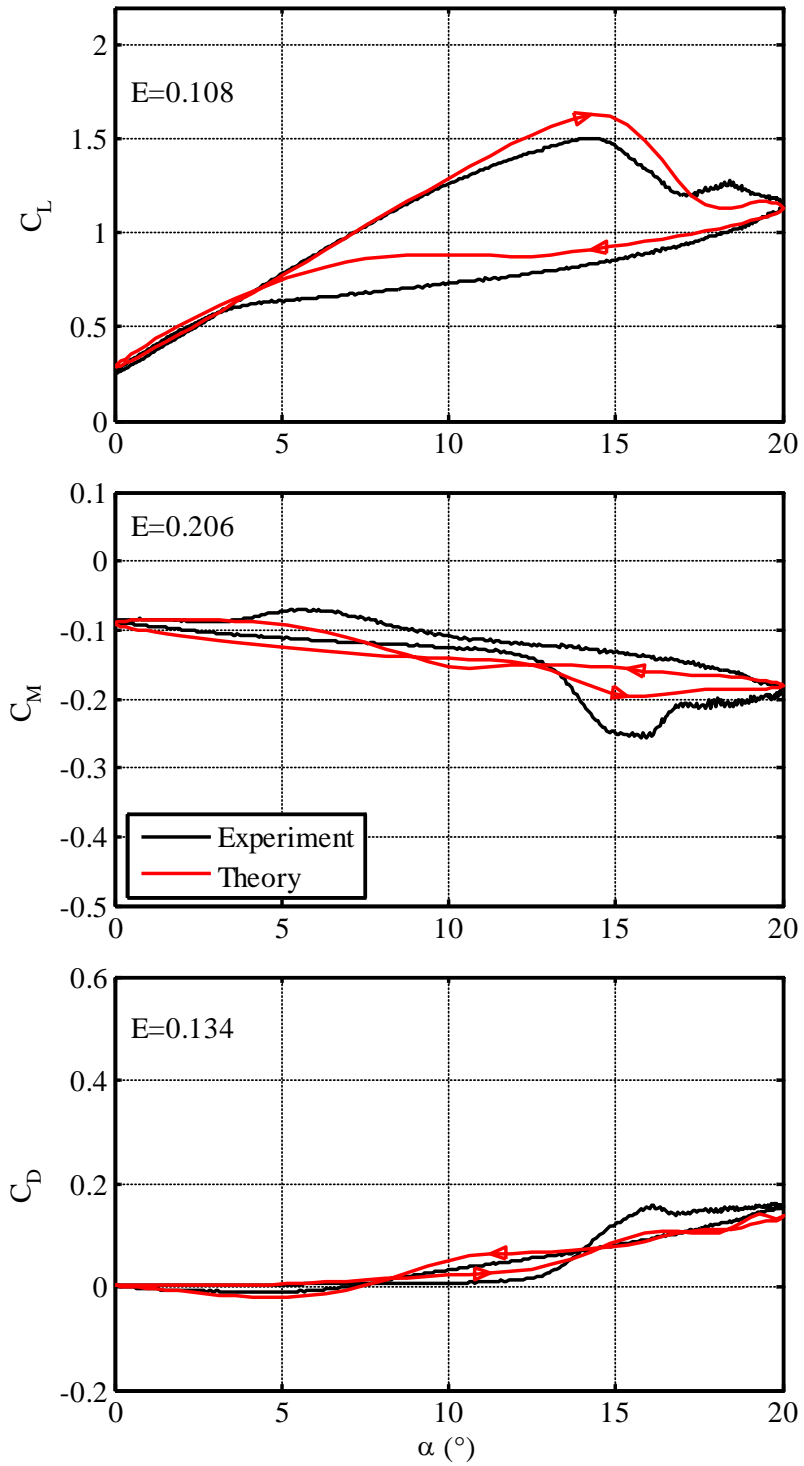


Figure 5.17: Dynamic airload correlation, VR-12 20° variable droop, $k=0.05$, $M=0.4$

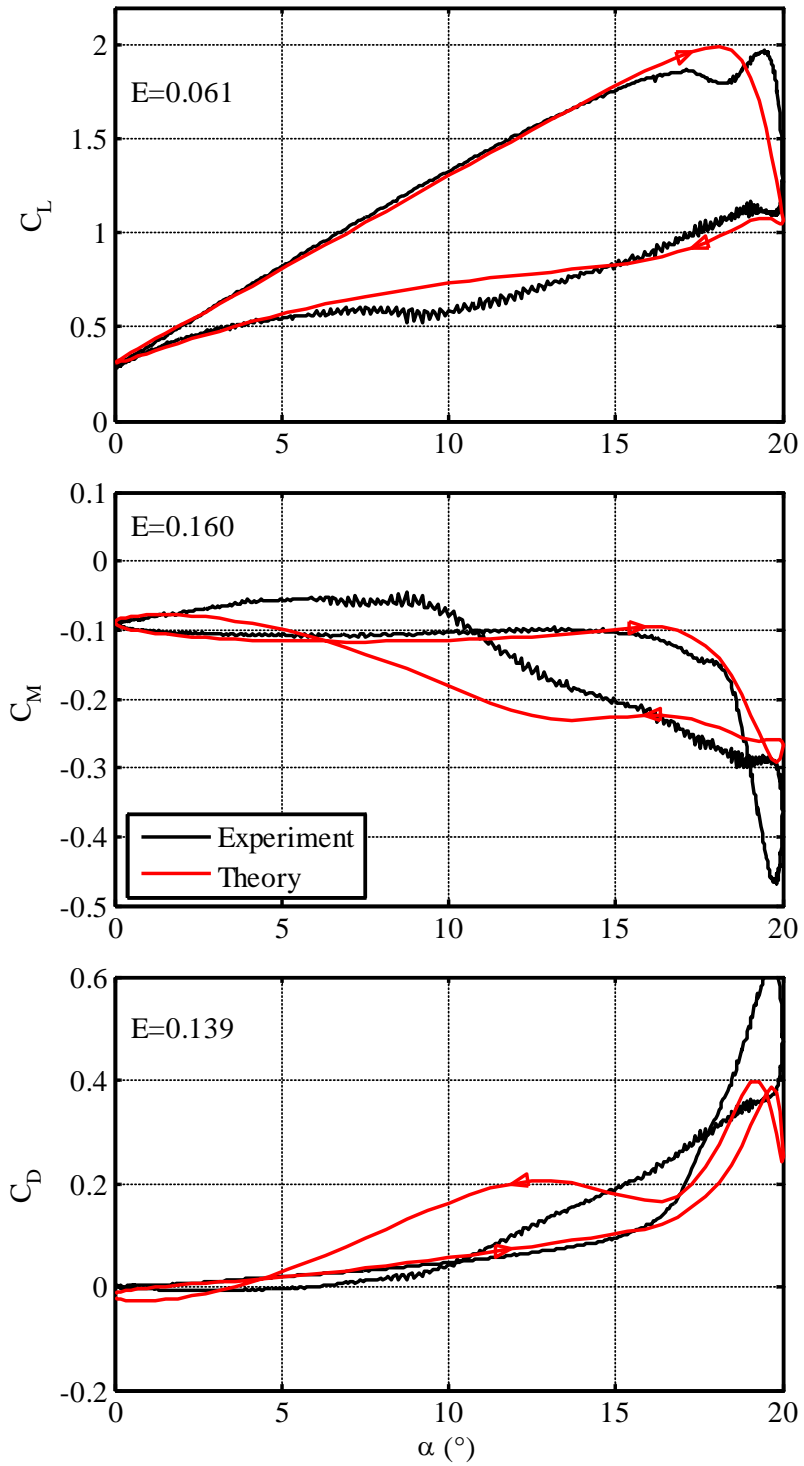


Figure 5.18: Dynamic airload correlation, VR-12 baseline airfoil, $k=0.10$, $M=0.2$

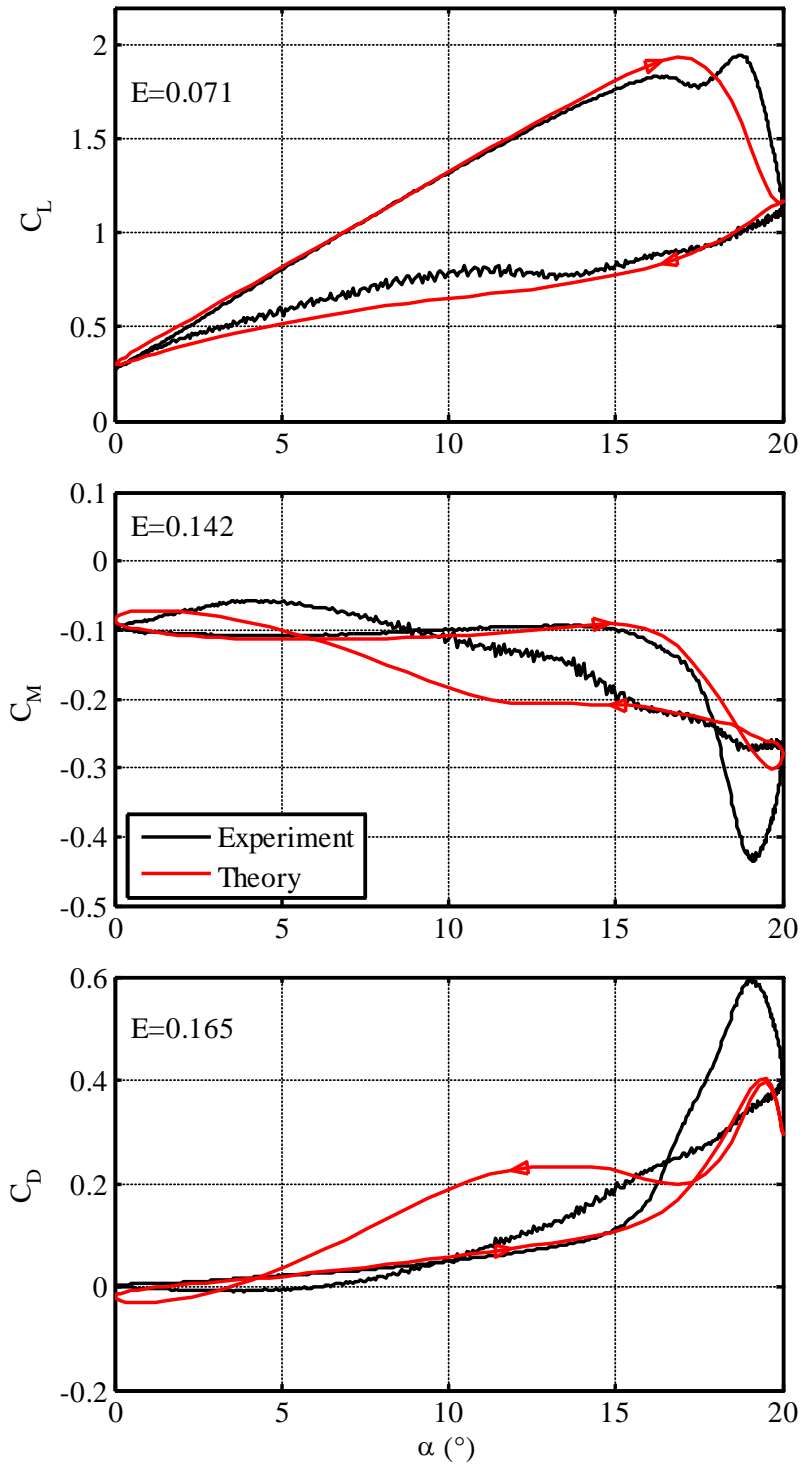


Figure 5.19: Dynamic airload correlation, VR-12 baseline airfoil, $k=0.10$, $M=0.3$

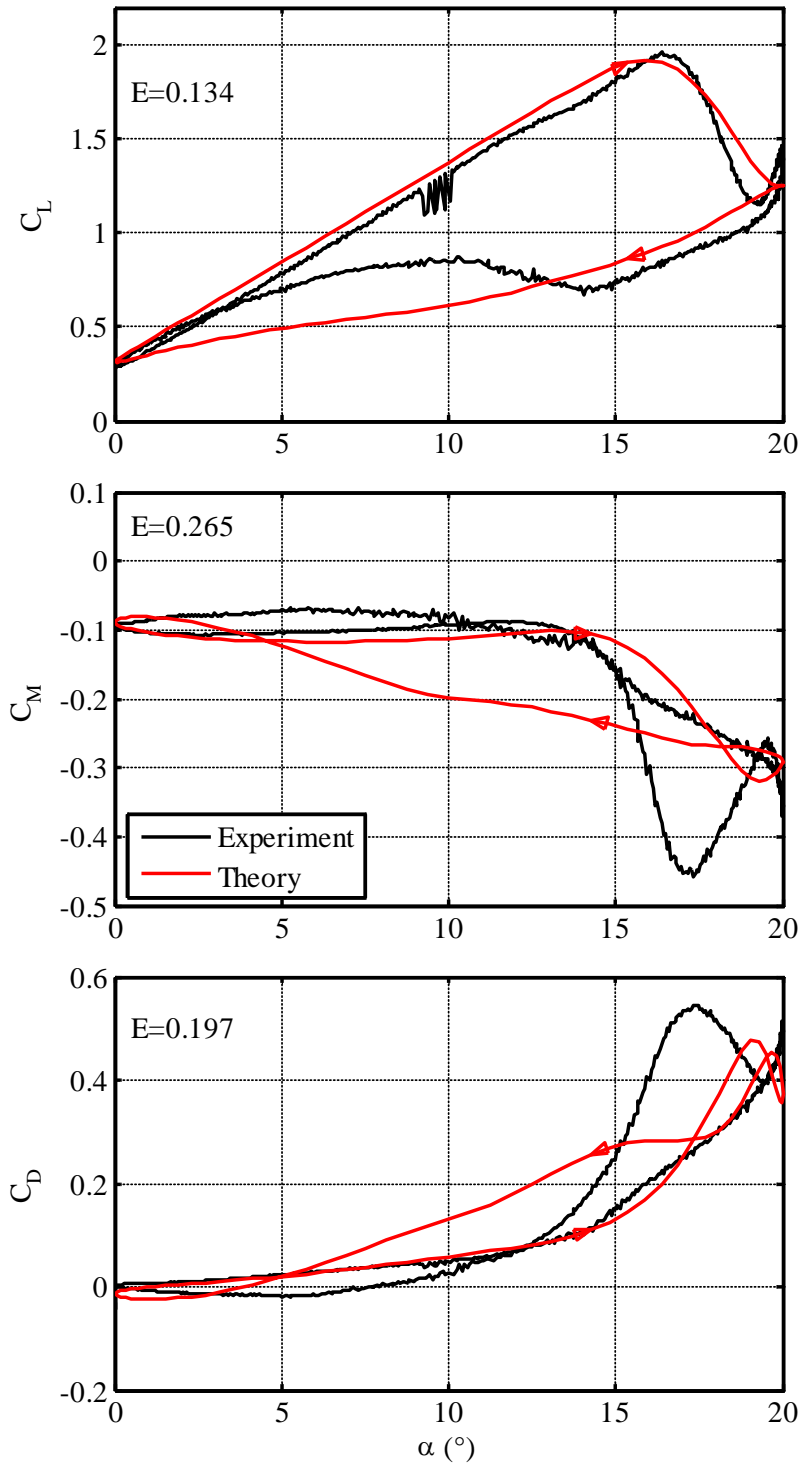


Figure 5.20: Dynamic airload correlation, VR-12 baseline airfoil, $k=0.10$, $M=0.4$

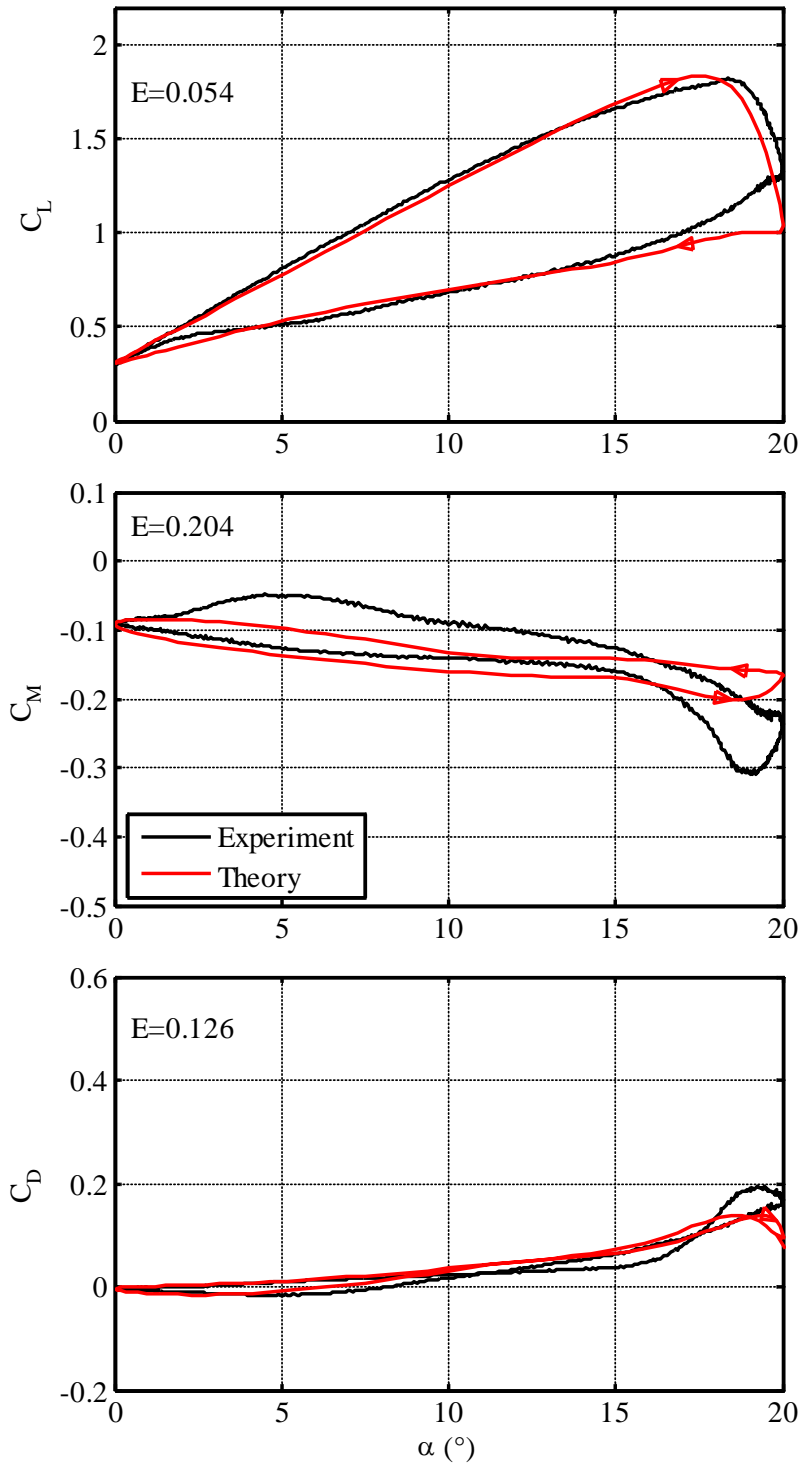


Figure 5.21: Dynamic airload correlation, VR-12 20° variable droop, $k=0.10$, $M=0.2$

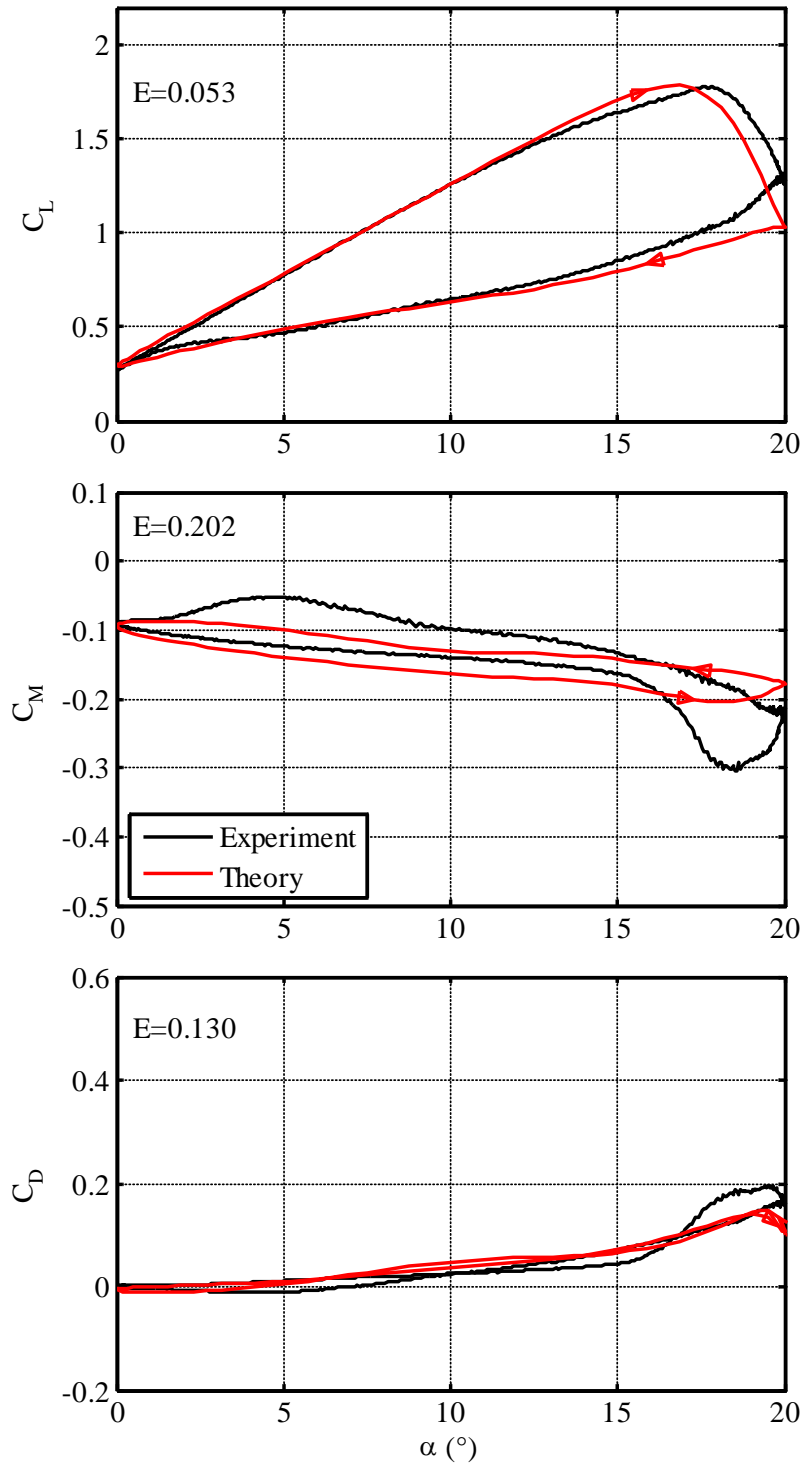


Figure 5.22: Dynamic airload correlation, VR-12 20° variable droop, $k=0.10$, $M=0.3$

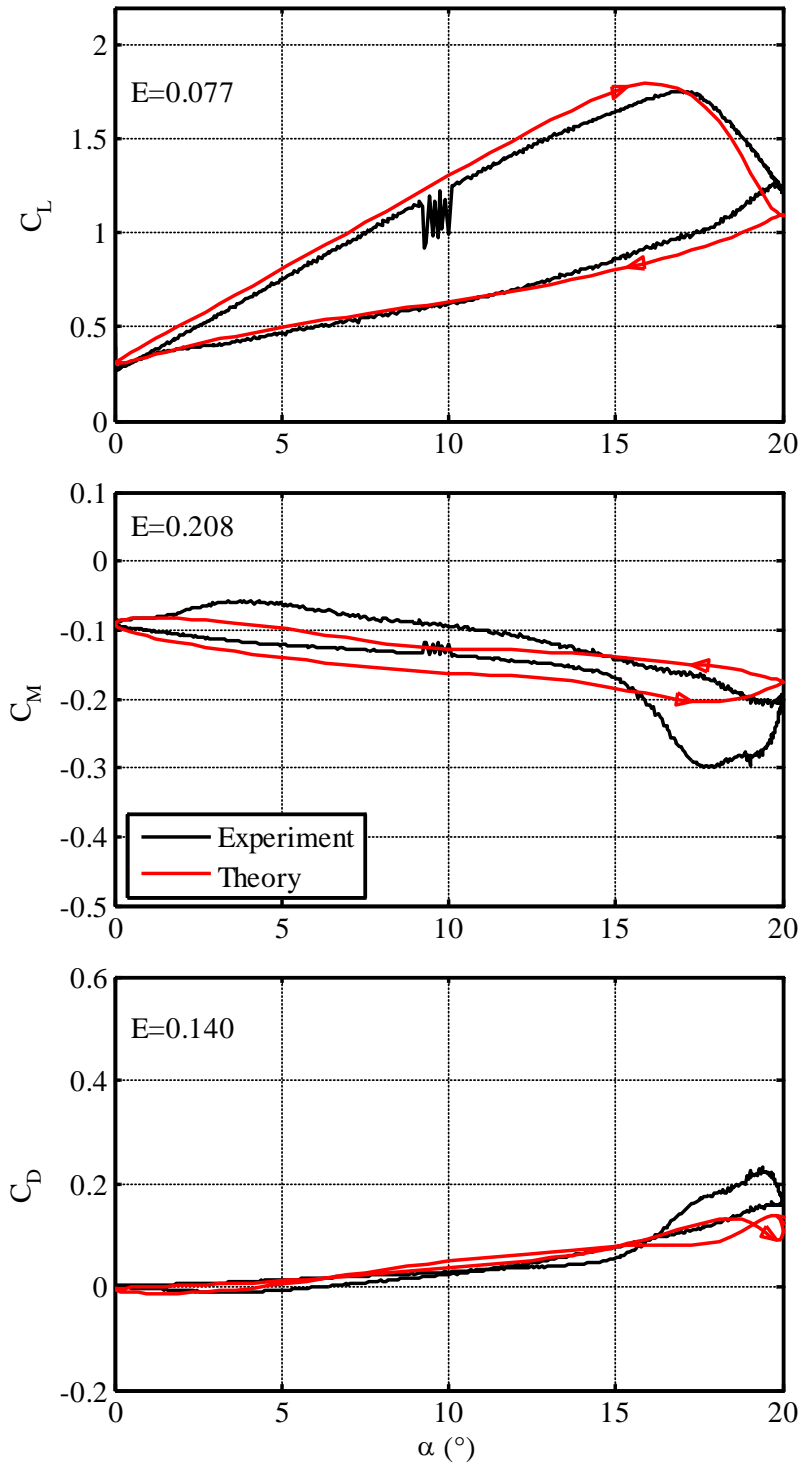


Figure 5.23: Dynamic airload correlation, VR-12 20° variable droop, $k=0.10$, $M=0.4$

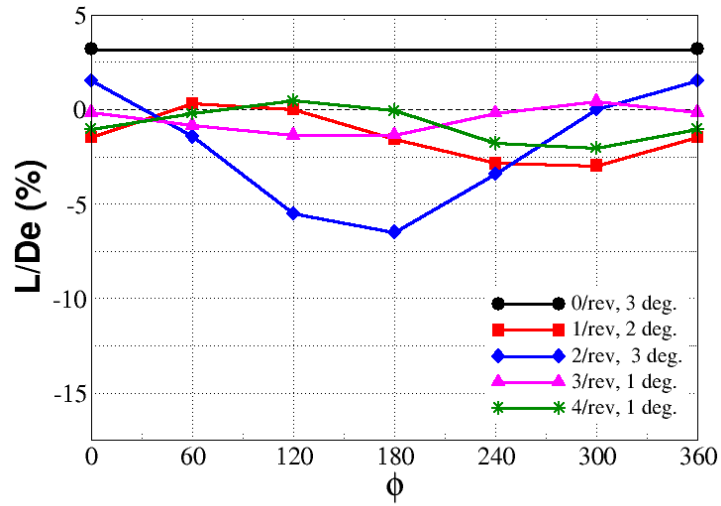


Fig. 25. Rotor performance variation using harmonic LED for the flight condition C9017 computed using lifting-line comprehensive analysis

Figure 5.24: Figure 25 of Ref. [50], reprinted for comparison.

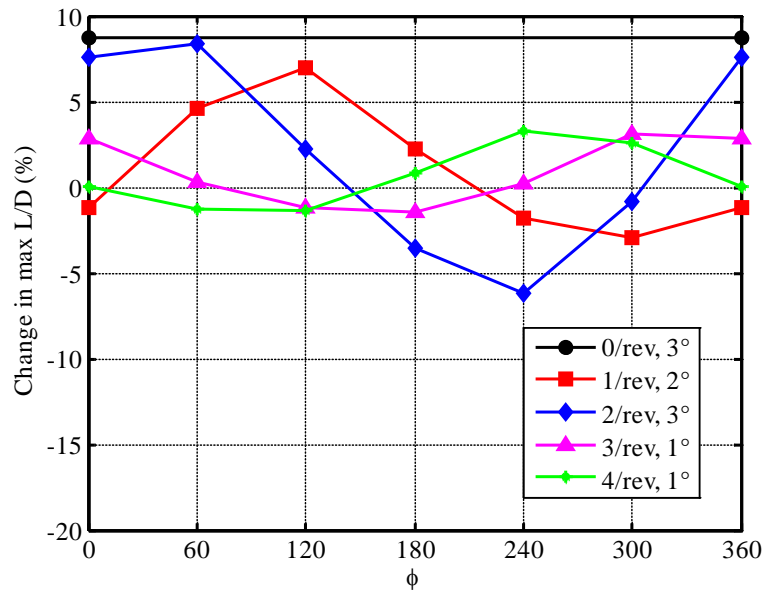


Figure 5.25: Change in airfoil L/D for various leading-edge deflections.

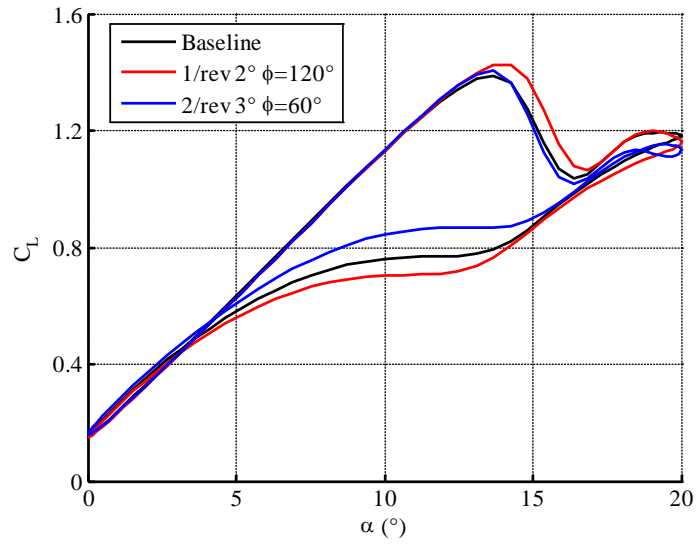


Figure 5.26: Lift coefficient for dynamic leading-edge deflection.

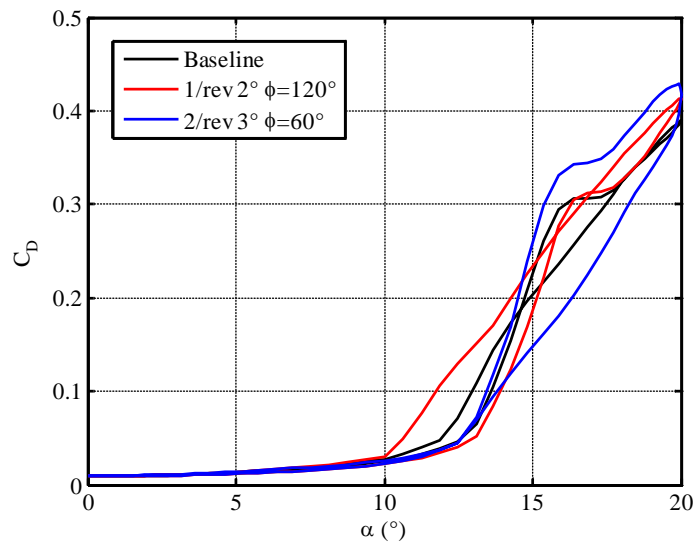


Figure 5.27: Quasi-steady drag coefficient for dynamic leading-edge deflection.

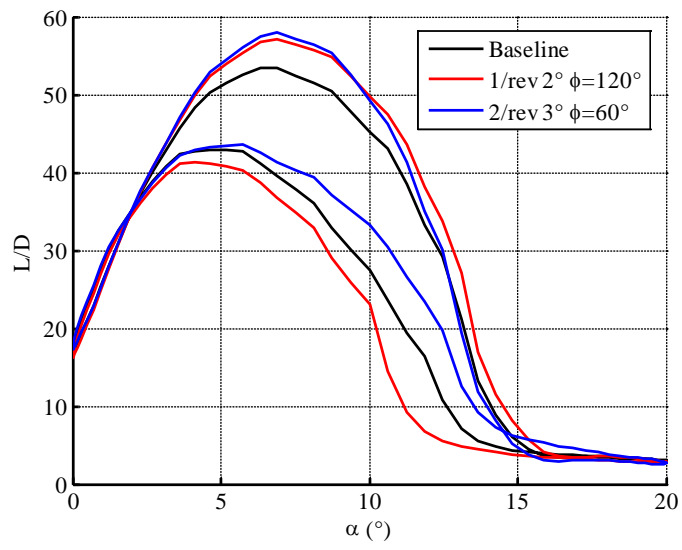


Figure 5.28: L/D ratio for dynamic leading-edge deflection.

Airfoil	M	Pitch Oscillation*			Morphing Variable*			Loads Correlated	Fig.	Error Norms		
		k	Mean	Amp.	k	Mean	Amp.			E_L	E_M	E_D
VR-12 Baseline	0.2	0.05	10.00	10.00	—	—	—	L, M, D	5.12	0.110	0.124	0.129
VR-12 Baseline	0.3	0.05	10.00	10.00	—	—	—	L, M, D	5.13	0.062	0.151	0.135
VR-12 Baseline	0.4	0.05	10.00	10.00	—	—	—	L, M, D	5.14	0.127	0.196	0.147
VR-12 VDLE	0.2	0.05	10.00	10.00	δ	10.00	10.00	L, M, D	5.15	0.100	0.254	0.144
VR-12 VDLE	0.3	0.05	10.00	10.00	δ	10.00	10.00	L, M, D	5.16	0.082	0.211	0.125
VR-12 VDLE	0.4	0.05	10.00	10.00	δ	10.00	10.00	L, M, D	5.17	0.108	0.206	0.134
VR-12 Baseline	0.2	0.10	10.00	10.00	—	—	—	L, M, D	5.18	0.061	0.160	0.139
VR-12 Baseline	0.3	0.10	10.00	10.00	—	—	—	L, M, D	5.19	0.071	0.142	0.165
VR-12 Baseline	0.4	0.10	10.00	10.00	—	—	—	L, M, D	5.20	0.134	0.265	0.197
VR-12 VDLE	0.2	0.10	10.00	10.00	δ	10.00	10.00	L, M, D	5.21	0.054	0.204	0.126
VR-12 VDLE	0.3	0.10	10.00	10.00	δ	10.00	10.00	L, M, D	5.22	0.053	0.202	0.130
VR-12 VDLE	0.4	0.10	10.00	10.00	δ	10.00	10.00	L, M, D	5.23	0.077	0.208	0.140
NACA 0012 Baseline	0.3	0.025	10.00	5.00	—	—	—	L	4.6	0.016	—	—
NACA 0012 Baseline	0.3	0.10	10.00	5.00	—	—	—	L	4.6	0.018	—	—
NACA 0012 Flap ($\phi = 59^\circ$)	0.4	0.02	0.00	6.00	β	0.04	5.50	L, M	5.3	0.017	0.036	—
NACA 0012 Flap ($\phi = 115^\circ$)	0.4	0.02	0.00	6.00	β	0.04	5.50	L, M	5.4	0.016	0.044	—
NACA 0012 Flap ($\phi = 235^\circ$)	0.4	0.02	0.00	6.00	β	0.04	5.50	L, M	5.5	0.010	0.040	—
NACA 0012 Flap ($\phi = 135^\circ$)	0.4	0.02	5.00	5.50	β	0.04	5.00	L, M	5.6	0.016	0.049	—
NACA 0012 Flap ($\phi = 196^\circ$)	0.4	0.02	4.50	5.75	β	0.04	5.00	L, M	5.7	0.015	0.047	—
NACA 0012 Flap ($\phi = 285^\circ$)	0.4	0.02	4.25	5.75	β	0.04	-0.50	L, M	5.8	0.022	0.061	—
NACA 0012 Flap ($\phi = 160^\circ$)	0.4	0.02	11.00	5.50	β	0.04	5.25	L, M	5.9	0.158	0.048	—
NACA 0012 Flap ($\phi = 323^\circ$)	0.4	0.02	11.00	5.50	β	0.04	4.75	L, M	5.10	0.086	0.078	—
SC1095 LE Droop	0.4	0.00	7.50	22.50	θ_{LE}	0.00	2.50	L, M	3.9-3.10	—	—	—
SC1095 LE Droop	0.4	0.05	10.00	10.00	θ_{LE}	0.00-0.20	0.00	L, D, L/D	5.25-5.28	—	—	—
SC1095 TE Droop	0.4	0.00	7.50	22.50	δ_{TE}	0.00	0.00	L, M	3.11-3.12	—	—	—

Table 5.1: Summary of airload correlations. (*Mean and Amp. are measured in degrees)

Chapter 6

Conclusions and Future Work

6.1 Conclusions

This thesis presents a unified model for determining the dynamic airloads for morphing airfoils. The model consists of three components: a flexible thin-airfoil theory for calculating the linear airloads, an induced flow model, and a dynamic stall model. Each of the components is validated by correlation to classical aerodynamic theories and published wind tunnel data.

In Chapter 2, the derivation of the unified model is presented. First, the Peters/Johnson Flexible Airfoil theory is derived from first principles, based on inviscid, incompressible, 2D potential flow. Although the incompressibility assumption is made in the derivation, the Prandtl-Glauert correction can be used for subsonic Mach numbers. In previous work, numerous validations of the theory have demonstrated that the theory recovers classical aerodynamic results, such as Theodorsen, Greenberg and Loewy theories. The theory is couched in terms of generalized airfoil deformations, which allows for arbitrary morphing of the meanline geometry. The airload theory is coupled with the Karunamoorthy two-dimensional inflow model. It is shown that this model provides a very good approximation to the Theodorsen lift deficiency function when used with eight states. Finally, a dynamic stall model is proposed, based on the ONERA second-order dynamic filter approach.

In order to implement the dynamic stall model, the static stall residuals must be known for each airfoil being studied. In Chapter 3, we illustrate an approach of building these static databases for three different airfoils:

1. NACA 0012 airfoil with trailing-edge flap
2. Boeing VR-12 airfoil with variable droop leading edge
3. SC-1095 airfoil with LE and TE droop

First, the static stall residuals are computed from available static data (wind tunnel, CFD, lookup tables, etc.) for various values of the morphing variables. Then, the residuals are parameterized in terms of the generalized gradients h'_n . The results are synthesized into a static database that can be used for any morphology of the baseline airfoil.

When ONERA originally developed their dynamic stall model, the stall parameters $\hat{\omega}$, $\hat{\eta}$, and \hat{e} were determined by a large number of small-amplitude pitch oscillation tests conducted at a variety of mean angles of attack. That work validated their approach and suggested that the functional form of the parameters. In Chapter 4, we show that the dynamic stall parameters can alternatively be determined from large-amplitude wind tunnel test data, via a genetic optimization algorithm.

In Chapter 5, we present correlations to dynamic morphing airfoil data using the unified model. First, we show that the model recovers Theodorsen theory for both harmonic pitch motions and harmonic trailing-edge deflections. Second, eight dynamic cases are correlated for a NACA 0012 airfoil with trailing-edge flap deflections. Third, twelve dynamic cases are correlated for a VR-12 airfoil with dynamic leading-edge droop. Fourth, dynamic stall data for an SC-1095 airfoil are correlated and applied to morphing of that airfoil. All of the correlations demonstrate that the theory captures the essential physical behavior of dynamic stall. Although we have analyzed dynamic stall specifically for a NACA 0012 with a flap, a VR-12 with variable droop, and an SC-1095 with leading-edge droop, our model applies to any arbitrary morphing of these airfoils. One needs only be able to find h'_0 , h'_1 , and h'_2 in terms of the morphing variables of interest to be able to predict the corresponding C_L and C_M . If other loads are needed, such as a flap hinge moment, additional data would need to be supplied to determine the static corrections and post-stall behavior for those loads.

The three airfoils studied are typical of thin airfoil sections used on modern rotorcraft, with thickness ranging from 9.5% to 12%. Despite subtle differences in

geometry, the resulting constants that define the unified model are strikingly similar for each of these airfoils. Thus, the theory has been validated for an entire family of thin airfoils. If one were to analyze a similar airfoil, for which experimental data were not available, a reasonable approximation of the dynamic behavior can be made from an average of the coefficients determined in this work.

The current theory has many potential applications in the aerodynamic analysis of rotorcraft. In order to apply the model, the following data must be supplied by the user:

1. Static slopes for each desired airload with respect to each morphing variable, in order to obtain the static correction factors.
2. Stall initiation angle for various combinations of morphing variables. Only enough data need to be supplied so that the stall initiation angle may be parameterized in terms of the generalized spatial gradients h'_0 , h'_1 , and h'_2 .
3. Post-stall behavior of each airload of interest, averaged over various morphing combinations to obtain the stall residuals as a function of $\alpha - \alpha_{ss}$. This assumes that post-stall behavior is independent of morphing.
4. The dynamic stall parameters ω_0 , ω_2 , η_0 , η_2 , and e_2 for the basic unmorphed airfoil. These parameters may either be obtained from small-amplitude oscillations to develop the transfer function, as described in Ref. [31], or by an optimization procedure applied to large-amplitude data.

6.2 Required Constants

The present approach requires remarkably few experimental constants to implement the theory. For example, consider a baseline airfoil for which one would want dynamic stall simulations with C_L and C_M . (One would assume that either experimental or CFD data are available—giving these load coefficients as functions of angle of attack.) To implement the linear airfoil theory, one would match the theoretical lift-curve and moment slopes $C_{L\alpha}$ and $C_{M\alpha}$ with the data. This requires that **two** correction factors be added to the Johnson/Peters theory, f_L for the lift slope and a_{corr} for the moment

slope. Sometimes, the lift and moment offsets might need to be matched as well. To accomplish this, a residual h'_1 can be added to shift the lift and a residual h'_2 can be added to shift the moment. Thus, at most **four** constants are needed to match the static data. To implement the dynamic stall model, only **five** constants are required for the baseline airfoil: ω_0 , ω_2 , η_0 , η_2 , and e_2 . Thus, a total of **nine** parameters completely parameterize the baseline airfoil. Since the present theory utilizes Prandtl-Glauert Mach number corrections, these same **nine** parameters apply for all Mach numbers, all reduced frequencies, and both lift and pitching moment.

Next, consider that N_M morphing variables are introduced into the airfoil with N_L required morphing loads. In the linear region, the Johnson/Peters theory can be matched to the experimental data by addition of one correction factor f_M , one correction factor for each morphing variable f_β , and one correction factor for each morphing load f_n . (It is assumed that static data are available for the change in each load with respect to at least one morphing variable in order to express the behavior in terms of the generalized coordinates.) Therefore, $\mathbf{1} + \mathbf{N}_M + \mathbf{N}_L$ correction factors need be chosen to match the linear experimental data.

The same 5 constants for the baseline dynamic stall are used for the morphed airfoil as well. Therefore, stall response of all loads of the morphed airfoil (i.e., C_L , C_M , and the C_n), requires the evaluation of a single variable α_{shift} in order to apply the theory. (Note that α_{0L} is implicitly matched by the static corrections in the linear region.) This research shows that one can express $\alpha_{\text{shift}} = C_1 h'_1 + C_2 h'_2$. Thus, only **two** additional constants are needed independent of the number of morphing variables. The total parameters required for N_M morphing variables with N_L morphing loads is therefore $\mathbf{N}_M + \mathbf{N}_L + \mathbf{3}$.

For example, with one morphing variable and one morphing load (e.g., a trailing-edge flap and the moment about the flap hinge) one would require **nine** constants for the baseline and **five** additional constants for the morphed airfoil—for a total of **fourteen** constants to analyze dynamic stall. These constants apply to all Mach numbers, all reduced frequencies, all loads, and all combinations of morphing.

6.3 Future Work

This work is an important first step in opening up a new method of investigating dynamic stall for morphing airfoils. There are many directions one could choose to take from this point. Some possibilities for future work include:

1. Integration of the unified airloads model with the Peters/Garcia-Duffy 3D Dynamic Inflow model. The combined model would truly be a global analysis tool, which could accommodate arbitrarily morphing airfoils in hover, vertical flight, or forward flight. Each of these cases would need to be validated by comparison to flight tests and CFD. As an example, flight conditions C8534 and C9017 on the UH-60A were correlated by CFD in Ref. [50]. First, the flight test data were correlated to validate the CFD model. Then, various morphing airfoil scenarios were evaluated with CFD under the same conditions. A similar approach could be applied to the unified airloads model.
2. There is keen interest in developing active control methodologies for improvements in efficiency, and reduction in vibratory loads. The approach for most of these investigations is to optimize each parameter independently. For example, key design parameters for a trailing-edge flap may include chord, span, radial location, and deployment schedule. Each of these parameters is evaluated independently, often involving lengthy CFD runs, while the other parameters are fixed. Due to the computational expense of CFD, it is not feasible to optimize all of the parameters simultaneously. However, the unified airload model can provide results in a fraction of the time required for CFD. This makes it possible to use a genetic algorithm or other optimization approach to simultaneously optimize all of the parameters. This may result in an improved global optimum.
3. A similar approach could be used to evaluate morphing wind turbine blades to reduce vibratory loads. This may be particularly useful for turbines that operate in yawed flow during high-wind conditions.
4. Characterize the static load residuals and dynamic stall parameters for additional airfoils that are currently used in production rotorcraft and wind turbines.

5. Quantify the effect of Mach number on the dynamic stall parameters by analyzing dynamic data for a variety of Mach numbers on the same airfoil.
6. Comparisons should be made between this approach and CFD computations in order to obtain the relative realms of applicability of each method. Such a comparison effort has begun with our partners at Georgia Institute of Technology. The results will be published at the 2010 European Rotorcraft Forum [57]. A sample correlation is shown in Fig. 6.1. For this case the nominal motion of the airfoil is given by

$$\alpha = 4.25^\circ + 5.75^\circ \sin kt$$
$$\beta = -0.5^\circ + 5.5^\circ \sin(2kt - 285^\circ)$$

However, the actual motions were not simple harmonic due to error in the experiment. The correlation of the CFD data is dependent on the modeling the wind tunnel wall, as well as the turbulence model used in the computations. Further study will provide insight on comparison of the unified airloads model to CFD data.

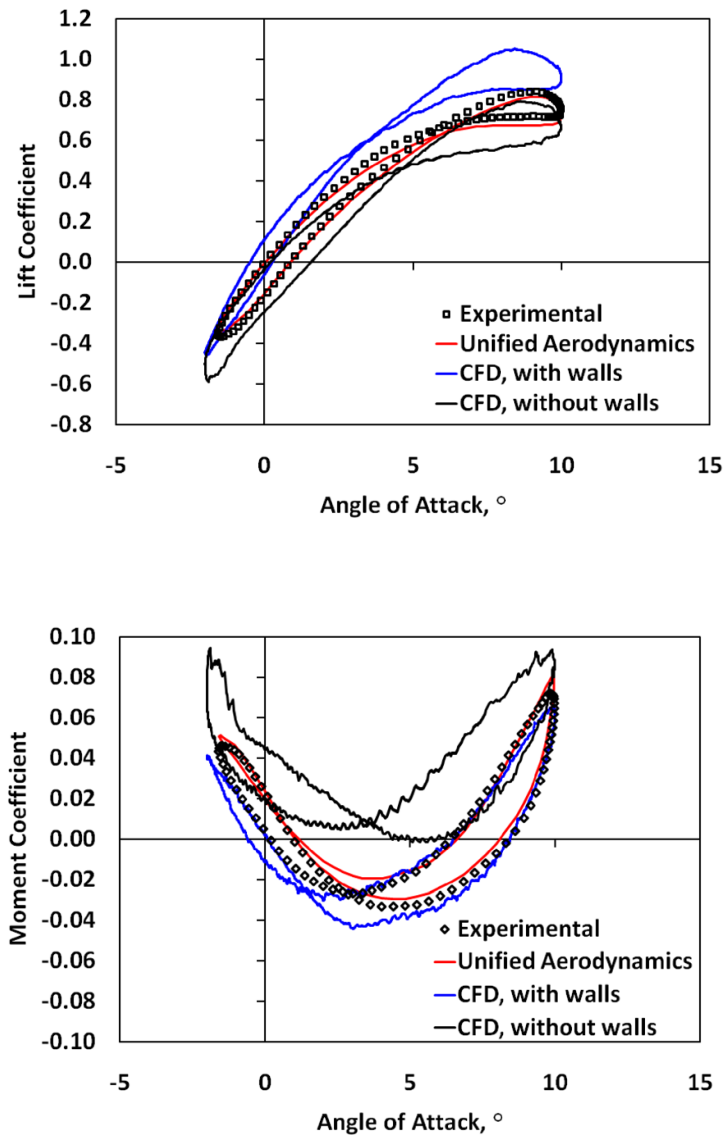


Figure 6.1: Comparison of unified model with CFD for NACA 0012 with TE flap.

Appendix A

Definition of Matrices and Vectors

This appendix defines the matrices and vectors used in the derivation of the unified model. Note that M refers to the number of states in the Glauert expansion, resulting in $(M + 1) \times (M + 1)$ matrices and $(M + 1) \times 1$ vectors. N refers to the number of inflow states, resulting in $N \times N$ matrices and $N \times 1$ vectors.

$$\{1\} = \{1 \ 0 \ 0 \ 0 \ \dots\}^T$$

$$\{b\} = \{b_1 \ b_2 \ b_3 \ \dots \ b_N\}^T \text{ as defined by Eq. (2.24)}$$

$$\{c\} = \{2 \ 1 \ \frac{2}{3} \ \frac{1}{2} \ \dots \ \frac{2}{N}\}^T$$

$$\{d\} = \{\frac{1}{2} \ 0 \ 0 \ 0 \ \dots\}^T$$

$$\{e\} = \{1 \ \frac{1}{2} \ 0 \ 0 \ \dots\}^T$$

$$\{f\} = \{0 \ 1 \ 2 \ \dots \ M\}^T$$

$$\{h_n\} = \{h_0 \ h_1 \ h_2 \ \dots \ h_M\}^T$$

$$\{v_n\} = \{v_0 \ v_1 \ 0 \ 0 \ \dots\}^T$$

$$\{\dot{v}_n + \ddot{h}_n\} = \left\{ \dot{v}_0 + \ddot{h}_0 \ \dot{v}_1 + \ddot{h}_1 \ 0 \ 0 \ \dots \right\}^T$$

$$\{\lambda_0\} = \{\lambda_0 \ 0 \ 0 \ 0 \ \dots\}^T$$

$$\{\lambda_1\} = \{\lambda_0 \ \lambda_1 \ 0 \ 0 \ \dots\}^T$$

$$[A] = [D + db^T + cd^T + \frac{1}{2}cb^T]$$

$$[C] = \begin{bmatrix} f & 1 & 0 & 0 & 0 & \cdots \\ -\frac{1}{2} & 0 & \frac{1}{2} & 0 & 0 & \cdots \\ 0 & -\frac{1}{2} & 0 & \frac{1}{2} & 0 & \cdots \\ 0 & 0 & -\frac{1}{2} & 0 & \frac{1}{2} & \ddots \\ 0 & 0 & 0 & -\frac{1}{2} & 0 & \ddots \\ \vdots & \vdots & \vdots & \ddots & \ddots & \ddots \end{bmatrix} \quad [D] = \begin{bmatrix} 0 & -\frac{1}{2} & 0 & 0 & \cdots & 0 \\ \frac{1}{4} & 0 & -\frac{1}{4} & 0 & \cdots & 0 \\ 0 & \frac{1}{6} & 0 & -\frac{1}{6} & \ddots & 0 \\ 0 & 0 & \frac{1}{8} & \ddots & \ddots & 0 \\ \vdots & \vdots & \ddots & \ddots & 0 & \ddots \\ 0 & 0 & 0 & 0 & \frac{1}{2N} & 0 \end{bmatrix}$$

$$[G] = \begin{bmatrix} 0 & \frac{1}{2} & 0 & 0 & 0 & \cdots \\ 0 & 0 & \frac{1}{4} & 0 & 0 & \cdots \\ 0 & -\frac{1}{4} & 0 & \frac{1}{4} & 0 & \ddots \\ 0 & 0 & -\frac{1}{4} & 0 & \frac{1}{4} & \ddots \\ 0 & 0 & 0 & -\frac{1}{4} & 0 & \ddots \\ \vdots & \vdots & \vdots & \ddots & \ddots & \ddots \end{bmatrix} \quad [H] = \begin{bmatrix} 0 & 0 & 0 & 0 & 0 & \cdots \\ 0 & 1/2 & 0 & 0 & 0 & \cdots \\ 0 & 0 & 2/2 & 0 & 0 & \cdots \\ 0 & 0 & 0 & 3/2 & 0 & \cdots \\ 0 & 0 & 0 & 0 & 4/2 & \cdots \\ \vdots & \vdots & \vdots & \vdots & \vdots & \ddots \end{bmatrix}$$

$$[K] = \begin{bmatrix} 0 & f & 2 & 3f & 4 & \cdots \\ 0 & -\frac{1}{2} & 0 & 0 & 0 & \cdots \\ 0 & 0 & -\frac{2}{2} & 0 & 0 & \cdots \\ 0 & 0 & 0 & -\frac{3}{2} & 0 & \ddots \\ 0 & 0 & 0 & 0 & \ddots & \ddots \\ \vdots & \vdots & \vdots & \vdots & \ddots & -\frac{M}{2} \end{bmatrix} \quad [K'] = \begin{bmatrix} f & \frac{1}{2} & 0 & 0 & 0 & \cdots \\ -\frac{1}{2} & 0 & \frac{1}{4} & 0 & 0 & \cdots \\ 0 & -\frac{1}{4} & 0 & \frac{1}{4} & 0 & \cdots \\ 0 & 0 & -\frac{1}{4} & 0 & \frac{1}{4} & \ddots \\ 0 & 0 & 0 & -\frac{1}{4} & 0 & \ddots \\ \vdots & \vdots & \vdots & \ddots & \ddots & \ddots \end{bmatrix}$$

$$[M] = \begin{bmatrix} \frac{1}{2} & 0 & -\frac{1}{4} & 0 & 0 & \cdots \\ 0 & \frac{1}{16} & 0 & -\frac{1}{16} & 0 & \cdots \\ -\frac{1}{4} & 0 & \frac{1}{6} & 0 & \ddots & \ddots \\ 0 & -\frac{1}{16} & 0 & \ddots & 0 & \ddots \\ 0 & 0 & \ddots & 0 & \ddots & \ddots \\ \vdots & \vdots & \ddots & -\frac{1}{8M} & \ddots & \frac{M}{4(M^2-1)} \end{bmatrix} \quad [S] = \begin{bmatrix} f & 0 & 0 & 0 & 0 & \cdots \\ 0 & 0 & 0 & 0 & 0 & \cdots \\ 0 & 0 & 0 & 0 & 0 & \cdots \\ 0 & 0 & 0 & 0 & 0 & \cdots \\ 0 & 0 & 0 & 0 & 0 & \cdots \\ \vdots & \vdots & \vdots & \vdots & \vdots & \ddots \end{bmatrix}$$

$$[T] = \begin{bmatrix} -ba & (b/\pi)[\sin \varphi_m - \varphi_m \cos \varphi_m] \\ b & (b/\pi)[\varphi_m - \sin \varphi_m \cos \varphi_m] \\ 0 & (b/\pi) \left[\frac{1}{n+1} \sin[(n+1)\varphi_m] + \frac{1}{n-1} \sin[(n-1)\varphi_m] - \frac{2}{n} \cos \varphi_m \sin(n\varphi_m) \right] \\ \vdots & \vdots \end{bmatrix}$$

Appendix B

Derivation of Spatial Gradient Components

NACA four-digit airfoils are given the designation NACA $\overline{m}\overline{p}xy$, with the following definitions:

- \overline{m} maximum ordinate of mean line, in percent chord
- \overline{p} chordwise position of maximum ordinate, in tenths of a chord
- xy maximum thickness of the airfoil, in percent chord

For simplicity, the following substitutions are made:

$$m = 0.01\overline{m}, \quad p = 0.1\overline{p}, \quad q = 2p - 1 \quad (\text{B.1})$$

The equation of the mean line is given in closed form [58]:

$$\frac{y_c}{c} = \begin{cases} (m/p^2) [2p\overline{x} - \overline{x}^2] & 0 \leq \overline{x} \leq p \\ [m/(1-p)^2] [(1-2p) + 2p\overline{x} - \overline{x}^2] & p < \overline{x} \leq 1 \end{cases} \quad (\text{B.2})$$

where $\overline{x} = (1 + x/b)/2$. As an example, the mean line for the NACA 2512 airfoil is shown in Fig.B.1.

In Eq. (B.2), the mean line is defined on the interval $\overline{x} = [0, 1]$, but for the thin airfoil theory, the mean line is defined on the interval $x = [-b, +b]$. The variables are transformed by Eq. (B.3).

$$x = b(2\overline{x} - 1), \quad b = c/2 \quad (\text{B.3})$$

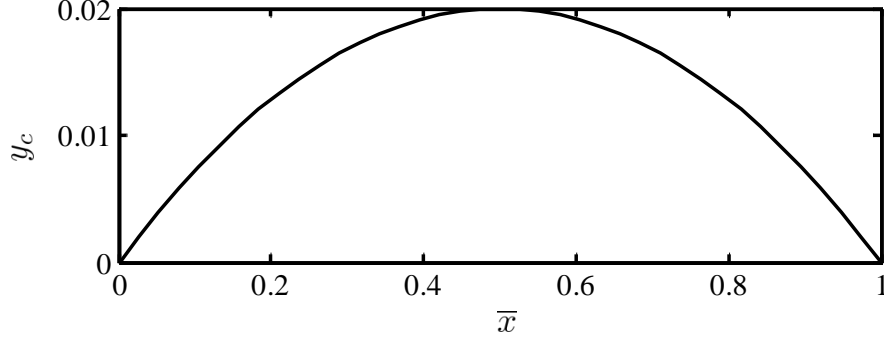


Figure B.1: Coordinates of NACA 2512 airfoil

The resulting equation of the mean line in the transformed coordinates becomes:

$$\frac{y_c}{b} = \begin{cases} \frac{2m}{b^2(1+q)^2} [b^2(1+2q) + 2bqx - x^2] & -b \leq x \leq qb \\ \frac{2m}{b^2(1-q)^2} [b^2(1-2q) + 2bqx - x^2] & qb < x \leq b \end{cases} \quad (\text{B.4})$$

Since $h \equiv -y_c$, the spatial gradient is calculated in closed form.

$$\frac{\partial h}{\partial x} = \begin{cases} \frac{4m(x-bq)}{b(1+q)^2} & -b \leq x \leq qb \\ \frac{4m(x-bq)}{b(1-q)^2} & qb < x \leq b \end{cases} \quad (\text{B.5})$$

With the Glauert change of variable, $x = b \cos \varphi$, the gradient becomes:

$$\frac{\partial h}{\partial x} = \begin{cases} \frac{4m(\cos \varphi - q)}{(1-q)^2} & 0 \leq \varphi \leq \varphi_q \\ \frac{4m(\cos \varphi - q)}{(1+q)^2} & \varphi_q < \varphi \leq \pi \end{cases} \quad (\text{B.6})$$

In Eq. (B.6) above, φ_q is the value of the Glauert variable evaluated at q . The gradient is now cast in a form that may be integrated to solve for the Glauert expansion coefficients. The solution of the first four terms is given below.

$$h'_0 = \frac{1}{\pi} \int_0^\pi \frac{\partial h}{\partial x} d\varphi$$

$$h'_0 = \frac{4mq}{(1-q^2)^2} \left[\frac{4}{\pi} \left(q \sin^{-1} q + \sqrt{1-q^2} \right) - (1+q^2) \right] \quad (\text{B.7})$$

$$h'_1 = \frac{2}{\pi} \int_0^\pi \frac{\partial h}{\partial x} \cos \varphi d\varphi$$

$$h'_1 = \frac{4m}{(1-q^2)^2} \left[(1+q^2) - \frac{4}{\pi} \left(q \sin^{-1} q + q^2 \sqrt{1-q^2} \right) \right] \quad (\text{B.8})$$

$$h'_2 = \frac{2}{\pi} \int_0^\pi \frac{\partial h}{\partial x} \cos 2\varphi \, d\varphi = \frac{32m}{3\pi} \frac{q}{\sqrt{1-q^2}} \quad (\text{B.9})$$

$$h'_3 = \frac{2}{\pi} \int_0^\pi \frac{\partial h}{\partial x} \cos 3\varphi \, d\varphi = \frac{32m}{3\pi} \frac{q^2}{\sqrt{1-q^2}} \quad (\text{B.10})$$

Useful approximations of the exact solutions can be made using Taylor series expansions in terms of q . Table B.1 summarizes the exact solutions, as well as first-order and third-order Taylor series expansions for the first four gradient coefficients. Note that similar results were given in Reference [59]. The linear approximations here agree with Ref. [59]; however a sign error in [59] causes the results here to be different from those shown in Ref. [59].

Table B.1: Spatial gradient components for NACA four-digit airfoils

$h'_0 = \frac{4qm}{(1-q^2)^2} \left[\frac{4}{\pi} (\sqrt{1-q^2} + q \sin^{-1} q) - (1+q^2) \right]$
$h'_0 \approx \frac{4m}{\pi} [(10 - 3\pi)q^3 + (4 - \pi)q] \approx \frac{4m}{\pi} (4 - \pi)q$
$h'_1 = \frac{4m}{(1-q^2)^2} \left[(1+q^2) - \frac{4}{\pi} \left(q \sin^{-1} q + q^2 \sqrt{1-q^2} \right) \right]$
$h'_1 \approx 4m(1 + \frac{3\pi-8}{\pi}q^2) \approx 4m$
$h'_2 = \frac{32m}{3\pi} \frac{q}{\sqrt{1-q^2}} \approx \frac{16m}{3\pi} (q^3 + 2q) \approx \frac{32m}{3\pi} q$
$h'_3 = \frac{32m}{3\pi} \frac{q^2}{\sqrt{1-q^2}} \approx \frac{32m}{3\pi} q^2 \approx 0$

Appendix C

Mean Line Expansion for LE and TE Droop

The purpose of this appendix is to derive a simple closed-form expression for a parabolic leading-edge or trailing-edge droop, similar to the geometry described in Ref. [50]. Jain, *et al.*, describe the NURBS control point methodology used to define the geometry of the drooped leading edge. However, since the exact geometry is not given, a simple approximation is employed to allow for analysis of the drooped leading-edge airfoil with thin airfoil theory. Only the meanline of the airfoil is needed for the airloads calculation. The procedure used to derive the simplified expression is detailed below.

First, the depiction of the airfoil from Fig. 1 of Ref. [50] is digitized, showing the geometry for a deflection of about 20° . Figure C.1 shows the digitized data plotted in the x - y coordinate system for leading-edge droop; and Figure C.2 is for trailing-edge droop. Second, a parabola is fit to each shape. Since the shapes are defined by the angles θ_{LE} and δ_{TE} (which are the droop angles measured from the leading edge or trailing edge to the initiation point of the droop), the deflections are easily written in terms of these points and these angles in the coordinate system of Fig. 2.1. For leading-edge droop,

$$y = -\frac{\theta_{LE}}{b} \frac{(x + eb)^2}{1 - e} \quad -b \leq x \leq -eb \quad (\text{C.1})$$

and for trailing-edge droop,

$$y = -\frac{\delta_{TE}}{b} \frac{(x - db)^2}{1 - d} \quad db \leq x \leq b \quad (\text{C.2})$$

where it has been assumed that $\tan \theta_{LE}$ and $\tan \delta_{TE}$ equals the angle in radians.

The slope of the mean line follows immediately for $0 \leq e \leq 1$, and $0 \leq d \leq 1$:

$$\frac{dy}{dx} = \begin{cases} [-2\theta_{LE}(x/b + e)] / (1 - e) & -b \leq x < -be \\ 0 & -be \leq x \leq bd \\ [-2\delta_{TE}(x/b - d)] / (1 - d) & bd < x \leq b \end{cases} \quad (\text{C.3})$$

With $x/b = \cos \varphi$, h_n and h'_n can be computed as follows.

$$h_0 = -\frac{1}{\pi} \int_0^\pi y(\varphi) d\varphi \quad (\text{C.4})$$

$$h_n = -\frac{2}{\pi} \int_0^\pi y(\varphi) \cos(n\varphi) d\varphi \quad n \geq 1$$

$$h'_0 = -\frac{1}{\pi} \int_0^\pi \frac{dy}{dx}(\varphi) d\varphi \quad (\text{C.5})$$

$$h'_n = -\frac{2}{\pi} \int_0^\pi \frac{dy}{dx}(\varphi) \cos(n\varphi) d\varphi \quad n \geq 1$$

The resultant integrals for the generalized deformations are:

$$\begin{aligned} h_0 &= \frac{b\delta_{TE}}{2\pi(1-d)} \left[(1 + 2d^2) \cos^{-1} d - 3d\sqrt{1-d^2} \right] \\ &\quad + \frac{b\theta_{LE}}{2\pi(1-e)} \left[(1 + 2e^2) \cos^{-1} e - 3e\sqrt{1-e^2} \right] \\ h_1 &= \frac{2b\delta_{TE}}{3\pi(1-d)} \left[-3d \cos^{-1} d + (2 + d^2)\sqrt{1-d^2} \right] \\ &\quad + \frac{2b\theta_{LE}}{3\pi(1-e)} \left[3e \cos^{-1} e - (2 + e^2)\sqrt{1-e^2} \right] \end{aligned}$$

$$\begin{aligned}
h_2 &= \frac{b\delta_{TE}}{6\pi(1-d)} \left[3 \cos^{-1} d - (5 - 2d^2)d\sqrt{1-d^2} \right] \\
&\quad + \frac{b\theta_{TE}}{6\pi(1-e)} \left[3 \cos^{-1} e - (5 - 2e^2)e\sqrt{1-e^2} \right] \\
h_n &= Q_1 \left\{ [1 - n^2 + d^2(2 + n^2)] \sin(n \cos^{-1} d) 3d\sqrt{1-d^2} n \cos(n \cos^{-1} d) \right\} \\
&\quad + Q_2 \left\{ [1 - n^2 + e^2(2 + n^2)] \sin(n \cos^{-1} e) - 3e\sqrt{1-e^2} n \cos(n \cos^{-1} e) \right\}
\end{aligned} \tag{C.6}$$

for $n \geq 3$, where Q_1 and Q_2 are given by

$$\begin{aligned}
Q_1 &= \frac{4b\delta_{TE}}{n\pi(1-d)(n^2-4)(n^2-1)} \\
Q_2 &= \frac{4b\theta_{LE}(-1)^n}{n\pi(1-d)(n^2-4)(n^2-1)}
\end{aligned}$$

The generalized mean-line gradients are given by

$$\begin{aligned}
h'_0 &= \frac{2\delta_{TE}}{\pi(1-d)} \left(-d \cos^{-1} d + \sqrt{1-d^2} \right) + \frac{2\theta_{LE}}{\pi(1-e)} \left(e \cos^{-1} e - \sqrt{1-e^2} \right) \\
h'_1 &= \frac{2\delta_{TE}}{\pi(1-d)} \left(\cos^{-1} d - d\sqrt{1-d^2} \right) + \frac{2\theta_{LE}}{\pi(1-e)} \left(\cos^{-1} e - e\sqrt{1-e^2} \right) \\
h'_n &= \frac{4\delta_{TE}}{n\pi(1-d)(n^2-1)} \left[d \sin(n \cos^{-1} d) - n\sqrt{1-d^2} \cos(n \cos^{-1} d) \right] \\
&\quad + \frac{4\theta_{LE}}{n\pi(1-e)(n^2-1)} \left[e \sin(n \cos^{-1} e) + (-1)^n n\sqrt{1-e^2} \cos(n \cos^{-1} e) \right] \quad n \geq 2
\end{aligned} \tag{C.7}$$

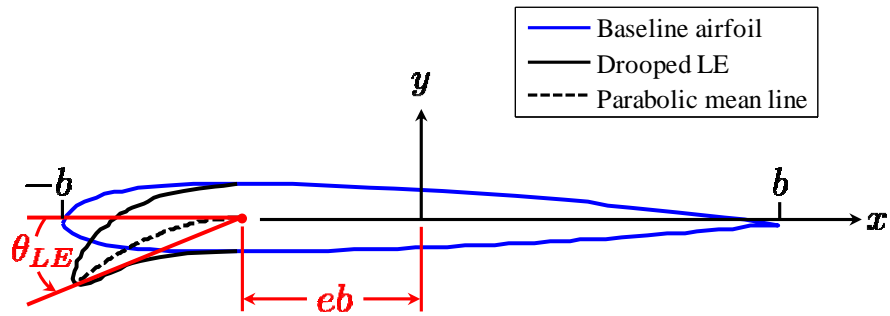


Figure C.1: Geometry of drooped leading-edge airfoil

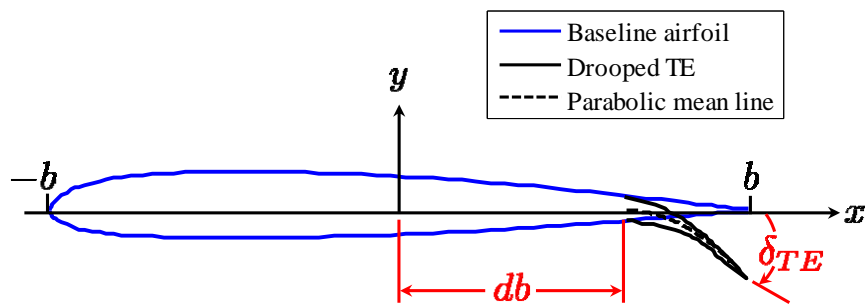


Figure C.2: Geometry of drooped trailing-edge airfoil

Appendix D

Chain Rule Application to Stall Residual Derivatives

The purpose of this appendix is to illustrate the method for computing the total derivative of the stall residuals when applying the dynamic stall model. The stall model is given by Eq. (2.41), reprinted here for clarity.

$$\frac{b^2}{u_T^2} \ddot{\Gamma}_n + \eta \frac{b}{u_T} \dot{\Gamma}_n + \omega^2 \Gamma_n = -b u_T \omega^2 \left[\Delta C_n + e \frac{d\Delta C_n}{dt} \frac{b}{u_T} \right] \quad (\text{D.1})$$

The derivative in the last term of Eq. (D.1), $d(\Delta C_n)/dt$, deserves special consideration. It is the total time derivative of the generalized stall residual ΔC_n . In Chapter 3, we show that ΔC_n is a function of α , α_{0L} , and α_{shift} (or alternatively α and z). In turn, α_{0L} , α_{shift} , and z are functions of the generalized spatial gradients h'_n . Thus, it is a non-trivial exercise to apply the chain rule correctly to determine $d(\Delta C_n)/dt$.

If ΔC_n is known in terms of z , we conclude the following:

$$\begin{aligned} \frac{d(\Delta C_n)}{dt} &= \frac{\partial(\Delta C_n)}{\partial z} \frac{dz}{dt} \\ &= \frac{\partial(\Delta C_n)}{\partial z} \left[\frac{\partial z}{\partial \alpha} \frac{d\alpha}{dt} + \frac{\partial z}{\partial h'_0} \frac{dh'_0}{dt} + \frac{\partial z}{\partial h'_1} \frac{dh'_1}{dt} + \dots \right] \end{aligned} \quad (\text{D.2})$$

This procedure is best illustrated by an example. From Eq. (3.20) for the NACA 0012 airfoil, the variable z is given by:

$$z = \alpha - \alpha_{ss} = \alpha - 0.293 + 0.870h'_0 + 0.099h'_1 - 0.490h'_2 \quad (\text{D.3})$$

The total derivative of z is given by

$$\frac{dz}{dt} = \frac{d\alpha}{dt} + 0.870\frac{dh'_0}{dt} + 0.099\frac{dh'_1}{dt} - 0.490\frac{dh'_2}{dt} \quad (\text{D.4})$$

Furthermore, from a fit of the average shifted ΔC_L curves for the eighteen NACA airfoils discussed in Section 3.2, an approximate expression for ΔC_L in terms of z is given by Eq. (3.22), repeated below.

$$\Delta C_L \approx 0.2689 \tan^{-1}(54.54z) + 15.89(z + 0.3192)^4 + 0.4070 \quad (\text{D.5})$$

Eq. (D.5) is only valid for $z \geq -0.3192$. It follows that the partial derivative $\partial(\Delta C_L)/\partial z$ is given by

$$\frac{\partial(\Delta C_L)}{\partial z} = \frac{14.67}{1 + 2975z^2} + 63.56(z + 0.3192)^3 \quad (\text{D.6})$$

The total derivative is given from Eqs. (D.2), (D.4), and (D.6):

$$\begin{aligned} \frac{d(\Delta C_L)}{dt} = & \left[\frac{14.67}{1 + 2975z^2} + 63.56(z + 0.3192)^3 \right] \\ & \left(\frac{d\alpha}{dt} + 0.870\frac{dh'_0}{dt} + 0.099\frac{dh'_1}{dt} - 0.490\frac{dh'_2}{dt} \right) \end{aligned} \quad (\text{D.7})$$

Eq. (D.7) can be written alternately in terms of a morphing variable, such as the flap deflection β .

$$\begin{aligned} \frac{d(\Delta C_L)}{dt} = & \left[\frac{14.67}{1 + 2975z^2} + 63.56(z + 0.3192)^3 \right] \\ & \left[\frac{d\alpha}{dt} + \left(0.870\frac{\partial h'_0}{\partial \beta} + 0.099\frac{\partial h'_1}{\partial \beta} - 0.490\frac{\partial h'_2}{\partial \beta} \right) \frac{d\beta}{dt} \right] \end{aligned} \quad (\text{D.8})$$

The partial derivatives $\partial h'_n/\partial\beta$ are found from the transformation matrix used to compute h'_n . For an airfoil with a trailing-edge flap, the first three terms are:

$$\begin{aligned}\frac{\partial h'_0}{\partial\beta} &= \frac{1}{\pi} \cos^{-1} d \\ \frac{\partial h'_1}{\partial\beta} &= \frac{2}{\pi} \sqrt{1-d^2} \\ \frac{\partial h'_2}{\partial\beta} &= \frac{2}{\pi} d\sqrt{1-d^2}\end{aligned}\tag{D.9}$$

where db is the location of the flap hinge aft of the mid-chord. For any of the equations above, finite-difference approximations of the derivatives can be used in place of the analytical expressions.

References

- [1] D. Petot. Progress in the semi-empirical prediction of the aerodynamic forces due to large amplitude oscillations of an airfoil in attached or separated flow. In *Proceedings of the Ninth European Rotorcraft Forum*, September 1983.
- [2] D. Petot. Differential equation modeling of dynamic stall. *Rech. Aerosp.*, 5, 1989.
- [3] Daniel J. Rudy. Three interpretations of the ONERA dynamic-stall model with applications to rotor blade flapping response. Master of Science thesis, Washington University, St. Louis, Missouri, 1983.
- [4] D. A. Peters and M. Johnson. Finite-state airloads for deformable airfoils on fixed and rotating wings. *Symposium on Aeroelasticity and Fluid/Structure Interaction, American Society of Mechanical Engineers Winter Annual Meeting*, November 1994.
- [5] D. A. Peters, S. Karunamoorthy, and W. Cao. Finite state induced flow models part I: Two-dimensional thin airfoil. *Journal of Aircraft*, 32(2):313–322, March–April 1995.
- [6] M. Munk. General theory of thin wing sections. *NACA Report 142*, 1923.
- [7] T. Theodorsen and I. E. Garrick. General potential theory of arbitrary wing sections. *NACA Rept. 452*, 1934.
- [8] I. E. Garrick. On some reciprocal relations in the theory of nonstationary flows. *NACA Report 629*, 1939.
- [9] T. Theodorsen. General theory of aerodynamic instability and the mechanism of flutter. *NACA Rept. 496*, May 1934.
- [10] T. von Kármán and J. M. Burgers. *General Aerodynamic Theory - Perfect Fluids*, volume II. Julius Springer, Berlin, 1935.
- [11] I. E. Garrick. Propulsion of flapping and oscillating airfoil. *NACA TR 567*, May 1936.
- [12] R. Issacs. Airfoil theory for flows of variable velocity. *Journal of the Aeronautical Sciences*, 12(1):113–117, 1945.

- [13] R. Issacs. Airfoil theory for rotary wing aircraft. *Journal of the Aeronautical Sciences*, 13(4):218–220, 1946.
- [14] J. M. Greenberg. Airfoil in sinusoidal motion in a pulsating stream. *NACA TN No. 1326*, June 1947.
- [15] D. A. Peters, M. Hsieh, and A. Torrero. A state-space airloads theory for flexible airfoils. In *Proceedings of the American Helicopter Society 62nd Annual Forum*, May 2006.
- [16] R. G. Loewy. A two-dimensional approximation to unsteady aerodynamics in rotary wings. *Journal of the Aeronautical Sciences*, 24(2):81–92, 1957.
- [17] H. Wagner. Über die entstehung des dynamischen auftriebs von tragflugeln. *ZAMM, Bd. 5, Heft 1*, pages 17–35, 1925.
- [18] W. P. Jones. Aerodynamic forces on wings in non-uniform motion. *British Aeronautical Research Council, R & M 2117*, August 1945.
- [19] R. T. Jones. Operational treatment of the nonuniform lift theory to airplane dynamics. *NACA TN 667*, pages 347–350, March 1938.
- [20] R. T. Jones. The unsteady lift of a wing of finite aspect ratio. *NACA Report 681*, pages 31–38, June 1939.
- [21] J. W. Edwards, J. V. Breakwell, and A. E. Bryson. Active flutter control using generalized unsteady aerodynamic theory. *Journal of Guidance and Control*, 1:32–40, January-February 1978.
- [22] J. W. Edwards, H. Ashley, and J. V. Breakwell. Unsteady aerodynamic modeling for arbitrary motions. *AIAA Journal*, 17(4):365–374, April 1979.
- [23] R. Vepa. On the use of Padé approximants to represent unsteady aerodynamic loads for arbitrarily small motions of wings. In *Proceedings of AIAA 14th Aerospace Sciences Meeting*, 1976.
- [24] E. H. Dowell. A simple method for converting frequency domain aerodynamics to the time domain. *NASA TM-81844*, October 1980.
- [25] E. H. Dowell. Eigenmode analysis in unsteady aerodynamics: Reduced-order models. *AIAA Journal*, 34(8):1548–1583, August 1996.
- [26] M. A. H. Dinyavari and P. P. Friedmann. Application of time-domain unsteady aerodynamics to rotary-wing aeroelasticity. *AIAA Journal*, 24(9):1424–1432, 1986.

- [27] P. P. Friedmann and C. Venkatesan. Finite state modelling of unsteady aerodynamics and its application to a rotor dynamic problem. In *Proceedings of the Eleventh European Rotorcraft Forum*, September 1985.
- [28] B. Glaz, L. Liu, and P. Friedmann. Reduced order nonlinear unsteady aerodynamic modeling using a surrogate based approach. In *AHS Specialist's Conference on Aeromechanics*, pages 613–634, San Francisco, CA, January 2010.
- [29] D. A. Peters, D. Barwey, and M. Johnson. Finite-state airloads modeling with compressibility and unsteady free-stream. In *Proceedings of the Sixth International Workshop on Dynamics and Aeroelastic Stability Modeling of Rotorcraft Systems*, November 1995.
- [30] W. J. McCroskey. The phenomenon of dynamic stall. *NASA TM 81264*, March 1981.
- [31] K. McAlister, O. Lambert, and D. Petot. Application of the ONERA model of dynamic stall. *NASA Technical Paper 2399*, 1984.
- [32] M. S. Chandrasekhara, P. B. Martin, and C. Tung. Compressible dynamic stall control using a variable droop leading edge airfoil. *Journal of Aircraft*, 41(4):862–869, July-August 2004.
- [33] P. B. Martin, K. W. McAlister, M. S. Chandrasekhara, and W. Geissler. Dynamic stall measurements and computations for a VR-12 airfoil with a variable droop leading edge. In *Proceedings of the American Helicopter Society 59th Annual Forum*, May 2003.
- [34] G. Depailler and P. Friedmann. Alleviation of dynamic stall induced vibrations using actively controlled flaps. In *Proceedings of the American Helicopter Society 58th Annual Forum*, pages 19–22, June 2002.
- [35] Hyeonsoo Yeo. Assessment of active controls for rotor performance enhancement. *Journal of the American Helicopter Society*, 53(2):152–163, April 2008.
- [36] N. Hariharan and J. G. Leishman. Unsteady aerodynamics of a flapped airfoil in subsonic flow by indicial concepts. In *AIAA/ASME/ACE/AHS/ASC Structures, Structural Dynamics, and Materials Conference*, pages 613–634, April 1995.
- [37] A. Wickenheiser and E. Garcia. Aerodynamic modeling of morphing wings using an extended lifting-line analysis. *Journal of Aircraft*, pages 10–16, January-February 2007.
- [38] T. H. Pulliam, M. Nemeč, T. Holst, and D. W. Zingg. Comparison of evolutionary (genetic) algorithm and adjoint methods for multi-objective viscous airfoil optimizations. In *Proceedings of the 41st AIAA Aerospace Sciences Meeting*, January 2003.

- [39] Bandu N. Pamadi, Patrick C. Murphy, Vladislav Klein, and Jay M. Brandon. Prediction of unsteady aerodynamic coefficients at high angles of attack. In *Proceedings of the AIAA Atmospheric Flight Mechanics Conference*, August 2001.
- [40] D. A. Peters and C. J. He. Finite state induced flow models part ii: Three-dimensional rotor disk. *Journal of Aircraft*, 32(2):323–333, 1995.
- [41] D. A. Peters and C. J. He. Correlation of measured induced velocities with a finite-state wake model. *Journal of the American Helicopter Society*, 36(3):60–70, July 1991.
- [42] T. S. Beddoes. A synthesis of unsteady aerodynamic effects including stall hysteresis. In *Proceedings of the 1st European Rotorcraft Forum*, September 1975.
- [43] J. G. Leishman and T. S. Beddoes. A semi-empirical model for dynamic stall. *Journal of the American Helicopter Society*, 34(3):3–17, July 1989.
- [44] David A. Peters. Toward a unified lift model for use in rotor blade stability analyses. *Journal of the American Helicopter Society*, July 1985.
- [45] W. J. McCroskey. Unsteady airfoils. *Annual Review of Fluid Mechanics*, 14:285–311, 1982.
- [46] S. Thepvongs, C. E. S. Cesnik, R. Palacios, and D. A. Peters. Finite-state aeroelastic modeling of rotating wings with deformable airfoils. In *Proceedings of the American Helicopter Society 64th Annual Forum*, May 2008.
- [47] Mark James Johnson. Finite-state airloads for deformable airfoils on fixed and rotating wings. Master of Science thesis, Washington University, St. Louis, Missouri, 1995.
- [48] P. Plantin De Hughes, K. W. McAlister, and C. Tung. Effect of an extendable slat on the stall behavior of a VR-12 airfoil. *NASA Technical Paper 3407*, September 1993.
- [49] E. Jacobs, K. Ward, and R. Pinkerton. The characteristics of 78 related airfoil sections from tests in the variable-density wind tunnel. *NACA Report No. 460*, 1933.
- [50] R. Jain, K. Szema, R. Munipalli, H. Yeo, and I. Chopra. CFD-CSD analysis of active control of helicopter rotor for performance improvement. In *Proceedings of the American Helicopter Society 65th Annual Forum*, May 2009.
- [51] L. Ahaus, D. Peters, and A. Kahler. Simplified analysis of sectional airloads on morphing airfoils. In *Proceedings of the AHS 66th Annual Forum & Technology Display*, May 2010.

- [52] W. J. McCroskey. A critical assessment of wind tunnel results for the NACA 0012 airfoil. *NASA Technical Memorandum 100019*, October 1987.
- [53] A. Krzysiak and J. Narkiewicz. Aerodynamic loads on airfoil with trailing-edge flap pitching with different frequencies. *Journal of Aircraft*, 43(2):407–418, March-April 2006.
- [54] K. W. McAlister, S. L. Pucci, W. J. McCroskey, and L. W. Carr. An experimental study of dynamic stall on advanced airfoil sections volume 2. pressure and force data. *NASA TM 84245*, Sep 1982.
- [55] L. Ahaus and D. Peters. Unified airloads model for morphing airfoils in dynamic stall. In *Proceedings of the American Helicopter Society Specialist’s Conference on Aeromechanics*, San Francisco, CA, January 2010.
- [56] J. Bain, L. Sankar, JVN Prasad, O. Bauchau, D. A. Peters, and C. He. Computational modeling of variable droop leading edge in forward flight. In *Proceedings of the AIAA Fourth Flow Control Conference*, June 2008.
- [57] L. Ahaus, N. Liggett, D. Peters, and M. Smith. Unsteady aerodynamics of single and multi-element airfoils. In *Proceedings of the 36th European Rotorcraft Forum*, Paris, France, September 2010.
- [58] I. H. Abbott and A. E. von Doenhoff. *Theory of Wing Sections*. Dover, New York, 1959.
- [59] D. A. Peters, D. Barwey, and A. Su. An integrated airloads-inflow model for use in rotor aeroelasticity and control analysis. *Mathematical and Computer Modelling*, 19(3/4):109–123, 1994.

Vita

Loren A. Ahaus

- Date of Birth** August 14, 1974
- Place of Birth** Oklahoma City, Oklahoma
- Degrees** B.S. Mechanical Engineering, May 1997
M.S. Mechanical Engineering, May 2009
Ph.D. Mechanical Engineering, May 2010
- Professional Societies** American Helicopter Society
American Institute of Aeronautics and Astronautics
- Honors** Vertical Flight Foundation Scholarship for Educational Excellence, awarded April 30, 2008.
- Publications** Ahaus, L., Peters, D., and Kahler, A. Simplified Analysis of Sectional Airloads on Morphing Airfoils, *Proceedings of the 66th Annual Forum of the American Helicopter Society*, May 11-13, 2010, Phoenix, AZ.
- Ahaus, L. and Peters, D. Unified Airloads Model for Morphing Airfoils in Dynamic Stall, *Proceedings of the American Helicopter Society Specialist's Conference on Aeromechanics*: January 20-22, 2010, San Francisco, CA.
- Ahaus, L. and Peters, D. Comparison of Finite-State Dynamic Stall Theory with Unsteady Data, *Proceedings of the 34th Annual European Rotorcraft Forum*: September 16-19, 2008, Liverpool, U.K.
- Peters, D. and Ahaus, L. Correlation of Unsteady State-Space Airloads Theory to Oscillating Airfoil Windtunnel Data, *Proceedings of the Tenth Pan American Congress of Applied Mechanics*: January 7-11, 2008, Cancun, Mexico.

Ahaus, L. State-Space Airloads Theory for Morphing Airfoils with Dynamic Stall, student poster session, National Science Foundation CMMI Conference: January 7-10, 2008, Knoxville, TN.

May 2010

Short Title: Stalled Morphing Airfoil Loads

Ahaus, Ph.D. 2010